KU LEUVEN

FACULTY OF SCIENCE

A comprehensive analysis of a rare Wolf-Rayet multiple system in the Large Magellanic Cloud

Soetkin JANSSENS

Supervisor: Dr. T. Shenar
Instituur voor Sterrenkunde,
Department of Physics & Astronomy,
KU Leuven

Co-supervisor: Dr. L. Mahy
Instituur voor Sterrenkunde,
Department of Physics & Astronomy,
KU Leuven

Thesis presented in
fulfillment of the requirements
for the degree of Master of Science
in Astronomy & Astrophysics

Academic year 2019-2020

A long time ago in a galaxy far, far away ...[1]

Episode 0

THE PREFACE

It is a period of multi-messenger astronomy. Many methods are available in observing distant stars and galaxies and astronomers are trying to reveal the secrets of the Universe.

Some are researching the bigger structures, galaxies, and others analyse their individual building blocks, stars. The most massive of these stars end their lives as black holes. The process towards these dead stars is accompanied by a supernova explosion with enough power to destroy an entire planet (and even entire stellar systems).

One of the questions in massive star research is: "How do most massive stars evolve and how do they impact the chemical evolution of the Universe?" Astronomers do not only observe stars in the Milky Way, but also analyse systems of (massive) stars in other galaxies, in order to understand the impact of other environments on their evolution.

Soetkin Janssens, a young astronomer, analysed a rare multiple system of massive stars in the Large Magellanic Cloud, called BAT99 126. It was a complex analysis, but she had a lot of people who helped and supported her...

[1]The small introductory part of the preface of this thesis is written as a variation of the opening crawl from the famous Star Wars movies, in particular with elements of Episode IV, the original first movie, as I hope this will be the first of many research achievements I will complete. An animated version can be reached at `https://starwarsintrocreator.kassellabs.io/#!/CM9TwTGrJpksfJ3rI4Eg`

The inspiration behind the topic of research, a rare multiple system, is hidden deeper in the details of the system. One of the stars in the system is a Wolf-Rayet star. This is an evolved phase of the most massive stars and as will become clear throughout the thesis these stars are very rare (and important), hence the origin of the term 'rare' in the declaration of the system. Around the time when choosing a bachelor thesis project, my interest in these stars was sparked by an article which explained that the Solar system might have formed thanks to such a Wolf-Rayet star[2]. At that time, I was participating in the group meetings of Prof. Hans van Winckel, for which I am still very thankful he gave me that opportunity.

Dr. Ana Escorza Santos, at the time a PhD student in the group of Hans, asked me if there was any project I wanted to do my bachelor thesis on. She is the reason why I was able to already perform research on these Wolf-Rayet stars. Just as C-3PO was the one who led Luke Skywalker to Obi-Wan Kenobi, it was Ana who led me to one of my supervisors. If it would not have been for her, Dr. Laurent Mahy might not have proposed the project I did back then and I would not have contacted him again for a master thesis subject.

Just as Luke Skywalker had Yoda and Obi-Wan Kenobi to teach him the art of the Jedi, I had Dr. Tomer Shenar and Dr. Laurent Mahy, my supervisor and co-supervisor, to teach me many new analysis techniques. Upon my request, they proposed this extremely interesting thesis topic of analysing a rare Wolf-Rayet multiple system. They gave me the opportunity to perform complex analysis, shared their expertise with me and also guided me through the process of writing this thesis. From very early on, the system appeared to be more complex than originally thought and they provided me with the mental support to keep on progressing. They have always been ready to answer my questions, no matter their numbers. Tomer introduced me to the technique of cross-correlation, an important tool in the performed analysis, and Laurent has helped a lot with the usage of PHOEBE. Moreover, they gave me the chance to write a proposal to apply for new data, an amazing opportunity to expand my research skills. For all of this and much more, I am indefinitely grateful!

I also want to thank everybody in the group of Prof. Hugues Sana for their help and insights. In particular, I want to thank Julia Bodensteiner for all the help she has offered while writing the proposal, for sharing the expertise she has with MUSE (a unit mounted on the Very Large Telescope in Chile) and for giving me advice on the plotting style of certain graphs and figures. I also want to thank Hugues and Dr. Pablo Marchant for helping me with the proposal and for joining the discussions on the evolution of the system. For this, an extra big thank you to Pablo, as he has helped

[2]https://astronomy.com/news/2018/01/did-the-solar-system-form-in-a-bubble

me enormously with studying the evolutionary part of the system and performing the simulations with MESA. He was always ready to answer my questions regarding the evolution/simulations, even when it turned out the simulations needed to be redone.

I would like to thank my office roommates, Frederik De Ceuster, Jordan Van Beeck, Dr. Miguel Montarges and Dr. Taissa Danilovich. They have immediately accepted me as one of their own. They helped me out with Python related issues, Redhat questions (thank you for repeating some stuff multiple times) and occasionally the necessary feedback. Many interesting conversation were held, both related and a little less related to the topic of (this) work. It was an amazing experience working in the same office with all these people. I also want to thank Dr. Marie Van de Sande for always taking me up in conversations when walking into the office, but also for making me one of those cute little puppets, with your characteristic moving eyes glued on them, when you made them for the rest of the office. It was really nice feeling so accepted and 'part of the team'.

Although I did not end up using the data, I thank Dr. Timothy Van Reeth for subtracting TESS[3] light curve data of BAT99 126, in order to see whether it would give any added value to the analysis. I also thank Dr. Dominic Bowman, a specialist in the field of stellar pulsations, for looking at the light curve to see if any periodic variations besides the 1.55-day signal could be detected.

I would like to say thank you to my fellow students and friends. They have supported me throughout all of the academic years. There are many names I could mention here, but in particular I will say thank you to Tim De Ryck for being my partner for the bachelor thesis, which was a tip-toe in the ocean of astronomical research. I also want to thank Wouter Peere. He listened to all my problems and was always able to make me laugh, even in very stressful times. To all my friends: You made all my academic years an extremely wonderful time, for which I could not be more grateful!

Last but not least I want to thank my family for their support, especially my parents, for always being there for me and for providing me with everything I needed to become a scientist. You have made me to who I am today and without you I would have never been able to do everything I did. Even though we sometimes did not agree or even when I was so stressed I became a less enjoyable person, you were there for me and always tried to cheer me up. I can not express my gratitude enough.

Grateful, I am.

Yoda

[3]Transiting Exoplanet Survey Satellite

Summary

Stars born with masses larger than eight times the mass of the Sun ($M_{\rm initial} > 8M_{\odot}$) are driving the evolution of the Universe, yet they are rare. These massive stars, which are OB-type stars, emit powerful radiation, ionising the material that surrounds them, and they impact star formation rates in their surroundings. Massive stars end their lives with a supernova explosion, leaving behind a compact object - a neutron star or a black hole. If we want to understand the chemical evolution of the Universe and the nature of some of the most energetic sources in the Universe, the evolution of massive stars needs to be understood.

Almost all massive stars are found in a binary or multiple system. Although it is predicted that most massive stars will interact with a companion during their evolution, binary-interaction physics is not well established. Close-binary physics remains an important field of study in the evolution of massive stars, as astronomers try to answer how most massive stars evolve.

In this thesis, a rare multiple system of massive stars is analysed: BAT99 126, located in the Large Magellanic Cloud at 50 kpc from Earth. It is thought to host both a *Wolf-Rayet* (WR) star and a close binary. A WR star is an evolved massive star, but only the most massive stars will reach this stage. It is an important stage as a WR star represents one of the final stages in massive star evolution. WR stars are not well understood, in particular the influence of binary interactions on their formation remains uncertain.

With spectroscopic and photometric data, the parameters of the system are determined: the multiplicity, radial velocities, luminosities, effective temperatures and masses. After the determination of these parameters, tailored modelling is performed.

In this thesis, I show that BAT99 126 comprises four components: two O-type stars, a WR star and a B-type star. The spectral types are O4 V and O6 V for the two O-type stars respectively, WN2.5-3 for the WR star and B1 V for the B-type star. Radial velocity measurements exclude the previously derived orbit of 25.5 days for the WR star (Foellmi et al., 2003b). The data remain inconclusive on the orbital configuration of the WR and B-type star. However, they do display motion for the B-type star. Orbital analysis shows that the two O-type stars are the components which produce the 1.55-day signal, with masses of $34 \pm 4M_{\odot}$ and $15 \pm 2M_{\odot}$ for the O4 V and O6 V star respectively.

The luminosity of the WR star suggests an age around 4 Myr. Combining this with the obtained parameters suggests that the close O+O binary is an Algol system, that is, a system that has gone through a previous phase of mass transfer. However, simulations performed in this work using standard mass transfer physics do not seem to be able to reproduce the

system. Because of the complexity of the system, there is an uncertainty on some stellar parameters, which could be the reason why we are not able to reproduce the system from theoretical simulations. In order to obtain more certainty on the configuration of the WR star and the B-type star, we have applied for more data. Future research will also perform spectral disentangling of the system. This should enable us to gain further insights on the configuration of this complex system. It will give more precise measurements on the stellar parameters such that close binary physics can be constrained better.

Vulgarizing summary

In order to understand the chemical evolution of the Universe, scientists study heavy (massive) stars as they are extremely important: these stars are the reason we have so many different elements in the Universe. Moreover, they are responsible for powerful supernova explosions, resulting in exotic objects like black holes and neutron stars. If astronomers can understand how such stars live and die, they can obtain possible keys to unlock the hidden secrets of some of the most powerful radiation sources in the Universe. However, these massive stars are extremely rare.

Almost all massive stars are found in a binary or multiple system. Although it is predicted that most massive stars will interact with a companion during their evolution, binary-interaction physics is not well understood. Close-binary physics remains an important field of study in the evolution of massive stars, as astronomers try to answer how most massive stars evolve.

In this thesis, one rare multiple system of massive stars is analyzed: BAT99 126, located in the Large Magellanic Cloud at 150 000 light years from Earth. As multiple stars are present, it is an interesting system to study, because different stellar parameters can be obtained accurately. These can then be used to verify, test and refine existing theoretical models, in particular models on binary evolution. Two types of data are used for the determination of all the different parameters: spectroscopic and photometric. The spectroscopic data can tell us something about the number of components of the system, the type of stars, and the shape of their orbit. The photometric data gives information about the luminosity and the size of the components, and can help determine the different masses.

In this thesis, I show that the system has 4 components: one rare *Wolf-Rayet* (WR) star, one B-type star and a close binary system of two O-type stars. O- and B-type stars are by definition massive stars. A WR star is an evolved massive star, but since only the most massive stars will become WR stars, they are even rarer than 'normal' massive stars. On top of that the WR phase is very short-lived.

The data exclude a previously derived period of 25.5 days for the WR star. A clear motion of the B-type star is detected, however it remains inconclusive whether it is bound to the WR star or not. The two O-type stars are in a very close orbit with a period of 1.55 days and masses of 36 and 15 times the mass of the Sun.

Based on the data obtained for the WR star, the system is calculated to be around 4 million years old. As the age of the system is known, the evolution of the binary components can be studied and its evolution simulated. It follows that the two O-type stars did not evolve like single stars, but that during their lifetime, there was a mass exchange between the two

components. It was however not possible to reproduce the system using standard mass transfer physics. A possibility is that the stellar parameters contain some uncertainty which can lead to errors in the simulation.

The complexity of the system could be a cause of the increased uncertainty on some stellar parameters. Even small differences can alter the results of the simulations of a complex system like this one. More observational data is applied for, to obtain certainty on the configuration of the WR star and the B-type star. It will give more precise measurements on the stellar parameters such that close binary physics can be constrained better.

Contents

List of Figures

List of Tables

Acronyms

BAT99 126 The system of study. x, xiii–xv, 3, 4, 6, 63, 65, 70, 72, 73, 75, 102, 106, 118, 122, 123, 130–132, 151, 152

BH Black-hole. xii, 20, 60–62, 131

BONNSAI BONN Stellar Astrophysics Interface. 120, 121

CAK Castor-Abbott-Klein stellar wind theory. xii, xvi, 29, 30

CCF Cross-correlation function. xiii, xiv, 85–87, 90, 93, 95, 153–155, 157

CNO carbon-oxygen-nitrogen cycle. 11, 21

FD Finite disk correction theory to the CAK model. xii, 30

HJD Heliocentric Julian Date. 44, 66, 67

HRD Hertzsprung-Russell diagram. xii, 8, 9, 11, 13, 15, 18, 19, 24, 25, 59, 120, 125

LBV Luminous blue variable. 18, 19, 29, 30

LC Light curve. 70, 105–109

LMC Large Magellanic Cloud. xiv, xv, 3, 19, 63, 70, 75, 81, 83, 95–97, 99–101, 114, 120, 122–125, 148

LTE Local thermodynamic equilibrium. 35

MESA Modules for Experiments in Stellar Astrophysics, stellar evolution code. 122, 123

MJD Modified Julian Date. xiii, 66, 67, 93, 95–97, 154

non-LTE No local thermodynamic equilibrium. xvii, 36

NS Neutron star. 16, 18

OGLE Optical Gravitational Lensing Experiment. xiii, 63, 70, 73

PHOEBE PHysics Of Eclipsing BinariEs, orbital analysis software. xv, 48, 106–109, 111

PoWR Potsdam Wolf-Rayet non-LTE stellar atmosphere code. 36, 69, 89, 114

pp Proton-proton chain. 11

RLOF Roche-lobe overflow. 51, 57

RV Radial velocity. xiii–xv, 85, 87–93, 95–99, 102, 104, 106–109, 132, 153–157

S/N Signal-to-noise ratio. 67, 70, 87

SED Spectral energy distribution. xi, xiv, xv, 31, 69, 113–118

TLUSTY TLUSTY non-LTE stellar atmosphere code. xiii, 36, 80, 81, 83, 95, 102, 114, 115

ULX Ultra-luminous X-ray source. xii, 61, 62, 118, 131

UVES Ultraviolet and Visual Echelle Spectrograph. xv, 66, 67, 69, 132

WC Wolf-Rayet star of the carbon sequence. 21

WN Wolf-Rayet star of the nitrogen sequence. 21, 63, 80

WO Wolf-Rayet star of the oxygen sequence. 21

WR Wolf-Rayet. v–viii, x, xiii–xv, 3, 19, 21–23, 29, 30, 36, 39, 40, 63, 69, 72, 74–77, 79–81, 83, 88–93, 96, 98–100, 102–105, 113–115, 117–119, 129–132, 153–156

Units & Constants

	Symbol	value	Unit
Solar mass	$M_\odot$	1.9891×10^{30}	kg
Solar radius	$R_\odot$	696 340 000	m
Solar luminosity	$L_\odot$	3.828×10^{26}	W
parsec	pc	$3.08567758 \times 10^{16}$	m
year	yr		
Gravitational constant	G	6.67408×10^{-11}	$m^3kg^{-1}s^{-2}$
Velocity of light	c	2.99792458×10^8	m s^{-1}
Stefan-Boltzmann constant	σ	5.66956×10^{-8}	W m^{-2} K^{-4}

Symbols

Name	Symbol	Units
Wavelength	λ	Å
Effective temperature	T_{eff}	K
Stellar luminosity	L	$L_\odot$
Stellar mass	M	$M_\odot$
Stellar radius	R	$R_\odot$
Surface gravity	$\log g$	[cm s^{-2}]
Period	P	days
Mass ratio	q	
Inclination	i	°(degree)
Semi-major axis	a	$R_\odot$
Centre-of-mass velocity	γ	km/s
First Lagrangian point	L_1	
Second Lagrangian point	L_2	

1 Introduction

> Do not look at stars as bright spots only. Try to take in the vastness of the Universe.
>
> *Maria Mitchell, Astronomer*

Long before modern telescopes started to reveal the secrets of the Universe, stars already played an important role in ancient civilisations and cultures. The image of the stars on the night sky was so imposing, some cultures believed the stars to be Gods. Others created legends of how they formed, naming constellations after mythological creatures. These stories and names would last for centuries and are still used up to today.

The ancient wondering about the twinkling diamonds in the night sky has led to many theories and mythologies, but only after the invention of telescopes the truth behind these stories was revealed. It became clear these diamonds were balls of hot gas, living alone or with close neighbours. By analysing the light of these hot gaseous balls, astronomers could reveal characteristics of the stellar interior. Slowly but steadily astronomy became a modern science and it allowed mankind to discover its place in the Universe and understand its surroundings. Telescopes would probe deeper and deeper, offering a unique opportunity to look into the vast darkness between the stars, to look at the early Universe and its first components.

It is thought that extremely massive stars with masses higher than one thousand times the mass of the Sun (Loeb and Barkana, 2001) have been amongst the first stars in the Universe. These first stars were born in an environment with only the elements created in the Big Bang: approximately 75% hydrogen (H) and 25% helium (He), and small trace amounts of lithium, beryllium and boron.

The present Universe however holds many more elements and without them the world that we know would not have been. In some way, the Universe created these so-called metals, which is the astronomical name for

elements heavier than helium. These elements were created in the heart of the first stars: in their cores. With the death of the first stars, the first metals were spread across the Universe. New generations of stars were born out of this enriched material. Following the footsteps of their predecessors, they in turn also chemically enriched the Universe. Generation after generation the stars were born with more metals in their interiors and massive stars became less and less present.

Whilst massive stars are thought to have been common in the early Universe, nowadays massive stars are rare. The distribution of stellar masses is determined by the initial mass function. In 1955, E. Salpeter determined the initial mass function of the Galaxy[1] and found that the number of stars with a certain mass is a rapidly decreasing function of mass. For every star that is born with a mass 20 times that of the Sun, there are about 1 000 Suns. Nonetheless, most of the heavy metals are produced in massive stars. Chemically enriching the Universe is only one of the important things these massive stars do. The intense radiation field of massive stars ionises the gas around them and influences star formation in their surroundings. It is for this reason that they are also referred to as *cosmic engines* (Bresolin et al., 2008). On top of that, they end their lives with powerful supernova explosions, leaving behind compact objects: neutron stars and black holes. The merger events of these compact objects are nowadays regularly observed with gravitational wave detectors.

Unfortunately, massive stars are rare and a lack of (observational) constraints on their parameters makes it difficult to fully perceive the evolution of these building blocks of the Universe. Some of the most pressing questions are: How do the most massive stars evolve? How do they impact star formation? And what is the upper limit of stellar masses? In order to answer these questions, the cosmic engines need to be monitored and analysed in every stage of their evolution. Understanding them is critical if we want to model the evolution of our Galaxy and the Universe.

In this thesis, I bring astronomers one step closer to constraining the uncertainties that are present, as I investigate a rare multiple system of massive stars - a system with multiple massive stars that are assumed to be gravitationally bound to each other. One might wonder what the analysis of one single system of massive stars could mean to the astronomical community. The answer is very simple: Massive stars are rare and every observational constraint matters. Moreover, multiple systems offer precious laboratories to (accurately) obtain stellar parameters (Chapter 4). These parameters can then be used to test models and refine them where necessary.

[1]When talking about galaxy with a capital (Galaxy) astronomers refer to our own Milky Way.

The multiple system analysed here is called BAT99 126. It is located in the Large Magellanic Cloud (LMC), the most massive satellite galaxy of our Milky Way. At a distance of over 150 000 light years (Pietrzyński et al., 2013), it is also one of the closest satellite galaxies to the Milky Way (Karachentsev et al., 2004). The LMC is an active star-forming region. Robert Burnham (1978) referred to the LMC as an "astronomical treasure-house, a great celestial laboratory for the study of the growth and evolution of the star". Not only that, it is also an interesting environment because it is less chemically enriched than the Milky Way. A study of the LMC allows for a study of stellar objects with a different metal content in their interior and the influence thereof on the stellar parameters.

There are two things which make BAT99 126 an important system to study as it hosts:

- a Wolf-Rayet (WR) star. This star is an even rarer type of evolved massive star, discussed in more detail in Section 2.5. Only $\sim$ 1 000 WR stars are known in the Milky Way and merely $\sim$ 150 in the LMC (Neugent et al., 2018).
- a very short-period binary, with a period of 1.55 days (Graczyk et al., 2011). Very close binaries are important for evolutionary studies (Chapter 4).

Because of its properties, BAT99 126 was thought to be a prototypical example of a black-hole + black-hole merger, which are now routinely being observed by gravitational wave detectors. For this reason, high-quality data were collected to study this system in more detail.

The overarching goal of this thesis is to perform a comprehensive analysis of BAT99 126 and establish the evolutionary state of the system. This goal is reached in three steps:

1. Identify the multiplicity of the system and determine the spectral types of the individual components[2].
2. Establish the orbital configuration of the system and simultaneously derive accurate masses for its components.
3. Determine the age of the system and perform tailored modelling to establish the evolutionary state of the system.

This thesis is divided into two major parts. The first part goes through the fundamental knowledge necessary to understand the working methods used in this thesis. Throughout the chapters it will become clear where

[2]The spectral type of a star is a way of grouping stars with similar radiation profiles together. It is explained in more detail in Section 2.1.

the deficiencies in massive-star evolution theory are located as well as the importance of massive stars. The part on fundamental astronomy ends with a brief overview of the research already performed on BAT99 126. The second part explains the analysis and results, starting with a presentation of the available data and ending with the conclusion and outlook after the work performed in this thesis.

Part I

Fundamental astronomy

Stars, just like humans, are born and will eventually die. The reason for their birth, being gravitational contraction, is also the cause of their death. Because of this contraction, the core of stars can grow hot enough for nuclear fusion reactions to take place. A star is born when the heat from nuclear reactions counteracts the gravitational contraction and it dies when there is no more fuel available to sustain the gravitational pressure. Their evolution and ending are dependent on certain stellar parameters, one of them being their *initial mass*. The evolution of single massive stars is first discussed in Chapter 2 - or at least how it is commonly thought they evolve, starting with a few words on why massive stars are classified as such. The stellar parameters that describe (the evolution of) a star are given in Chapter 3, together with the information necessary to understand stellar atmospheres and winds in the context of this thesis.

An important aspect to the evolution of massive stars is a nearby companion. The evolution of massive stars in a binary system is explained in Chapter 4.

This part ends with a brief introduction on previous research that has been performed on BAT99 126, our target of study, and summarises its implications.

2 Single-massive-star evolution

Massive stars, or stars born with masses larger than eight times the mass of the Sun ($M_{\text{initial}} > 8M_{\odot}$), have a lifetime of $\tau \sim 10^7$ years. For us this might seem long, but compared to the Sun ($\tau \sim 10^{10}$ years) this is very short. The lifetime of a star is determined by the ratio of the amount of fuel the star has and its luminosity, i.e. how much energy it irradiates. The fuel for a star primarily consists of hydrogen, however during later stages in its evolution heavier elements will take over that role. The amount of fuel that a star can use during its lifetime is proportional to its mass. As heavier stars are also more luminous, they require more energy to sustain this luminosity and hence burn through all their energy faster. The lifetime of a star thus decreases with increasing mass (see also Section 3.2). In their short lives, however, massive stars have a major impact on their surroundings. Their intense radiation fields ionise the interstellar matter and blow away gas and dust in their surroundings, impacting star formation. The most massive stars have strong stellar winds which blow away a significant amount of mass from their stellar surface back into space. By ending their lives with a supernova explosion, they eject incredible amounts of enriched material into interstellar space. With all these aspects combined, massive stars have a considerable influence on their environment both mechanically and by radiation, driving the evolution of the Universe (e.g. Heckman et al., 1990; Bresolin et al., 2008; Hopkins, 2014).

Massive stars will follow a different evolutionary path compared to their less massive counterparts. The latter are called low- and intermediate-mass stars. These less massive stars do not end their lives with supernova explosions and do not become compact objects. In Section 2.4, it is briefly explained how they end their lives and why astronomers make the difference between massive stars and low- and intermediate-mass stars. The complete evolution of low- and intermediate-mass stars is however not outlined here, for an excellent overview of their evolution the reader is referred to Kippenhahn et al. (2012).

This chapter is mostly based on the lecture notes of the course *Stellar structure and evolution*, taught at KULeuven (by Prof. C. Aerts).

2.1 The Hertzsprung-Russell diagram

The Hertzsprung-Russell diagram (HRD) is an important tool for studying the evolution of stars. The HRD shows the luminosity as a function of effective temperature. The luminosity is a measure of the brightness of a star and is dependent on the radius of the star and its effective temperature. The effective temperature is a measure of the surface temperature of a star (see Section 3.1 for further information on the parameters). A schematic HRD is shown in Figure 2.1. The position of some well known stars is indicated as well. We can distinguish four groups: the main sequence (the diagonal from the upper left to the lower right corner), giants, supergiants and white dwarfs.

Spectral classification

The spectrum of a star can be seen as a bar-code. Just as a scanning machine knows which product is scanned, astronomers can identify stars by looking at their spectra. Different groups of stars have similar spectra and are identified accordingly. These groups are also related to the temperature of the stars (see Section 3.4) and their evolutionary state.

A well-known example of a star is the one closest to us: the Sun. The Sun is classified as a G2 V star. The letter 'G' refers to the spectral type of the Sun. The spectral types are mostly an indicator of the temperature of the stellar surface. In Figure 2.1, the hottest and most luminous stars are O-type stars, with effective temperatures typically between 30 000 and 50 000 K. They are hence located in the upper left corner of the HRD. Then follow the B-type stars with effective temperatures between 12 000 and 30 000 K. In descending order of temperature other spectral types are A, F, G, K and M [1]. The effective temperature of the Sun is $\sim$ 5780 K. The spectral types are also indicated in the HRD in Figure 2.1.

The number '2' indicates the sub-class the Sun belongs to. Each spectral class is subdivided in sub-classes (O2-9.7, B0-9, A0-8, F0-9, G0-9, K0-5, M0-9). For each of these sub-classes there are subtle differences in the spectrum.

O-, B- and A-type stars are referred to as early-type stars. The other spectral types are referred to as late-types. Although these two words are

[1] One way of remembering the spectral sequence is the mnemonic "Oh Be A Fine Girl Kiss Me".

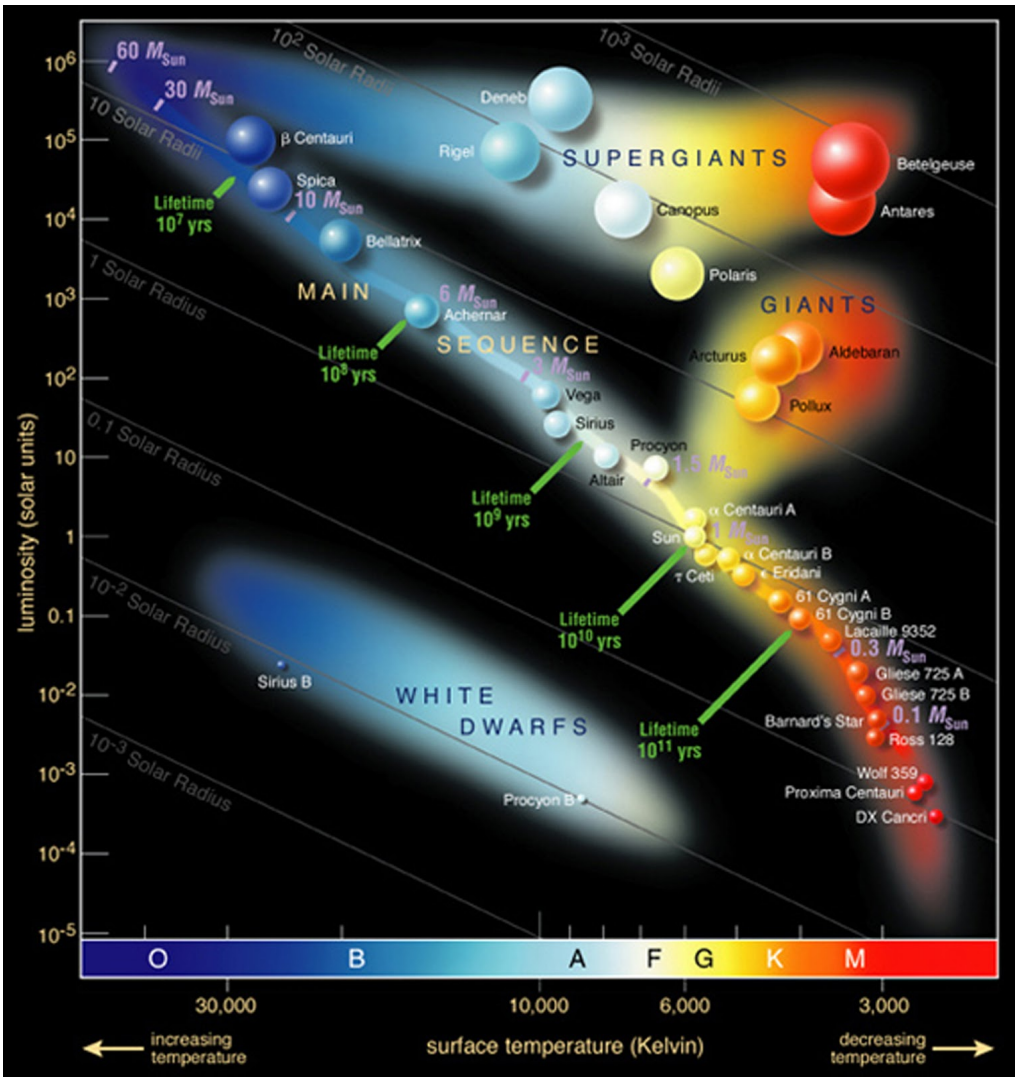

Figure 2.1: The HRD showing the luminosity in terms of the solar luminosity and the effective temperature of stars. We distinguish four clear categories: the main sequence (the diagonal from the upper left to the lower right), giants, supergiants and white dwarfs. Spectral types are also indicated, as well as masses and lifetimes. The position of some well known stars is indicated. Figure credits: ESO, `https://www.eso.org/public/images/eso0728c/`

used as timestamps in daily life, they have nothing to do with the age of the stars. Instead, the terms 'early' and 'late' are a synonym of 'hot' and 'cool' respectively. Hot stars are also referred to as 'blue' stars and cool stars are called 'red' stars. This originates from Wien's displacement law, which roughly determines at which wavelength a star radiates the most intensely (see Section 3.1 and 3.4). The intensity of the radiation emitted by hot stars peaks at wavelengths closer to the blue whereas for cool stars their intensity peaks near red wavelengths, hence the nomenclature. The terms 'early' and 'late' can also be used inside each spectral class, such that spectral type O6 is later than O5.

O-type and early B-type stars are classified as massive stars. All spectral types later than B3 are defined as low- and intermediate-mass stars [2].

Finally, the Roman number 'V' in the classification of the Sun (G2 V) is an indication of the evolutionary state of the Sun and is called the luminosity class. In this case, the Sun is still on the main sequence (Section 2.3). This is a reference towards the radius of the star. As will become more clear in the next sections, this also refers to the evolutionary state of the star. It is indicated with a Roman number after the spectral classification: 'I' for supergiant, 'II' for bright giant, 'III' for giant, 'IV' for subgiant and 'V' for dwarf.

2.2 Birth of a star

Although the night sky looks pretty crowded, most of it is empty space. Most of the visible matter is either located in stars or in interstellar gas clouds. These clouds come in all shapes and sizes, but not all fulfill the conditions that are necessary to further evolve into stars.

Stars are born out of dense interstellar gas clouds, with the number of particles per volume $\gtrsim 10^3$ cm^{-3}. Due to their high density the inside of these clouds is shielded from interstellar radiation and hence they are called cool ($\sim$20 K) molecular gas clouds. When such a cloud is massive enough, it becomes unstable to gravitational contraction. A common criterion to determine the stability of a cloud is the *Jeans mass*, established by J. Jeans in the early 1900's. The contraction will lead to fragmentation of the original cloud in small clumps, which also continue to get fragmented into smaller pieces. This process is called *hierarchical fragmentation*. The clumps keep on fragmenting until the individual clumps reach masses low enough to stop this fragmentation. The clumps now contract until a mas-

[2]Stars with masses ($M_{\rm initial} < 0.08 M_\odot$) never reach a temperature high enough to fuse hydrogen into helium. These stars are called brown dwarfs and are sometimes also referred to as 'failed stars'.

sive core, the so-called protostar, surrounded by a disk, will assemble in each clump. The protostar will heat up due to gravitational contraction and accretion of material in the disk. If the original clump was massive enough, the protostar will start fusing hydrogen into helium. These and other nuclear reactions will become the main source of energy for the star to counterbalance the gravitational force.

At the point when the nuclear reactions become the dominant energy source over the energy released from the contraction, the star reaches the zero-age main sequence. A star is born and it now begins its evolution on the main sequence. A schematic overview of this star-formation process is given in Figure 2.2.

2.3 Main sequence

From the moment stars are born, their fate is set. That is, unless they are influenced by their surroundings. But for now let us assume that there is nothing in the neighborhood of the star that might alter its evolution.

Stars on the main sequence fuse hydrogen into helium in their core. There are two processes resulting in the burning of hydrogen: the proton-proton (pp) chain and the carbon-nitrogen-oxygen (CNO) cycle. Both reactions have the same end result: the fusion of four protons into a helium atom. The pp-chain is not dependent on other elements. The CNO cycle on the other hand uses C, N and O to produce a He atom. The abundances of these elements partly determines the efficiency of the cycle. Furthermore, the efficiency of the CNO cycle is much more temperature-dependent than that of the pp-chain. This means that for a slight increase in temperature the efficiency of the CNO cycle will increase more relative to the efficiency of the pp-chain. This is why for stars with $M > 2M_{\odot}$ the CNO cycle is the dominating hydrogen-burning process, whereas for stars $M < 2M_{\odot}$ the pp-chain is the dominating energy source.

The main sequence is the diagonal band going from the upper-left to the bottom-right corner in the HRD in Figure 2.1. The reason why the main sequence is a band and not a fine line is explained later on in this chapter. A star will spend almost its entire life on the main sequence burning hydrogen. Most stars we observe are main-sequence stars. Main-sequence stars are typically observed as dwarfs, that is, stars with a luminosity class 'V' (see Section 2.1).

The luminosity and effective temperature of a star are related to the mass (Section 3.1). Depending on its initial mass the star will start its life on the main sequence at a different position. As indicated previously, the more massive the star, the higher the effective temperature and luminosity will

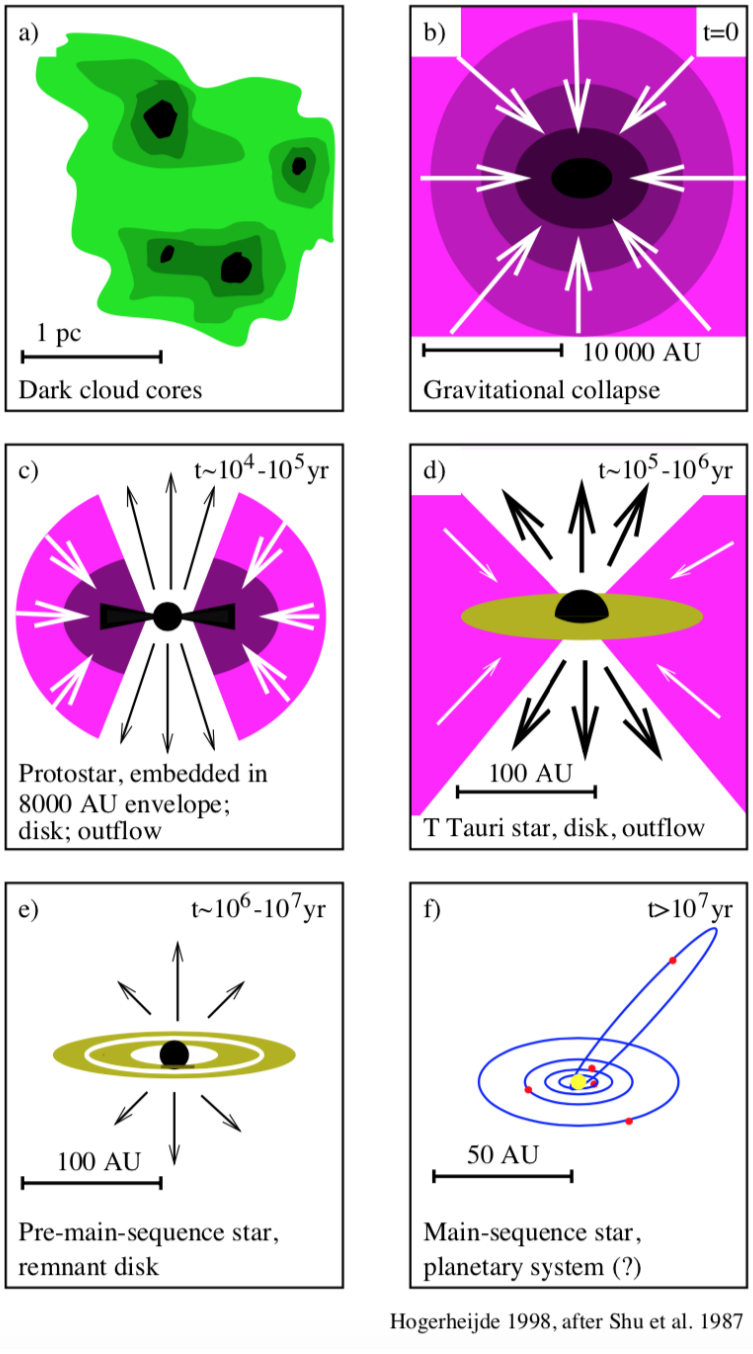

Figure 2.2: The different stages of star formation. a) Fragmentation of the cloud and formation of clumps. b) Gravitational collapse of the clump. c) A protostar is formed with circumstellar material. d+e) Material forms in a circumstellar disk and is accreted/radiated away. f) A star is formed, with possible planet formation from the remaining disk. Figure taken from the PhD thesis of M. Hogerheijde (University of Leiden).

be at the start of its life. Hence the closer the star will be located towards the top-left corner in the HRD.

Energy transport in the stellar interior

The energy transport from the core (where the nuclear reactions take place) to the surface (where light escapes) can be either radiative or convective. The latter happens when radiation alone is not sufficient to carry away all the produced energy. Mass elements with a temperature higher than their surroundings rise to the stellar surface and consequently dissipate. If radiative energy transfer becomes efficient enough to carry away all the energy through the stellar interior, no convection will occur.

An example of why radiation alone is not sufficient to carry away all the energy is because the opacity in the stellar envelope becomes very large. More radiation will interact with atoms in the ground state than they will with ions. When the stellar envelope is cool enough for metals to be in their ground state, it hence becomes opaque and convection sets in. The convective regions in the star are those regions where convection is the main source of energy transport due to a high opacity. Likewise, the radiative regions are those where radiation is the main source of energy transport and where no convection is necessary.

If there were two stars with identical initial masses, but one has a radiative envelope (all the material outside of the core) and the other a convective envelope, the star with the convective envelope would be larger in size. The temperature gradient inside the star is smaller for convection than for radiative transport. In order to have the same effective temperature, stars with convective envelopes will need to have a larger radius as the particles in the envelope need a longer path to cool down.

The internal structure of the star on the main sequence, shown in Figure 2.3, is also mass-dependent. Stars with $M_{\text{initial}} \lesssim 0.5 M_{\odot}$ are fully convective. The stellar material is fully mixed and they will burn up all the hydrogen they have. Stars with $0.5 M_{\odot} \lesssim M_{\text{initial}} \lesssim 1 M_{\odot}$ have convective envelopes and radiative cores. The material in their core is not mixed and a chemical gradient builds up in their core during their evolution. A chemical gradient is a measure of the difference in chemical composition between two adjacent stellar layers. For stars with $M_{\text{initial}} \gtrsim 1 M_{\odot}$ the core is convective and the envelope is (partly) radiative. This means that the core of these stars constantly mixes the material. They will burn through all hydrogen in their core. The convective core combined with the radiative envelope will show to have an influence on their further evolution (see Section 2.6).

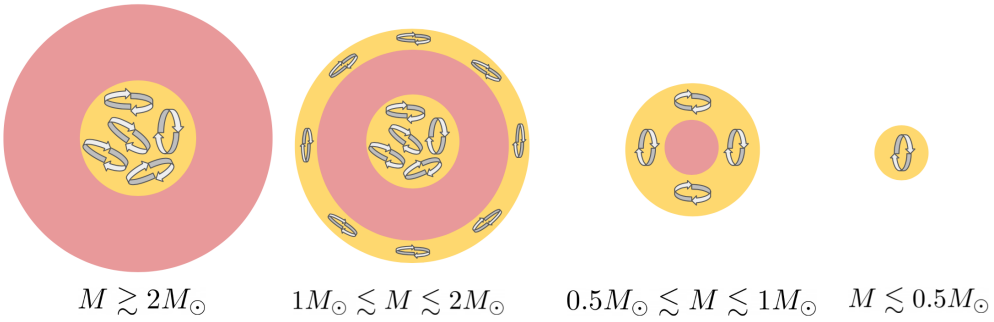

Figure 2.3: Schematic representation of the stellar structure of stars with $M_{\text{initial}} \gtrsim 2M_\odot$ (left most), $1M_\odot \lesssim M_{\text{initial}} \lesssim 2M_\odot$ (second from left), $0.5M_\odot \lesssim M_{\text{initial}} \lesssim 1M_\odot$ (third from left) and $M_{\text{initial}} \lesssim 0.5M_\odot$ (most right) on the (zero-age) main sequence. Red regions are radiative regions and yellow arrowed regions are convective.

2.4 Further evolution

Whilst discussing the further evolution of massive stars, it will become clear why astronomers distinguish between massive stars and low- and intermediate-mass stars. In the class of massive stars, we distinguish between two subclasses: stars with $8M_\odot \lesssim M_{\text{initial}} \lesssim 15M_\odot$ and stars with $M_{\text{initial}} \gtrsim 15M_\odot$.

2.4.1 Stars with $8\mathbf{M}_\odot \lesssim \mathbf{M}_{\text{initial}} \lesssim 15\mathbf{M}_\odot$

After hydrogen exhaustion in the core, the star reaches the terminal-age main sequence. The star is left with a helium core. There is a limiting mass for the helium core above which it will start to contract in the absence of another energy source due to the weight of the overlying layers. This limit is called the *Schönberg-Chandrasekhar limit*. It is typically about 7-15% of the total mass of the star. Stars with $M_{\text{initial}} \gtrsim 2.3M_\odot$ will have helium cores above this mass. Hence their core starts contracting after reaching the terminal-age main sequence. The temperature in the stellar interior increases as a result of this contraction. A shell surrounding the core now becomes hot enough to initiate hydrogen burning. This is called hydrogen shell-burning. Hydrogen shell-burning provides extra helium to the already shrinking core. This increase of mass leads to an even faster shrinking of the helium core.

The shrinking of the core leads to an increase of the temperature in the core and to an increase in luminosity. The outer layers of the star start expanding as a result of the sudden increase in luminosity. The outer layers cool down due to the enormous expansion: the star becomes a red supergiant. The outer layers of the star have now become convective. During

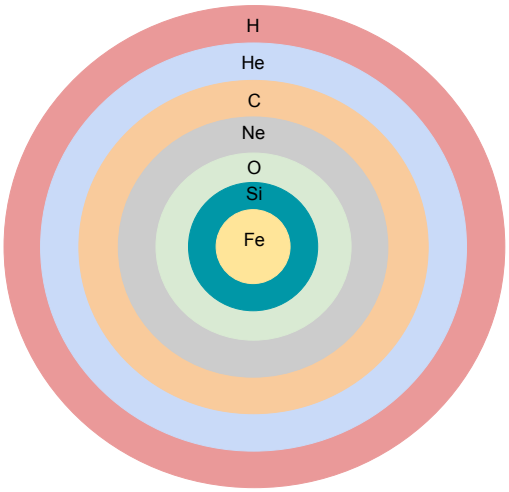

Figure 2.4: A schematic representation of the onion model in an evolved massive star. Shells are not to scale.

the process, the star is moving to the right in the HRD.

The core stops contracting once it reaches a temperature high enough to start helium burning. A new burning cycle has begun. The end product of helium burning or the triple-α process is mostly carbon and oxygen and a CO core forms.

When helium is depleted in the core, the core starts contracting again. Helium shell-burning starts in a thin layer around the core. Hydrogen shell-burning starts in a thin layer around the helium-burning layer. Eventually the core starts burning the carbon and oxygen produced by the previous helium fusion. When also C and O are depleted a new cycle begins. This process is repeated until the core consists fully of iron. After every phase of core-burning a phase of shell-burning occurs. The result of the subsequent layering of these shell-burnings is called the *onion model*. A schematic representation of the onion model of an evolved massive star is shown in Figure 2.4.

As opposed to stars with $M_{\text{initial}} \lesssim 8M_{\odot}$, massive stars will go through all burning cycles. Almost all low- and intermediate-mass stars will never reach CO burning. They end their life as a degenerate electron gas. This is caused by the Pauli exclusion principle, which states that no two identical fermions (e.g. electrons, protons or neutrons) can be in the same state. As the core of lower-mass stars contracts, the electrons are being pushed so closely together that the Pauli exclusion principle sets in. The gas becomes degenerate. The electrons now provide a pressure that counteracts the gravitational contraction. These objects are called white dwarfs. They are dying low- and intermediate-mass stars, as they radiate away the heat that is left from the contraction.

The final burning cycle for massive stars is that of silicon (Si) into iron (Fe). No more fusion reactions take place after that, as the fusion of Fe requires energy instead of releasing energy. With no energy to counteract the gravitational pressure, the star quickly collapses. As the core collapses, the material in the envelope is accelerated towards its centre. It comes to a sudden halt when reaching the dense core. The kinetic energy of the particles in the envelope is converted into thermal energy. The core is heated up and reaches temperatures higher than 10^9 K. These high temperatures lead to the dissociation of the heavy core elements into helium atoms, which requires energy. The energy is provided by the contraction of the core, which is accelerated by the process. The contraction in turn leads to even higher temperatures. Helium atoms are now also converted into protons and neutrons. The whole process of fusion is undone in less than a second.

The dissociation process also leads to a significant enhancement of the density in the core as all atoms are now replaced by their individual electrons, protons and neutrons. This high density results in the recombination of electrons and protons into neutrons. The neutrons collide with each other and create a shock wave that moves through the outer stellar layers. The star explodes as a supernova, ejecting an incredible amount of chemical elements into the interstellar space ready to be used up in the creation of new stars. This supernova results in magnificent images. A well-known example is the Crab nebula, shown in Figure 2.5.

What remains after the core-collapse supernova of stars with $8M_\odot \lesssim M_{\rm initial} \lesssim 15M_\odot$ is a neutron star (NS). This is a degenerate compact object. In the case of a neutron star, it is the neutrons which are degenerate. The object becomes so compact due to the gravitational force, that the neutrons will experience the effects of the Pauli exclusion principle. Hence the result is a NS.

A typical neutron star has $1.4M_\odot < M_{\rm initial} < 2M_\odot$ (e.g. Rezzolla et al., 2018). They are very fast rotators, which comes from conservation of angular momentum when a star with a radius $R > 10^6$ km collapses to a compact object with $R \sim 10$ km. Even the slightest rotation of the progenitor star will result in a very fast-rotating NS. Typical rotational velocities are of the order of milliseconds.

2.4.2 Stars with $\mathbf{M_{initial} \gtrsim 15M_\odot}$

The main difference between stars with $M_{\rm initial} \gtrsim 15M_\odot$ and stars with a lower mass is the strength of their stellar winds. Although all stars have particles which flow away from the stellar surface, only for stars with $M_{\rm initial} \gtrsim 15M_\odot$ these winds are significant enough to influence the evo-

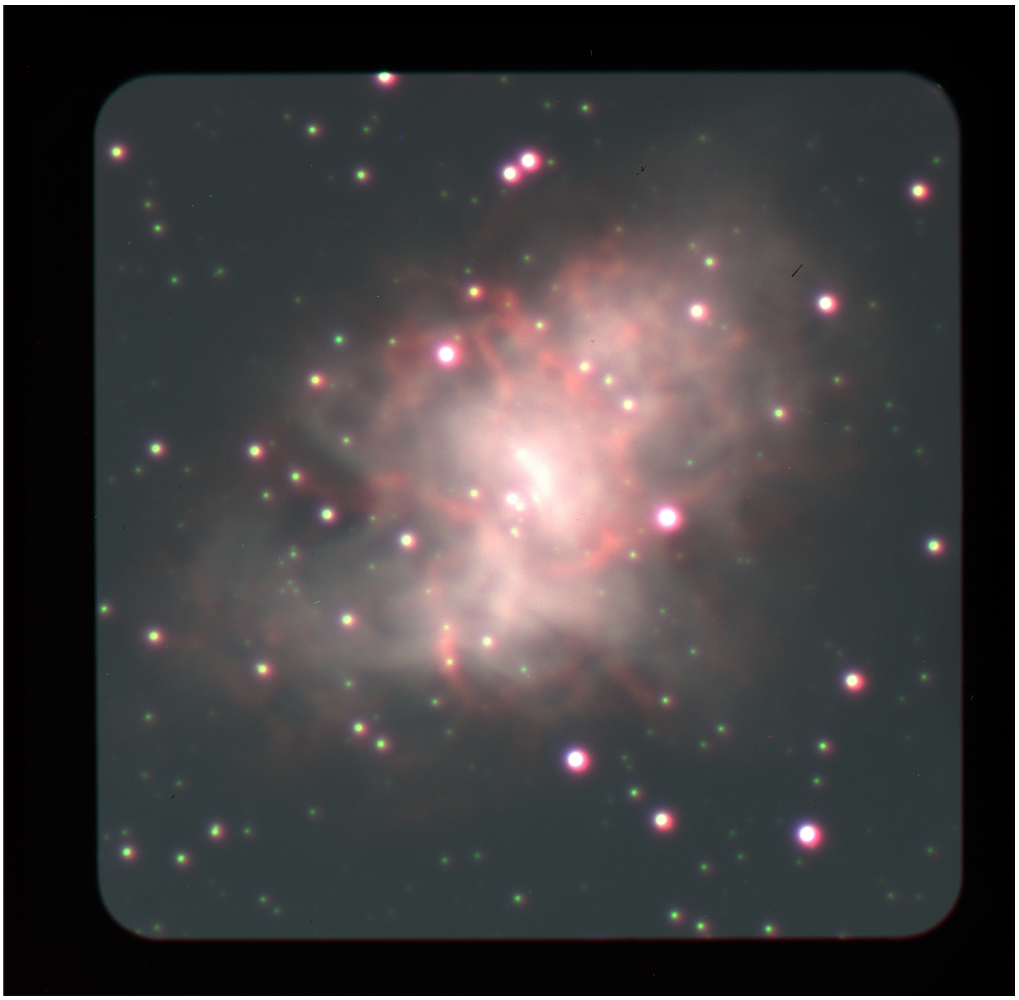

Figure 2.5: Snapshot of the Crab nebula taken with the Northern Optical Telescope on La Palma in November 2019. The bright spots are stars in the field of view. Image taken and constructed by Soetkin Janssens, Pablo Calabretto, Juha-Pekka Virtanen, Mikko Pöntinen and Tuomas Salo.

lution of the star[3]. A star with $M_{\text{initial}} = 15M_{\odot}$ has a mass-loss rate of $\sim 10^{-8}M_{\odot}$ per year (/yr) on the main sequence, whereas a $40M_{\odot}$-star will lose already $\sim 10^{-6}M_{\odot}$/yr on the main sequence (Vink et al., 2000). More massive stars will even have stronger winds. For a main-sequence life-time of $\sim 10^{7}$ years, a $40M_{\odot}$-star loses about one-fourth of its mass during its main-sequence evolution due to stellar winds. The impact of these winds can thus not be neglected.

The winds of stars with $15M_{\odot} \lesssim M_{\text{initial}} \lesssim 25M_{\odot}$ lead to a significant amount of mass loss during their evolution, but not significant enough to greatly alter their evolution compared to stars with $8M_{\odot} \lesssim M_{\text{initial}} \lesssim 15M_{\odot}$. They will most likely also end their lives as a NS.

The stellar winds of stars with $M_{\text{initial}} > 60M_{\odot}$ are so powerful during the main-sequence and hydrogen-shell burning stage that their entire hydrogen-rich envelope is blown away during their evolution. What remains is a naked helium core. As the extremely hot core of the star is exposed, it will reside the rest of its evolution in the blue part of the HRD in Figure 2.1.

The evolution of stars with $25M_{\odot} \lesssim M_{\text{initial}} \lesssim 60M_{\odot}$ is uncertain. According to a commonly accepted scenario (Conti et al., 2008) the winds of these stars during the part of their lives on the main sequence are not powerful enough to blow away the entire envelope. Just as for lower-mass stars, these stars will expand when hydrogen shell-burning is initiated. The star quickly becomes a red supergiant. As the star becomes so large, its luminosity approaches the *Eddington limit*. This is the maximum luminosity a star with a certain mass can have such that gravity can still hold all the material together. If a star approaches this limit any small perturbation will lead to extreme amounts of mass loss. Shortly after hydrogen shell-burning is initiated, the star becomes unstable and becomes a luminous blue variable (LBV) star. LBVs are characterised by powerful stellar outflows. The star is losing $\sim 10^{-4}M_{\odot}$/yr. The LBV stage only lasts about 10 000 years. During this stage the star loses so much mass that the expansion stops. The convection in the envelopes of these stars cannot happen in equilibrium anymore. The envelope contracts until it reaches radiative equilibrium again. In other words, the radius decreases and the contraction heats up the star. The star can thus not remain a red supergiant due to all the mass loss and it moves back to the blue part of the HRD. For the most massive (and luminous) stars, red giants are thus not present in the

[3]The Sun also generates a wind. An example of this is the Aurora Borealis or northern lights, which is a result of solar particles interacting with Earth's atmosphere. However the mass loss during the main-sequence evolution of the Sun is very insignificant.

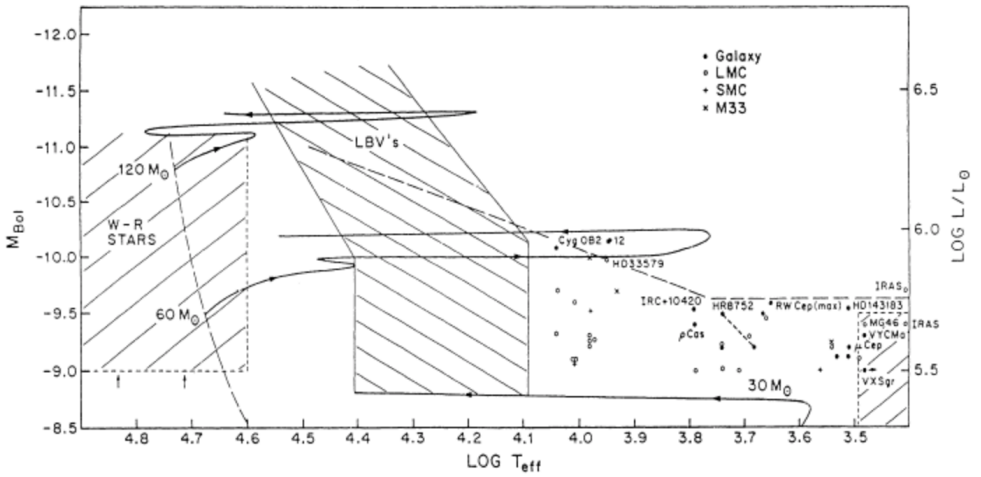

Figure 2.6: Evolutionary tracks for massive stars, as a function of effective temperature ($T_{\rm eff}$). Supergiants from four different galaxies are plotted in the diagram. The regions where LBVs and WR stars are seen in the HRD are indicated. Three evolutionary tracks are shown as well. The Humphreys-Davidson limit is indicated with the dashed line. The left y-axis shows the bolometric magnitude, which is a logarithmic inverse measure of the luminosity, shown on the right y-axis. Figure taken from Humphreys (1987).

HRD. The limiting luminosity and effective temperature combination above which red supergiants are not observed is called the *Humphreys-Davidson limit*. Figure 2.6 shows supergiants from four different galaxies: the Milky Way, the LMC, the Small Magellanic Cloud (SMC) and Messier33 (M33), which is the second closest Milky-Way-like galaxy. The left y-axis shows the bolometric magnitude, which is a logarithmic inverse measure of the luminosity, which is shown on the right y-axis. The Humphreys-Davidson limit is indicated with a dashed line, starting from the right around a bolometric magnitude of -9.6 and $\log L/L_{\odot} \approx 6.7/8$ staying constant up until effective temperatures of about 5 700 K. After that, the limit rises diagonally upwards, as the effective temperature increases. It can be seen that no red supergiants are observed above the limit.

As the star is moving back to the blue part of the HRD, it becomes a Wolf-Rayet (WR) star. Mass-loss rates during this stage can reach $\sim 10^{-5} M_{\odot}$/yr. This stage is also short-lived. The WR stars are explained in more detail in the next section. Stars with $25 M_{\odot} \lesssim M_{\rm initial} \lesssim 60 M_{\odot}$ will also evolve further towards a collapse of their iron core.

The evolution of the more massive stars can be summarised as

$$\text{O} \rightarrow \text{LBV} \rightarrow \text{WR} \rightarrow \text{core-collapse supernova.}$$

The gravitational contraction force of stars with $M_{\rm initial} \gtrsim 25 M_{\odot}$ is so strong that even the neutrons cannot provide enough pressure to counteract

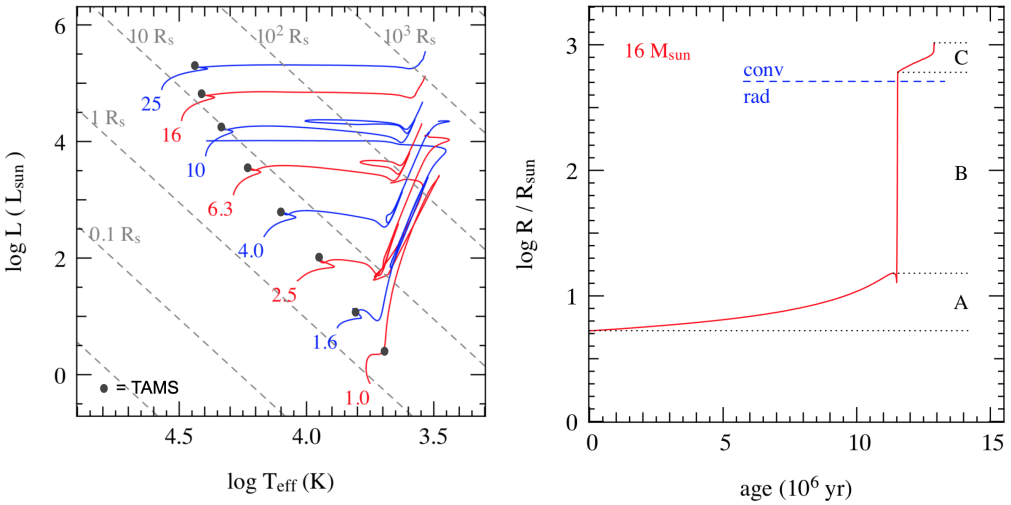

Figure 2.7: Left: Evolutionary tracks for stars with $1M_{\odot} \leq M_{\text{initial}} \leq 25M_{\odot}$. Diagonal dashed lines show the radius of the star. The terminal-age main sequence is indicated with a grey dot, labelled TAMS. Right: radius as a function of age for a $16M_{\odot}$ star. Region A indicates the main sequence, region B hydrogen shell-burning and region C core-helium burning. Figures taken from Prof. O. Pols' lecture notes.

it. The core collapses further and forms a black hole (BH). BHs typically have masses $> 2M_{\odot}$.

2.4.3 Radial expansion

Over its whole life, the radius of a star will increase significantly. Not only will the radius greatly expand during transition periods towards the (super)giant stage, but also during the main sequence the star will slightly evolve. As the stars burn through the hydrogen in their cores the chemical composition changes as the hydrogen in the core becomes less abundant. Consequently, the fusion rate gradually decreases. Fewer fusion reactions mean less energy production. The core will slightly contract, making it hotter and more luminous. This leads to an expansion of the envelope and a slight increase in radius. The left panel of Figure 2.7 shows evolutionary tracks for stars with $M \leq 25M_{\odot}$. Dashed lines indicate the radius of the star during its evolution. The end of the main sequence is indicated with a grey dot, labelled TAMS. It can be seen that the star already expands during the main sequence. The right panel of Figure 2.7 shows the radius as a function of the age of the star. Region A indicates the main sequence, region B hydrogen shell-burning and region C core-helium burning.

2.5 Wolf-Rayet stars

Wolf-Rayet (WR) stars are very rare: they are a part of the evolution of rare massive stars and it is only the most massive stars which will reach this stage. Moreover, the WR phase lasts only about 500 000 years. This is why only about a thousand of them are known today. It is a very critical stage in massive-star evolution as large amounts of mass are lost from the stars' surface ($10^{-4} M_{\odot}$/yr compared to $\sim 10^{-7} M_{\odot}$/yr during the main sequence. For the most massive stars, it is the final stage in their evolution, but that certainly does not make it the least important.

In 1867, French astronomers Charles Wolf and Georges Rayet observed for the first time stars with spectra which differed very strongly from normal main-sequence stars. Instead of narrow absorption lines, their spectra were dominated by very broad emission lines (see Section 3.4). These stars are since then known as WR stars. Their broad emission lines originate from the strong stellar winds that characterise all WR stars. Their winds result in mass-loss rates of $10^{-4} - 10^{-5} M_{\odot}$/yr (e.g. Nugis and Lamers, 2002). The particles in these winds can reach velocities higher than $\sim$ 3 000 km/s (e.g. Niedzielski and Skorzynski, 2002). The broadness of the spectral lines is a result of these high wind velocities. Probing the star becomes difficult as the dense material from the winds prevents an observer from looking directly at the star. The naked helium core that remains from the star is hidden behind the opaque wind material. A WR star can reach extremely high effective temperatures of $\sim 10^4 - 10^5 K$, much hotter than common O-type main-sequence stars. Their luminosities reach $L \sim 10^5 L_{\odot}$, which approach the Eddington limit.

The WR stars are subdivided into three classes: the nitrogen sequence (WN), the carbon sequence (WC) and the rare oxygen sequence (WO), based on whether the composition of their atmospheres is nitrogen-rich (from CNO cycle products) or carbon-/oxygen-rich (from He-burning products). The WN stars are early type and the WC/WO stars are late type. Sub-types of the WN and WC are: WN3-8 and WC5-9. A WN and WC star represent two different evolutionary stages. These three WR classes are thought to correspond to an evolutionary sequence of a WR star (Crowther, 2007):

$$\text{WN} \rightarrow \text{WC} \rightarrow \text{WO}.$$

There are two mechanisms which can drive such powerful stellar outflows: the internal radiation field and after interaction with a companion. The winds of massive stars are radiation-driven and the mechanism behind them

is explained in Section 3.3. The powerful WR winds can indeed be induced by the star itself. On the other hand, if a massive star has a companion close enough, the companion might strip the star revealing the hot stellar interior of the massive star. The hot star will develop a radiative-driven wind as it approaches the Eddington luminosity and evolve into a WR star. When a star is in orbit with another star - which is called a binary - there is the possibility that the winds are the result of interactions between the two stars. As the massive star transfers mass to its companion, it might approach the Eddington luminosity and appear as a WR star (Paczyński, 1967). Binary interactions are explained more in detail in Chapter 4.

2.6 Effect of mixing and metallicity

It was shown that stars with $M_{\text{initial}} \gtrsim 2M_{\odot}$ have a convective core and a fully radiative envelope on the main sequence (Figure 2.3). When one looks at a pot of boiling water, the rising gas bubbles do not stop precisely at the water surface. Instead they can be seen to shoot through the water surface. For stars with a convective core, the gas elements are also thought to overshoot the core boundary. If the gas elements overshoot this boundary, they bring new hydrogen-rich material into the core material that would otherwise never be used for fusion. This implies that the star will have more hydrogen to burn and live longer. How far into the radiative envelope this overshooting penetrates is however not well established and was already debated in the 1980's (Eggleton, 1983b, and references therein). Up until today the amount of overshooting is still not well established.

Another example of internal mixing is rotational mixing. Fast rotation of stars induces flows in the stellar envelope and mixes the material. The efficiency of this rotational mixing is however not well established and is a decades-old problem (Maeder, 1987). The effect of rotational mixing is more important in more massive stars (e.g. Heger et al., 2000). In principle, chemical gradients in the star prevent mixing. Chemical gradients in the envelope are for example created by core overshooting. The high radiation pressure for massive stars lowers this effect of the hindrance of mixing. For very effective mixing, the star will evolve homogeneously (Maeder, 1987), implying the whole envelope has the same chemical composition. Homogeneous evolution results in a lower radial expansion of the star during its evolution (e.g. de Mink et al., 2009).

This rotational mixing also changes the abundances of the elements in the envelope. The byproducts from nuclear fusion, which is amongst others the ^{14}N isotope, rise to the stellar surface and this effect is noticeable in their spectrum. Although many studies have tried to investigate the rotational-mixing efficiency (e.g. Hunter et al., 2008, 2009; Przybilla et al.,

2011; Martins et al., 2015; Grin et al., 2017; Abdul-Masih et al., 2019), their results remain inconclusive.

The metallicity of a star is the abundance of elements heavier than helium. These elements are also called metals by astronomers. Stars with lower metallicity have weaker winds than their counterparts with higher metallicity (Crowther and Hadfield, 2006; Mokiem et al., 2007). The reasoning behind this is explained in Section 3.3.

It was mentioned that WR stars are classified according to their strong stellar winds, which arise from massive stars having luminosities close to the Eddington luminosity. The winds of massive stars become stronger with increasing mass, but become weaker with decreasing metallicity. A higher initial mass is needed in lower-metallicity environments in order for a single massive star to appear as a WR star. Up until very recently, it was believed that the binary channel of the formation of WR stars would thus become more important in low-metallicity environments. Studies by Bartzakos et al. (2001); Foellmi et al. (2003a,b); Schnurr et al. (2008) showed however that the percentage of WR stars with companions in the low-metallicity environments of the Magellanic Clouds does not differ significantly from that of the Milky Way. This was in contradiction with theory. Shenar et al. (2020) suggest that the minimal initial mass for a star to appear as a WR star after stripping increases with decreasing metallicity. The minimal initial mass for a star to appear as WR stars from self-stripping, i.e. no companion is involved, is higher or equal to the previously stated mass. As such, stars stripped by a companion will only appear as a WR star when their initial mass was in between the two threshold masses. Shenar et al. (2020) then derive values for the threshold masses, showing why we should not necessarily expect a higher binary fraction amongst low-metallicity WR stars.

3 Basics of astronomy

This chapter aims to quantify some of the explained ideas by introducing some basic principles of astronomy that are necessary to understand the following Chapters. Section 3.1 discusses some fundamental stellar parameters, after which Sections 3.2, 3.3 and 3.4 go into more detail about stellar timescales, winds and atmospheres. This chapter ends with an explanation of some observational effects which should be accounted for in part II of this text.

3.1 Fundamental stellar parameters

Models of stellar evolution and model atmospheres are based on a set of fundamental parameters that describe the star. For each parameter the initial value, i.e. the value of the parameter at the birth of the star, is referred to with the subscript 'initial'. There are three fundamental parameters which determine the evolution of a (single) star: initial mass, metallicity and rotational velocity. In order to determine the evolutionary state of the star there are three other parameters which are important: current stellar mass, radius and luminosity. Listed below are fundamental stellar parameters for the star itself - as in how it will evolve - and for the observer - to determine the evolutionary state of the star.

(Initial) Stellar mass - $M_{\text{(initial)}}$

The initial stellar mass M_{initial} is the mass the star has at birth. It is one of the fundamental parameters that determines the evolution of the star. It will, together with the other fundamental parameters, determine where the star will start its life in the HRD. It also determines its further evolution, again with the other parameters. The mass M of a single star can change during the evolution due to winds.

The Sun currently has a mass of $M = 1.9891 \times 10^{30}$ kg $\equiv 1M_{\odot}$. A commonly used way to present the mass of a star is in units of solar mass, as could be seen in the previous Chapter.

Luminosity, stellar radius & effective temperature - L, R & $T_{\rm eff}$

The radius R of the star is here defined as the outermost layer where gravity counterbalances the internal pressure (hydrostatic equilibrium). The initial stellar radius increases with mass. During the evolution of the star, the radius changes - mostly growing until it has gone through all burning stages, after which it decreases rapidly as the star shrinks or collapses.

The Sun has a radius $R = 696\,340\,000$ m $\equiv 1R_{\odot}$. Also the radius of other stars is quite often described in solar units. A star with a radius two times that of the Sun has $R = 2R_{\odot}$.

The effective temperature $T_{\rm eff}$ of a star is a measure of the temperature at its surface. It is defined as the temperature of a black body that radiates with the same amount of total flux as the star. Wien's displacement law states that the black-body radiation curve for different temperatures will peak at different wavelengths. This wavelength is determined by

$$\lambda_{\rm max} = b/T, \tag{3.1}$$

with the constant $b = 2.89777 \times 10^7$ Å K. The cooler the star, the more the radiation of the star peaks towards red wavelengths. The hotter the star, the more the radiation peak moves to the blue side of the wavelength regime (and beyond). Hence the blue and red nomenclature of hot and cool stars.

The Sun has an effective temperature of $T_{\rm eff} = 5778$ K.

The luminosity L of a star is the total amount of electromagnetic energy emitted per unit of time. The radius, effective temperature and luminosity are related by the so-called Stefan-Boltzmann equation, which is a consequence of the definition of the effective temperature,

$$L = 4\pi R^2 \sigma T_{\rm eff}^4, \tag{3.2}$$

with the Stefan-Boltzmann constant $\sigma = 5.66956 \times 10^{-8}$ W m^{-2} K^{-4}.

The Sun has a luminosity $L = 3.828 \times 10^{26}$ W $\equiv 1L_{\odot}$. Also here, the solar luminosity $L_{\odot}$ is used as a unit. The luminosity can be obtained as follows

$$L/L_{\odot} = (R/R_{\odot})^2 (T_{\rm eff}/T_{\rm eff,\odot})^4. \tag{3.3}$$

This is why the HRD can also be seen as an indication of the radius of the star, as it is closely related to L and $T_{\rm eff}$. Measuring two of the parameters automatically leads to the determination of the third.

On the main sequence the mass-luminosity relation goes as (Eker et al., 2018)

$$L \sim M^{\eta} \quad \text{with} \quad \begin{cases} \eta \approx 5 & \text{for} \quad M < 0.5 M_{\odot} \\ \eta \approx 3.5 & \text{for} \quad 0.5 M_{\odot} < M < 10 M_{\odot} \\ \eta \approx 1 & \text{for} \quad M > 10 M_{\odot} \end{cases} \tag{3.4}$$

Surface gravity - $\log g$

The surface gravity of a star is determined by

$$g = \frac{GM}{R^2}, \tag{3.5}$$

with $G = 6.67408 \times 10^{-11} \mathrm{m^3 kg^{-1} s^{-2}}$ the gravitational constant. Instead of using g, astronomers often use $\log g$ to describe the surface gravity of the star. It is also an indication of the evolutionary state of the star. Main-sequence massive stars have $\log g \approx 4\,[\mathrm{cm\ s^{-2}}]$. Evolved stars will have a lower $\log g$ as they are puffed up due to their expansion during their evolution. Compact stars and objects will have a higher $\log g$.

Rotational velocity - v_{rot}

The rotational velocity v_{rot} is a function of the radius and the rotational period of the star

$$v_{\mathrm{rot}} = \frac{2\pi R}{P_{\mathrm{rot}}}. \tag{3.6}$$

It is also one of the fundamental parameters determining the further evolution of the star. As previously mentioned, high rotation rates induce mixing in the stellar interior. v_{rot} thus also plays an important role in the radial expansion during the evolution of a star, as indicated in Section 2.6. High rotation rates will also alter surface abundances as elements produced in the core may rise to the surface.

Absolute magnitude - M

The absolute magnitude M of a star is a measure of the flux or luminosity of the star on an inverse logarithmic scale. A brighter object will thus have a smaller magnitude. The flux received from an object decreases with the square of the distance d^2. The apparent magnitude m, which is the observed magnitude[1], of the star will thus be dependent on the distance of

[1]It was the Greek astronomer Hipparchus who established a numerical scale to describe the brightness of each star appearing in the sky. The brightest stars were assigned an apparent magnitude $m = 1$ and the dimmest stars visible to the naked eye are assigned $m = 6$. The difference between them corresponds to a factor of 100 in brightness.

the object. The two relate as follows

$$M = m - 5\log(d) + 5, \tag{3.7}$$

where d is the distance in parsec. The parsec or pc is a unit often used by astronomers to indicate the distance from an object (1 pc= $3.08567758 \times 10^{16}$ m). The absolute magnitude is often given in a specific wavelength band. For example the visual magnitude is indicated as M_V.

A measure of the magnitude taking into account all wavelengths is the bolometric magnitude $M_{\rm bol}$. It is calculated from the luminosity L of the star by

$$M_{\rm bol} - M_{\rm bol,\odot} = -2.5\log(L/L_\odot), \tag{3.8}$$

with $M_{\rm bol,\odot} = 4.74$ the bolometric magnitude of the Sun.

Metallicity - *Z*

The metallicity Z is a measure of the total mass fraction of elements in the star which are heavier than helium. These elements are also called the metals. Metallicities are typically expressed in units of solar metallicity ($Z_\odot$). The metallicity has an influence on the stellar structure and the strength of stellar winds, which are less powerful in environments with lower metallicity.

For a star with a given mass, the radius increases with increasing metallicity. The luminosity and effective temperature decrease with increasing metallicity.

Surface abundance

The surface abundance is used by astronomers to help determine processes that are happening below the stellar surface. Standard models predict certain surface abundances in environments with different metallicity. When the measured surface abundances in the spectrum (Section 3.4) are higher than is expected, this is an indication of the internal mixing processes that are going on. It is also an indication of which burning cycle the star is currently using as different elements are created in different burning cycles.

3.2 Stellar timescales

There are three fundamental timescales which are important for the evolution of a star (after Tauris and van den Heuvel, 2006).

Nuclear timescale - τ_n

The nuclear timescale τ_n determines how long the star can fuse elements in the core. The nuclear timescale is determined by the ratio of the energy available from nuclear energy E_n and the luminosity L. The energy available for fusion is dependent on the mass of the star. The nuclear timescale is then given by

$$\tau_n = \frac{E_n}{L} \sim \frac{M}{L}. \tag{3.9}$$

As it has been previously shown in Section 3.1, the luminosity increases steeply with mass such that the lifetime decreases with increasing mass.

Whilst fusing elements in the core, the star evolves on a nuclear timescale. Each fusing cycle has its own nuclear timescale. Since the burning of hydrogen releases the largest amount of energy, the nuclear timescale of hydrogen will last the longest. The hydrogen-burning timescale is often used as a measure for the total lifetime of the star.

For a star with $M = 1M_\odot$ $\tau_n \approx 10^9$ yr.

Kelvin-Helmholtz timescale - τ_{KH}

During some stages in the evolution of the star nuclear reactions will not be the main energy source. For example right after hydrogen exhaustion in the core. The energy for sustaining the luminosity of the star is then produced by the gravitational contraction of the star. The Kelvin-Helmholtz timescale τ_{KH}, also called the thermal timescale, is the time it takes the star to radiate away all of its current energy at the current luminosity. It is approximately given by

$$\tau_n = \frac{GM^2}{2RL}. \tag{3.10}$$

When nuclear reactions in the core come to an end, the star evolves on a thermal timescale.

For a star with $M = 1M_\odot$ $\tau_{\mathrm{KH}} \approx 10^7$ yr. Generally $\tau_n >> \tau_{\mathrm{KH}}$.

Dynamical timescale - τ_{dyn}

During most of its life, the star is in hydrostatic equilibrium, meaning that the pressure force is balanced out by all other active forces. When this equilibrium is perturbed, for example due to sudden mass loss or a comet falling into the star, the star restores its equilibrium on a dynamical (or hydrostatic) timescale. The dynamical timescale is given by

$$\tau_{\mathrm{dyn}} \approx \left(\frac{R^3}{GM}\right)^{1/2}. \tag{3.11}$$

For a star with $M = 1M_\odot$ $\tau_{\rm dyn} \approx 30$ minutes and is generally of the order of (tens of) minutes. It follows $\tau_n >> \tau_{HK} >> \tau_{\rm dyn}$. If a comet would fall into a star, the star would almost immediately restore its equilibrium.

3.3 Stellar winds

The effects of stellar winds on the evolution are explained in Section 2.4. During the main-sequence life of massive stars, their mass-loss rates $\dot{M}$ are of the order $\sim 10^{-8} - 10^{-6} M_\odot$/yr. Certain stages in massive star evolution are characterised by mass-loss rates that can even get as high as $10^{-5} - 10^{-4} M_\odot$/yr (WR and LBV stars respectively; Nugis and Lamers, 2000). It is clear that the winds of massive stars need to be correctly accounted for if we want to understand their evolution.

The stellar winds of massive stars are radiation-driven. This means that their winds are a result of the pressure exerted on the stellar material due to the absorption and emission of radiation. The radiation is what drives mass outflows from the stellar surface. The particles in the winds have a low velocity at the stellar surface but are accelerated outwards, reaching a terminal wind velocity v_∞ at large distances from the star. The terminal wind velocity v_∞ is also the maximum velocity achieved by the winds. In hot stars, these velocities can reach up to 3 000 km/s, which is 1% of the speed of light.

Every spectral line will contribute to the pressure exerted on the stellar material. In order to determine the velocity of the particles in the wind all spectral lines thus need to be taken into account. This requires the determination of a large number of ionisation and excitation stages of different elements. Atomic transitions and radiative transfer are discussed in more detail in Section 3.4.

Since the density of stellar winds is low, most of the elements will be found in the ground state of different ionisation levels. By good approximation, only resonance lines (i.e. transitions occuring between the ground state and upper states) need to be taken into account for the velocity calculations. The astronomers Castor, Abbott and Klein came up with the idea and introduced the theory called the CAK-theory (Castor et al., 1975). It is still used today.

Castor, Abbott and Klein started their calculations by assuming the star is a point source. They found in their approximation a formula for the wind velocity as a function of the distance from the star r:

$$v = v_\infty \left(1 - R/r\right)^\beta , \tag{3.12}$$

where $r > R$ with R the radius of the star and β a unitless parameter describing the steepness of the velocity field. This is also called the β-law

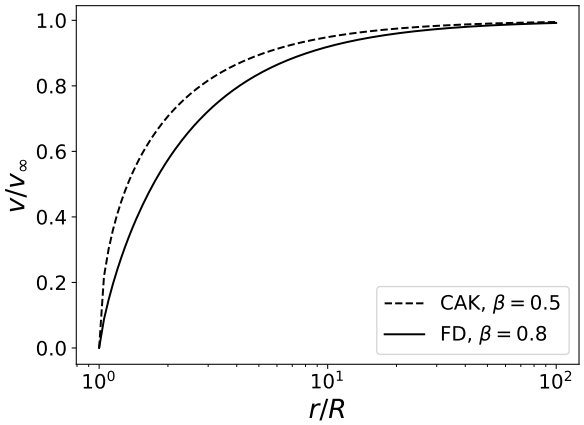

Figure 3.1: The β-law for FD ($\beta = 0.8$, solid line) and CAK ($\beta = 1/2$, dashed line). The y-axis shows the velocity of the wind divided by the terminal velocity. The x-axis shows the distance to the stellar surface on a logarithmic scale. Figure created for a wind with $v_\infty = 3\,000$ km/s.

for stellar winds. The CAK-theory predicts $\beta = 1/2$.

In practice, the star is not a point source. This approximation needs to be corrected for. The corrections are made by redoing the calculations whilst assuming that the star has a finite size. Friend and Abbott (1986) introduced a global correction factor, called the finite-disk correction or FD theory. The new value for β is 0.8, which gives a more gradual rise in velocity with radius. An image showing the difference in steepness between the CAK and FD model is shown in Figure 3.1 for a wind with a terminal velocity $v_\infty = 3\,000$ km/s. Only the basic assumptions and end results of the CAK-theory and FD model are discussed, as this thesis does not focus on winds. For further details and calculations, the reader is referred to the cited sources.

Whilst improvements on the wind-velocity law have been made (Krtička and Kubát, 2011; Sander et al., 2019), new problems such as clumping of material in the stellar wind arise (Puls et al., 2006; Oskinova et al., 2007; Sundqvist and Owocki, 2013, first visual detection by Eversberg et al., 1998). There are two types of clumping: optically thin and optically thick (Owocki et al., 2004). Recombination of electrons and ions occurs in optically thin winds, increasing the radiation pressure as lower ionisation stages of elements have more spectral lines. If the clumps are optically thick, radiation cannot pass through, while it travels more effectively through the inter-clump regions. Observationally, it has been shown that clumping in the winds would result in lower outflow rates than theoretically predicted (Bouret et al., 2003). Lower mass-loss rates could greatly alter our understanding of massive stars, as certain stages in their evolution (LBVs and WR stars) are characterised by extreme winds.

Metals have many more atomic transitions than hydrogen or helium. More metals in the envelope will result in stronger winds, as metals will feel more radiation pressure. This is why winds in low-metallicity environments are shown to be weaker (Crowther and Hadfield, 2006; Mokiem et al., 2007).

3.4 Stellar atmospheres

This section aims to cover the aspects of stellar atmospheres, relevant to this work. Starting with a brief introduction on the spectral energy distribution of the star, the different elements of a spectrum and the radiative transfer equation, Sections 3.4.1 and 3.4.2 explain the continuum and spectral line formation in the stellar atmosphere. Section 3.4.3 introduces how stellar atmospheres are modelled. Several mechanism broaden spectral lines (Section 3.4.4) and Section 3.4.5 illustrates the characteristic spectral lines for stellar winds.

Spectral energy distribution The spectral energy distribution (SED) of a star shows the energy emitted as a function of wavelength. It is the radiation coming from the stellar atmosphere. A celestial body in thermal equilibrium with its environment will emit radiation in a wide range of wavelengths according to Planck's law. The SED of a star has approximately the shape of a black-body radiation curve and it determines the effective temperature of the star (Section 3.1).

The SED can be constructed by measuring the total light intensity at each wavelength. In practice, the light intensity is measured in filters or (pass)bands, covering a certain (small) wavelength range.

For most photometric systems, which are a set of passbands, the measured light intensity can be calibrated against standard stars. These are stars for which the intensity and magnitude are known, such that the magnitude of the star in that passband is obtained.

For a wavelength $\lambda >> k_B T$ the energy distribution of a black-body can be approximated by

$$B_\lambda(T) = 2ck_BT/\lambda^4, \tag{3.13}$$

where $k_B = 5.66956 \times 10^{-8}$ W m^{-2}K^{-4} is the Boltzmann constant. This is the Rayleigh-Jeans tail. For massive stars the visual wavelengths can already be approximated with the Rayleigh-Jeans equation.

Spectrum The spectrum of a star provides a detailed look on the properties of the stellar radiation. It holds information on the elements which are present in the stellar atmosphere and how the different transition states of these elements are populated. The stellar atmosphere consists of many

particles. For hotter stars these particles will be ionised atoms and electrons whereas for very cool stars more molecules and atoms in the ground state will be present. The radiation produced by the nuclear reactions in the stellar core will interact with these particles. It is the radiation after interaction that we observe.

The radiative-transfer equation determines how the radiation coming from behind a certain stellar layer will interact with that layer or equivalently how the radiation coming from the inner stellar layers will react with the material in the photosphere. The radiative-transfer equation is

$$\frac{\mathrm{d}I_\nu}{\mathrm{d}\tau_\nu} = -I_\nu + S_\nu. \tag{3.14}$$

I_ν is the radiation coming from behind the inner stellar layers and S_ν is the source function or the radiation coming from the stellar photosphere itself. τ_ν is called the optical depth and is a measure of how much of the radiation coming from behind a certain stellar layer we can see. The radiative-transfer equation will have a different solution depending on the wavelength.

The black-body radiation forms the basis of the spectrum of the star and is called the spectral continuum. In addition to this continuum, several absorption and emission lines can be distinguished due to the presence of specific elements, which is determined by the radiative-transfer equation. The following sections (and also the introductory part) are based on the lecture notes of the course *Radiative processes in Astronomy*, taught at KULeuven (Prof. H. van Winckel).

3.4.1 Continuum

The continuum originates from *bound-free* (bf) transitions from atoms and ions and *free-free* (ff) transitions, also called *Bremsstrahlung*. The latter is electromagnetic radiation resulting from the acceleration or deceleration of a charged particle in a Coulomb field, for example due to a collision between an ion and an electron.

The part of the continuum that is created by bf-transitions is a result of the absorption of a photon with an energy equal to or higher than the ionisation energy of the electron in a bound state n. The emission of a photon occurs when a free electron is trapped by an ion into a bound state n. The energy of the electron in a bound state n is given by $\Delta\chi_{n0} = \chi_n - \chi_0$, where the energy level $n = 0$ is the ground state. We define $\chi_0 = 0$ and the energy of the level n as χ_n.

Free electrons can have an arbitrarily large amount of kinetic energy $mv^2/2$, where m is the mass of the electron and v is its velocity. The

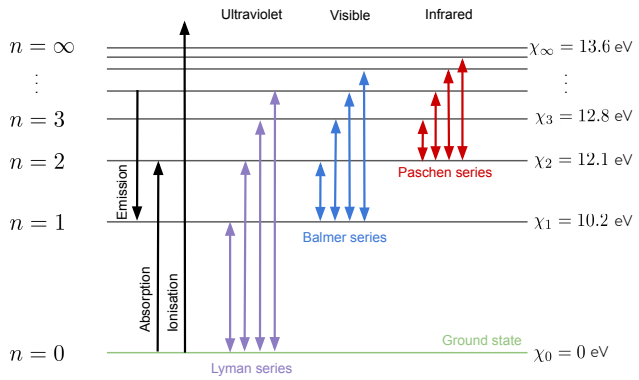

Figure 3.2: Energy levels of a hydrogen atom. Different energy levels and their energies are indicated. The energy scale is non-linear. Several transitions (not all) are shown for the first three series: Lyman, Balmer and Paschen series. At the top is indicated which series are visible in what wavelength domain.

energy of the photon associated with these bf-transitions is

$$h\nu = \chi_\infty - \chi_n + mv^2/2 = \Delta\chi_{\infty n} + mv^2/2, \tag{3.15}$$

with $h = 4.135667 \times 10^{-15}$eV s and χ_∞ is the energy necessary to ionise the atom in its ground state.

Figure 3.2 shows an example of the energy levels of a hydrogen atom. The ionisation of hydrogen in the ground state would require a photon with an energy $h\nu \geq 13.6$eV. The other way around, the trapping of an electron into the ground state will create a photon with an energy $h\nu \geq 13.6$eV.

3.4.2 Spectral lines

The spectral lines can be in emission or absorption relative to the continuum. An absorption line is the result of absorbed photons of a specific wavelength from the light beam in contrast to photons of other slightly different wavelengths (the continuum). An emission line occurs when more photons of a specific wavelength are created than photons of other slightly different wavelengths. An example of an emission and absorption line is given in Figure 3.3.

Spectral lines are a result of discrete *bound-bound* (bb) transitions, where the electron jumps from one bound state to another bound state, i.e. between energy levels $n < \infty$. Excitation, a jump to a higher energy level, can be caused by the absorption of kinetic energy (collisional excitation) or by the absorption of a photon (radiative excitation). Analogously, de-excitation, a jump to a lower level, can be caused by a collision (collisional de-excitation) or by the emission of a photon (radiative de-excitation). The

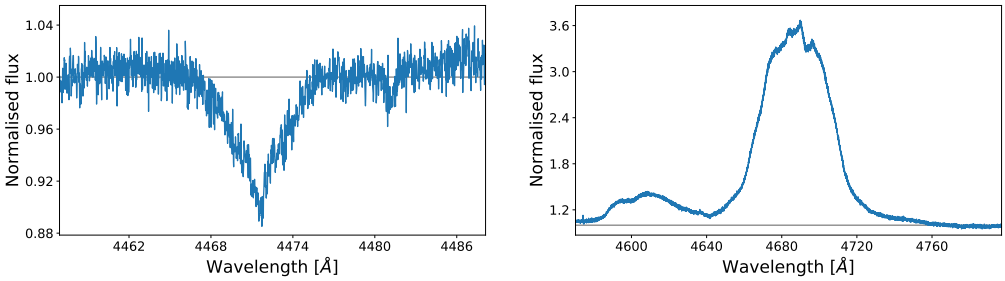

Figure 3.3: An example of an absorption line (left) and an emission line (right) in one of the spectra of BAT99 126.

energy of the photon associated with a radiative jump is given by

$$h\nu = \chi_m - \chi_n = \Delta\chi_{mn}. \tag{3.16}$$

For the hydrogen atom (Figure 3.2) these transitions are divided into series depending on which energy level is involved in the transition. All transitions from and to the ground state $n = 0$ are part of the Lyman series (purple). The transitions from and to the first excited state $n = 1$ form the Balmer series (blue). Likewise the Paschen series (red) are the transitions involving the second excited state. These series are shown in the Figure. The transitions of the Balmer series are indicated with a Greek letter to indicate the levels involved. For example, the spectral lines corresponding to the Balmer series indicated in Figure 3.2 (which are not all) from left to right are : Hα, Hβ, Hγ, Hδ.

Terminology Spectral lines are noted down as the abbreviation of the element followed by a Roman number indicating the ionisation level. Here, the Roman number 'I' stands for non-ionised stage of the element, 'II' stands for single ionised and so on. For example an O I transition corresponds to an atomic transition of non-ionised oxygen and an O II transition to an atomic transition of single-ionised oxygen. Moreover, the rest wavelength of the spectral line is also noted down. The notation of the atomic transition of single-ionised oxygen, with a rest wavelength of 4169.22 Å is written as 'O II λ4169.22'.

3.4.3 Model atmospheres

The presence of a spectral line associated with a certain atomic transition is determined by the abundance of the elements in that state or the level population. For example if very little He II is present the spectral lines corresponding to the atomic transitions of He II will be very weak or not present at all. It is the presence or absence of spectral lines corresponding

to certain elements/atomic transitions in the spectrum that determine the spectral type of the star.

During most of the lifetime of a star, the spectral lines originate from their photosphere (the gas surface above R) and are in absorption relative to the continuum.

In order to gain insight into the spectral classification (see Section 2.1), the stellar photosphere is approximated by local thermal equilibrium (LTE). This approximation implies that

- the relative populations of the various atomic levels of particles in the volume is in equilibrium (chemical equilibrium), and
- at each point the pressure force is compensated by all other forces (mechanical/hydrostatic equilibrium), combined with a single temperature in that volume (thermal equilibrium).

Chemical and thermal equilibrium combined give thermodynamic equilibrium. The star as a whole is not in thermal equilibrium, for example the core is extremely hot and dense and the outermost stellar layer is cool. The assumption of a single temperature throughout the star can most certainly not be made. However, locally, in a very thin layer, the temperature is uniform and the conditions of thermal equilibrium are met. Hence, thermal equilibrium is applied locally resulting in the assumption of LTE.

In LTE the relative populations of different atomic levels are solely determined by the thermodynamic quantities: the temperature and the electron pressure. There are two equations that determine the relative populations: the excitation law of Boltzman and the ionisation law of Saha.

Excitation law of Boltzmann

The distribution of excitation states within the same ionisation state is described by the Boltzmann relation

$$\frac{n_{r,s}}{n_{r,t}} \propto e^{-(\chi_{r,s}-\chi_{r,t})/k_B T}, \tag{3.17}$$

where $n_{r,s}, n_{r,t}$ are the number densities in excitation levels s, t of ionisation state r and $\chi_{r,s}, \chi_{r,t}$ are their related energies.

Ionisation law of Saha

The ratio of the number density of two successive ionisation states in the ground state is given by the Saha relation

$$\frac{n_{r+1,0}}{n_{r,0}} \propto \frac{1}{N_e}(k_B T)^{3/2} e^{-(\chi_{\infty r,0})/k_B T}, \tag{3.18}$$

where N_e is the electron number density and $\chi_{\infty r,0}$ is the ionisation energy of the ground state of ionisation state r.

LTE can be assumed when collisions dominate the pressure force. This condition is surely met in the dense interior of stars. However, in the atmosphere of stars the density is much lower and radiative processes become important. The Boltzmann and Saha equations do not determine the relative populations of different atomic levels anymore, as the radiation field becomes important as well. Hence the conditions are those of non-thermodynamic equilibrium (non-LTE).

Generally, statistical equilibrium is assumed to compute the level populations. This means that there is no net change in the abundances of the level populations. The equation that is solved is the following:

$$\frac{\mathrm{d}n_i}{\mathrm{d}t} = \sum_{j \neq i}^{N} n_j P_{ji} - n_i \sum_{j \neq i}^{N} P_{ij} = 0, \tag{3.19}$$

where n_i is the population in level i, N is the total number of atomic levels that can influence n_i. P_{ji} is the probability that a transition from level j to i occurs. The equation states that all processes that lead to the population of the state i are in balance with the reactions that depopulate the level. This does not imply that all microscopic processes need to be in balance, but the net level population does not change.

In non-LTE conditions, these equations are also coupled to each other and to the radiation field. The radiation field in turn depends on the populations. Solving the equations for non-LTE conditions is a complex problem. All equations need to be simultaneously solved with the equation of radiative transfer.

State-of-the-art non-LTE model atmosphere codes which solve all the equations simultaneously have been developed. Examples of such codes are CMFGEN (Hillier and Miller, 1998), FASTWIND (Puls et al., 2005), TLUSTY (Lanz and Hubeny, 2003) and the Potsdam Wolf-Rayet model atmosphere code (PoWR) (Hamann and Gräfener, 2003). In this thesis, both PoWR and TLUSTY are used.

There are two major differences between the two codes. One of them is in how the two codes solve the radiative-transfer equations. TLUSTY solves the radiative-transfer equation for a plane-parallel surface. PoWR uses the spherical solution, which allows for winds. Hence PoWR is used to model WR stars and TLUSTY is used to model B-type stars and also late O-type stars. A second difference is that TLUSTY has a more extensive spectral line list.

3.4.4 Broadening of spectral lines

The following Sections are considered for radiative de-excitations, i.e. atomic transitions which emit photons, but the explanations are also valid for ab-

sorption of photons.

In ideal circumstances, the transition from one atomic level to another will always emit a photon with the same wavelength. The transition should thus be observed in the spectrum as a sudden peak with no width. In practice however there will not only be photons of one single wavelength emitted in the atomic transition but photons with slightly different wavelengths will be emitted as well. Hence the transition will not be observed as a sudden peak but will rather have a certain line profile. This is called broadening of the spectral line.

The broadening mechanisms in stars are illustrated here.

Natural broadening

The lifetime of an atomic level is the average time an electron will stay on that atomic level before it falls back to a lower energy level (de-excitation). De-excitations to different levels have different lifetimes. For most of the atomic transitions these lifetimes are known. The uncertainty principle of Heisenberg states the following

$$\Delta E = h/(2\pi\Delta t), \tag{3.20}$$

where Δt is the known lifetime of the transition. The energy of the photon is related to the energy difference between the two levels. Hence the photons emitted will have slightly different wavelengths. The broadening related to this effect is called the natural broadening of the line.

Pressure broadening

When two atoms approach each other, their energy levels will change due to the interaction between the two atoms. The energy difference $\Delta\chi_{mn}$ between the levels m and n changes accordingly. If the interaction between the two atoms is repulsive, the change in $\Delta\chi_{mn}$ is positive. If the interaction is attractive, the change in $\Delta\chi_{mn}$ is negative. A transition happening in an interacting atom will thus have a different photon energy than a non-interacting atom. These interactions are also called collisions. Pressure broadening is thus also referred to as collisional broadening.

In the low-density atmospheres of red giants and supergiants this broadening effect is very weak. However, for main-sequence stars the spectral lines will be subject to pressure broadening.

(Microscopic) Doppler broadening

Doppler broadening is related to the thermal motion of atoms. The atoms have a spread in velocity with respect to the rest frame of the observer.

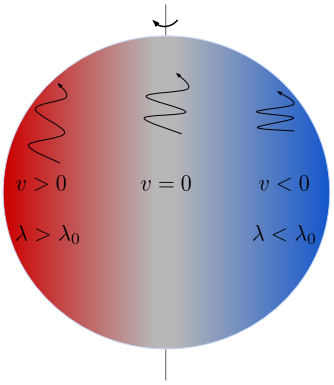

Figure 3.4: Schematic representation of a rotating star. The color gradient indicates how the wavelength of the photons changes from the rotation.

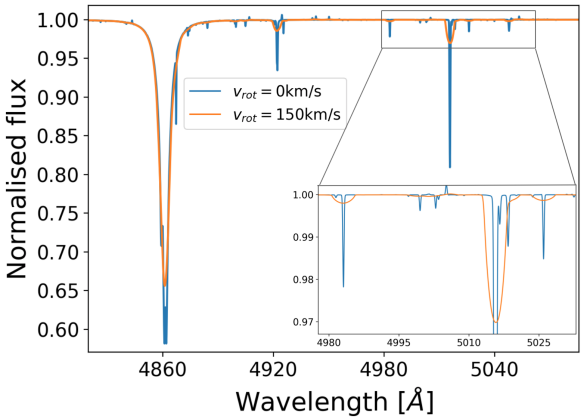

Figure 3.5: Part of a spectrum from a TLUSTY model star with $T_{\text{eff}} = 40$ kK and $\log g = 4$ [cm s^{-2}]. The blue spectrum has no rotational broadening. In the orange spectrum the star rotates with $v_{\text{rot}} = 150$ km/s.

The wavelength of the photons emitted from atoms with a velocity v will shift according to the non-relativisic Doppler law:

$$\lambda = \lambda_0 \left(\frac{v}{c} + 1 \right), \tag{3.21}$$

where λ_0 is the rest wavelength of the atomic transition (in vacuum) and $c = 299\,792\,458$ m/s is the speed of light.

Rotational broadening

The aforementioned broadening mechanisms are all important on a microscopic level. Rotational broadening is important on a macroscopic scale. As the star rotates with a particular velocity v_{rot}, particles at different positions in the stellar atmosphere will move with different velocities v. The photon emitted from de-excitation of a certain atom will be shifted according to Doppler's law presented in Eq. (3.21). A schematic representation is shown in Figure 3.4. As the star rotates, the photons emitted in the part of the star that is moving towards the observer (here the right side) will have shorter wavelengths and hence will be blue shifted. The photons coming from the part that is moving away from the observer (here the left side) will have longer wavelengths and will be red shifted. An example of a spectral line that is affected by rotational broadening is shown in Figure 3.5. It can be seen that for fast-rotating stars certain spectral lines will become very broad. Spectral lines can get become so broadened that it becomes difficult to distinguish the continuum from the spectral lines.

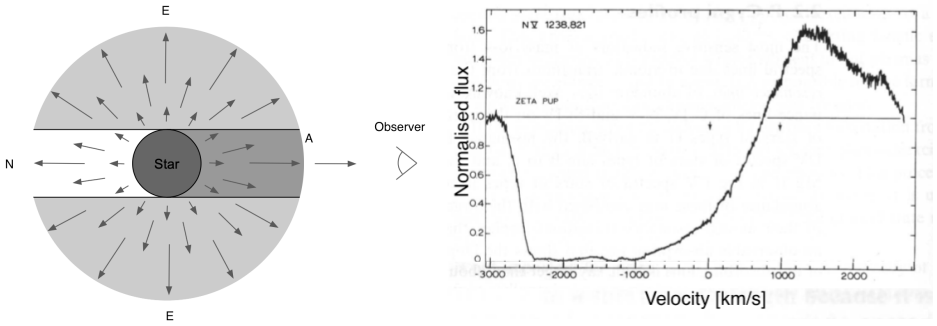

Figure 3.6: Left: Schematic representation of radiation moving through stellar winds. The observer discriminates between three regions in the winds: N, E and A. The explanation is in the text. Right: A P-Cygni profile in the N v doublet in the UV spectrum of the massive stars ζ Pup (O4 supergiant). Figure taken from the lecture notes of Prof. C. Aerts, p187.

3.4.5 Spectral lines in winds

There are two characteristic spectral lines in winds: the P-cygni profile and pure emission lines.

P-Cygni profile A P-Cygni profile is a spectral feature which shows blue-shifted absorption combined with red-shifted emission. The light of the star containing a photospheric spectral line passes through the stellar winds. The photons interact with the material in the wind and scatter. A schematic representation of the winds is given in the left panel of Figure 3.6. Radiation coming from region N will never reach the observer as this region is hidden behind the star.

The material in region A is moving towards the observer with a velocity 0 km/s $< v < v_\infty$. Some of the photons that are scattered in region A will leave the line-of-sight. These photons would reach the observer in the absence of winds. The results is blue-shifted absorption with a Doppler shift between $-v_\infty$ and 0 km/s.

The material in the surrounding halo E has $-v_\infty < v < v_\infty$. The photons passing through region E are scattered in all directions. Some of the photons will hence scatter in the direction of the observer. This induces an emission part with Doppler shifts between $-v_\infty$ and v_∞. The biggest contribution will be centred around 0 km/s. An example of a P-Cygni profile in the spectrum of the star ζ Pup is given in the left panel of Figure 3.6.

Pure emission Pure-emission profiles arise in winds where transitions are optically thin. The winds of WR stars are an example. Their winds are

optically thin in visual wavelengths, meaning that the absorption part created in a P-Cygni profile is negligible and hence only emission is obtained[2]. The emission line will be seen over wavelengths with Doppler shifts between $-v_\infty$ and v_∞ and is centred around $v = 0$ km/s.

3.5 Observational effects

In this section, some observational effects are explained, that need to be taken into account whilst analysing data used in this thesis (Chapter 6). Section 3.5.1 discusses interstellar reddening. Limb darkening and gravity darkening are explained in Sections 3.5.2 and 3.5.3 respectively.

3.5.1 Interstellar reddening

The light of stars travels through the interstellar medium before reaching our telescopes. The interstellar medium is defined as the material that exists between stars. It consists of gas and dust particles. The typical dust grain size in the interstellar medium is of the size of the wavelength of photons in the visible spectrum. As the radiation coming from a star passes through the interstellar medium, gas and dust particles will scatter the radiation along the line-of sight. The typical dust grain size makes ultraviolet and visible radiation much more sensitive to dust scattering than infrared radiation. Fewer 'blue' photons coming from the star will thus reach the telescope. Red photons on the other hand are much less prone to this scattering. Hence the star will appear redder than it actually is. This phenomenon is referred to as *interstellar reddening*.

This interstellar reddening needs to be accounted for when analysing data. Especially when using photometric data, not taking this into account would result in wrong magnitudes and fluxes. The way we account for the interstellar reddening is presented in Appendix A.

3.5.2 Limb darkening

Not all the light that reaches the telescopes originates from the same stellar layer. When looking at an image of the Sun, it can be seen that its edges are darker than the centre. This effect is called *limb darkening*. It affects all stars.

The radiation that reaches the telescopes originates from a certain depth within the stellar object. A light ray can only travel a certain distance before it interacts with the stellar material. The radiation coming from the

[2]P-Cygni profiles in WR spectra are more observed in ultra-violet wavelengths as the winds are less optically thin towards these photons.

edges of the star originates from higher and cooler layers than the radiation in the centre and this causes the darkening of the edges.

The limb darkening is a function of the angle of the outgoing radiation and the stellar surface (γ), defined as $\mu \equiv \cos\gamma$. For stars like the Sun, with low effective temperatures, the best law describing the limb darkening is a linear function of μ. This is called the *linear-cosine law*. (Diaz-Cordoves et al., 1995)

For stars with $T_{\text{eff}} > 8\ 500$ K, it has been shown that a function which goes as the square root of the angle $\sqrt{\mu}$ best describes limb darkening (Diaz-Cordoves and Gimenez, 1992). This law is called the *square-root law*. It follows that limb darkening for massive stars on the main sequence is best described by this square-root law.

Limb darkening affects the light curves of eclipsing binaries. Since the outgoing radiation of stars is not uniformly spread over the surface, the amount of light that is blocked during the eclipse does not depend only on whether one of the stars is fully eclipsed. As the eclipsing star moves in front of the other star, it first passes over the limbs and hence less light is blocked than when it is positioned at the centre. This will affect the shape of the bottom of the eclipse.

3.5.3 Gravity darkening

Gravity darkening is the effect of the distortion of the shape of the star caused by the gravitational attraction of the close-by companion. It also affects very rapid rotators. In both cases, the star will appear as an oblate spheroid. The poles, which are now compressed, are denser and hence will have a higher temperature than the less dense equator. The result is that the equator of the star is darkened and the poles are brightened. Therefore, gravity darkening is also referred to as gravity brightening. A more theoretical description is given in White et al. (2012)

4 Binary systems

A binary system is a system of two stars which are gravitationally bound to each other. Several studies (e.g. Chini et al., 2012; Sana et al., 2012, 2014; Aldoretta et al., 2015) have shown that more than 70% of all massive stars are part of a binary or higher-order multiple system and it is predicted that most of massive stars will interact with a companion during their evolution (Sana et al., 2013).

Close binaries are binaries for which the distance between the two components is comparable with or slightly larger than the dimensions of the two components on the main sequence. The components in close binaries are limited in their expansion due to the presence of the other star. As explained in Chapter 2, single stars will experience a large radial expansion during their evolution as they become (super)giants. With a companion in the close vicinity of the evolving star, its evolution will be drastically altered by the presence of the other star.

The following Sections are based on Tauris and van den Heuvel (2006), Prof. O. Pols' lecture notes and the lecture notes of the course *Binary stars*, taught biannually at the KULeuven (last taught academic year 2019-2020, Prof. H. Sana). The first three Sections apply to binaries in general, whereas the other Sections are specifically for close/interacting binaries.

4.1 Parameters of a binary system

There is a distinction between parameters intrinsic or fundamental to the system and parameters related to the orientation of the binary system. The latter will change the observer's perception of the orbit, but it will not affect the evolution of the system.

4.1.1 Fundamental parameters

The fundamental parameters determine the further evolution of the binary, assuming that no extra-binary components influence the system. These parameters are:

Orbital period and semi-major axis - P and a The orbital period P of a binary system is the time it takes for the star to fully revolve around the centre of mass once. The semi-major axis of the system is half of the distance between the periastron and apastron. The periastron is the point of closest approach between the components. The apastron is the point of farthest approach.
The period and the semi-major axis are related by Kepler's third law

$$P^2 = \frac{4\pi^2 a^3}{GM}, \tag{4.1}$$

with $M = M_1 + M_2$ the total mass of the system. M_1 and M_2 are the masses of the individual components.

Orbital eccentricity - e The orbital eccentricity e is the degree of ellipticity of the system. It defines the ratio of the semi-major axis a and the semi-minor axis b as $b/a = \sqrt{1-e^2}$. An orbit with $e = 0$ corresponds to a circular orbit.

Mass ratio - q The ratio between the masses of the two components is defined as $q \equiv M_2/M_1$. By definition $q \leq 1$.

Terminology The binary nomenclature used in this thesis is the following. The most massive component in a binary system is called the primary (subscript '1') and the less massive star is called the secondary (subscript '2'). This refers to how the system is observed. If initially the primary was less massive, it will still be referred to as the primary since it is observed as the more massive star (see Section 4.4).

4.1.2 Orientation parameters

The orbit of a star is defined against a reference plane. This is the plane in which we observe and is the plane normal to the line of sight. The orientation parameters are shown in Figure 4.1. The reference plane is the grey plane and the orbit of the binary is the yellow plane. The reference direction against which certain parameters are calculated is also indicated. The following parameters determine how an observer perceives the orbit:

Time of periastron passage - T0 A point in time where the star is located at the periastron of its orbit or thus the point where it is located closest to the other component. In this thesis it is also referred to as HJD0, which is T0 given in Heliocentric Julian Date (HJD), which is a way astronomers measure the time with the barycentre of the solar system as a reference.

Longitude of the ascending node - Ω The ascending node is the point where the orbit crosses the reference plane whilst the star is ascending. The longitude of the ascending node is the angle between the reference direction and the ascending node. Also used for calculating other orbital elements.

Orbital inclination - i The angle between the orbital plane and the reference plane. An orbital inclination of $i = 90°$ means the orbit is fully located in the reference plane and the orbit has no nodes. For $i = 0°$ the orbital plane is perpendicular to the reference plane. (Note that for the stellar inclination it is the other way around).

Argument of periastron - ω The angle between the ascending node and the periastron, the point of closest approach. In Figure 4.1 the periastron is indicated with the name periapsis, which is the general name for the point of closest approach.

True anomaly - ν The position of a star will change over time as it moves along the orbit. The parameter indicating the position of the star is the true anomaly ν and is defined as the angle between the periastron and the position of the star with respect to the central point of the line of intersection between the orbital plane and the reference plane.

4.2 Types of binaries

Binaries are detected by observing some kind of movement of the components. They are classified into different groups according to the method used to detect this motion. BAT99 126 is detected as a multiple system according to two methods: spectroscopy and photometry.

4.2.1 Spectroscopic binaries

Spectroscopic binaries are detected by measuring a periodic Doppler shift (Eq. 3.21) of the individual components in the spectrum. This Doppler

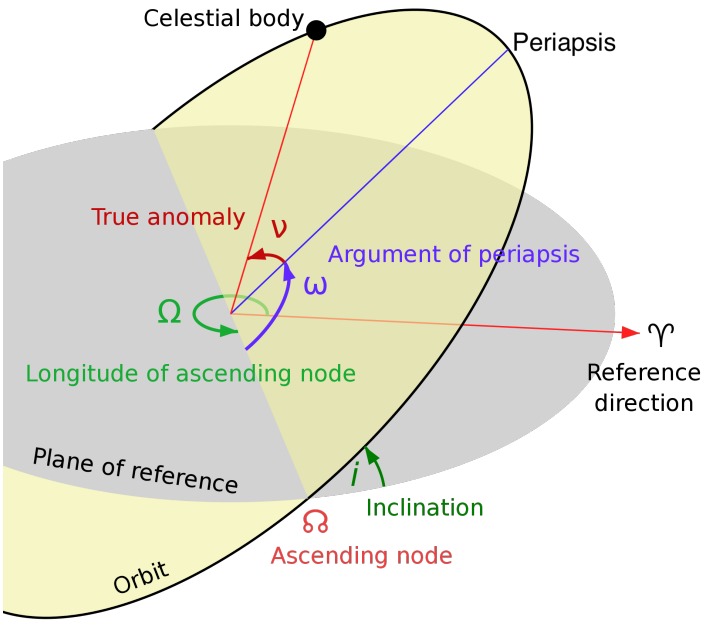

Figure 4.1: Parameters in the orbit of a binary system. Figure credits to Lasunncty via Wikimedia Commons

shift is the result of the radial velocity in the line of sight of the components. The individual components of spectroscopic binaries are unresolved. This can be due to the system being too distant from Earth, their orbital separation being too small or a combination thereof. An apparent single star is seen through telescopes but the spectrum can reveal its true nature.

Spectroscopic binaries can be divided into groups depending on the numbers of observed stars which belong to the system. In a single-lined spectroscopic binary (SB1) the spectral lines which are visible in the spectrum belong to only one of the components. The binarity of the star is inferred through the Doppler shift in the spectral lines of the visible component. An example of when only one star would be visible in the spectrum is when the component of the star has a very low mass compared to the visible star, or when the component is a compact object.

In SB2 systems both the primary and secondary star are visible in the spectrum. Their spectral lines exhibit an anti-phase motion where the components are alternatively blue- and red-shifted. An illustration of how the spectral lines shift with the binary orbit is shown in Figure 4.2.

4.2.2 Photometric binaries

Photometric binaries are detected by observing transits of the two components. As one of the binary components moves in front of the other component, i.e. eclipses it, the brightness of the system will drop, as part

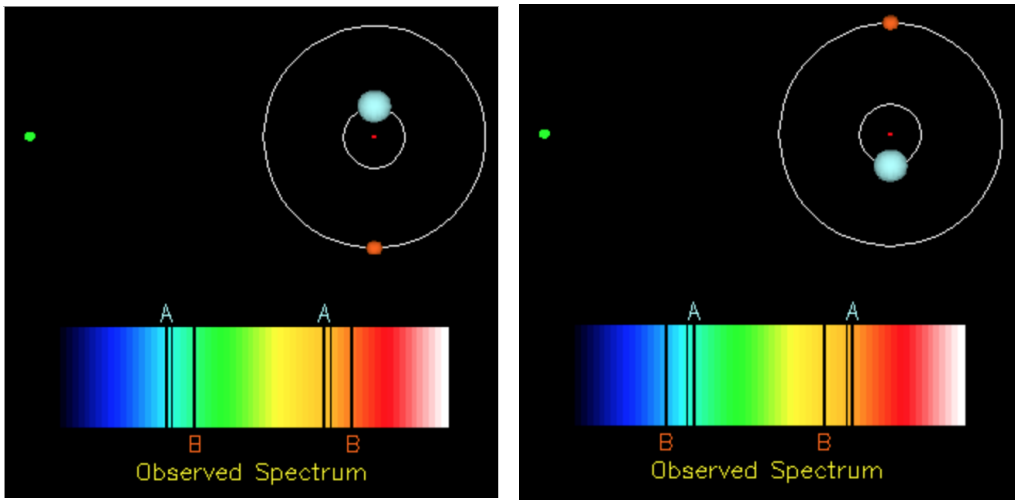

Figure 4.2: Visualisation of the Doppler shift observed in the spectral lines of binaries. The green dot on the left is the position of the observer. The larger blue component is component A and is the primary star. The smaller red component is component B and is the secondary star. The absorption lines from the two components in the spectra below are marked and color-coded accordingly. In the left panel component A is moving towards the observer and component B is moving away from the observer. In the right panel it is the other way around. Animation obtained with permission of Prof. Richard Pogge (`http://www.astronomy.ohio-state.edu/~pogge/Ast162/Movies/spanim.gif`).

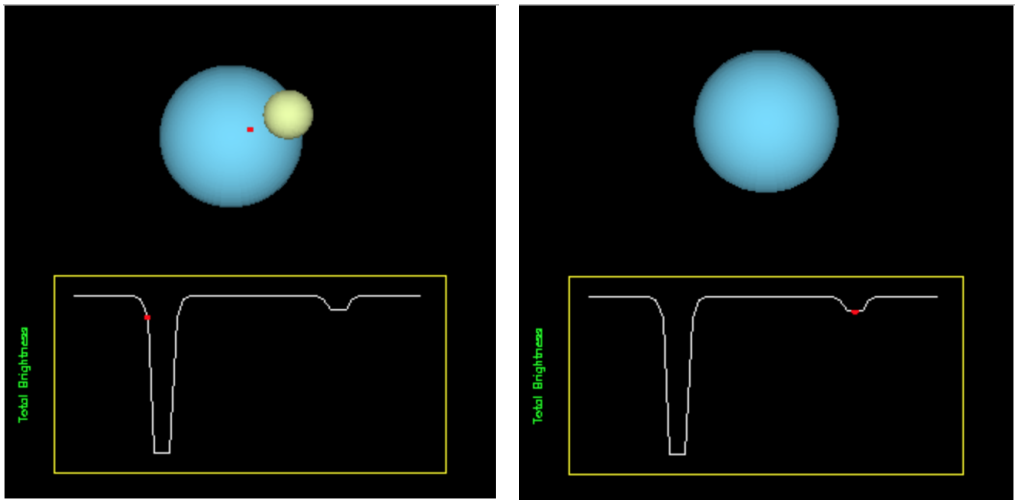

Figure 4.3: Visualisation of an eclipsing binary system. The corresponding part in the light curve is marked with a red dot. The larger blue component is the primary. The smaller yellow component is the secondary star. The left panel shows the onset of the first eclipse as the secondary moves in front of the primary. In the right panel the primary fully eclipses the secondary. Animation obtained with permission of Prof. Richard Pogge (`http://www.astronomy.ohio-state.edu/~pogge/Ast162/Movies/eclbin.gif`).

of the light of the second component will be blocked. By observing the system for a longer period of time, a light curve is obtained. A binary system is detected from a periodic signal of eclipses in the light curve. An illustration of an eclipsing binary is shown in Figure 4.3.

Terminology The primary eclipse, which is the deepest, is caused by the secondary star moving in front of the primary star. The secondary eclipse is then caused by the primary star eclipsing the secondary star. (Hilditch, 2001)

4.3 Determining the parameters

A full analysis of a binary system requires the determination of the binary orbit or the orbital equations of each star. These orbital equations describe Keplerian orbits.

The parameters P, e, ω and T0 can be determined from the analysis of spectroscopic data. Two additional parameters are derived from spectroscopy:

- **Radial-velocity semi-amplitude - K** Half of the difference between the maximum and minimum radial velocity of an individual star.
- **Centre-of-mass velocity - γ** The radial velocity of the centre of mass of the system.

The equation determining the variation of the radial velocity or the radial-velocity curve is given by

$$v_{\text{rad}} = \gamma + K\left[e\cos\omega + \cos(\omega + \nu)\right], \tag{4.2}$$

where K is related to other parameters by

$$K = \frac{2\pi a \sin i}{P\sqrt{1-e^2}}. \tag{4.3}$$

An illustration of the effect of e and ω on the radial-velocity curve is shown in Figure 4.4. It can be seen that for a circular orbit the radial-velocity curve is a sinusoid and the effect of ω can be interpreted as a horizontal shift. For a circular orbit, ω is usually defined to have a value of 90°.[1]

In total, spectroscopic data gives information about P, e, ω, T0 and K. Although K is related to a and i, it is K which is derived from spectroscopic

[1]There is a nice online tool which allows the user to vary the masses and eccentricity and see the radial velocity curve. It can be found at: `http://www.astro.ucla.edu/undergrad/astro3/orbits.html`

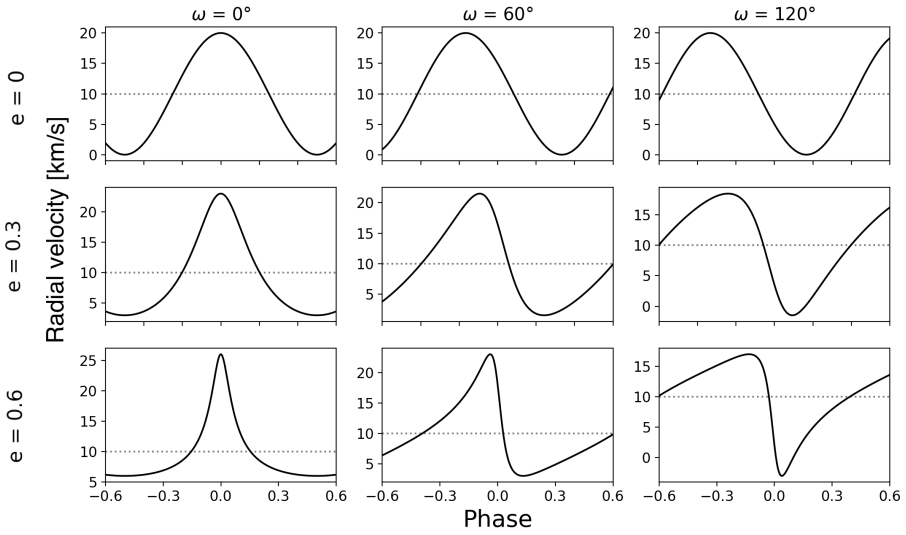

Figure 4.4: Radial-velocity curves with varying eccentricity and argument of periastron. Curves created for $P = 25$ days, $K = 10$ km/s and $\gamma = 10$ km/s.

data. In order to determine i other data is required, for example a light curve. When $i \approx 90°$ the eclipses will be flat-bottomed. Figure 4.3 is an example of a binary system with a flat-bottomed light curve. This arises when one star eclipses the other for a prolonged time. In this case, the same amount of flux is blocked for a longer period of time and hence the flat bottom of the eclipse. This is only possible for $i \approx 90°$. When i is too small no eclipses will be visible. Fitting tools are available which fit both the radial velocities and the light curve at the same time. An example is PHOEBE (Prsa and Harmanec, 2010), which is used in this thesis.

The equations mentioned above are for the parameters of the relative orbit. The relative orbit is the orbit of one star relative to the other and is shown as the bottom (grey) orbit in Figure 4.5. It is also possible to describe the equations for the barycentric orbits. These orbits describe the orbit of the stars around the centre of mass. In Figure 4.5 these orbits are shown in red and blue at the top. Here the variables belonging to the first and second component have subscripts '1' and '2' respectively. The following relations are valid for the the relative and barycentric orbits:

$$a = a_1 + a_2, \qquad e = e_1 = e_2, \qquad M = m_1 + m_2 \tag{4.4}$$

The velocity semi-amplitudes for both components can hence be written as

$$K_{1,2} = \frac{2\pi a_{1,2} \sin i}{P\sqrt{1 - e^2}}. \tag{4.5}$$

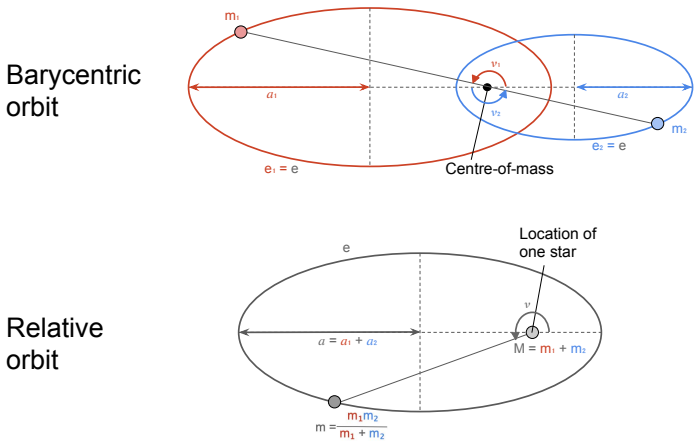

Figure 4.5: Relative orbit (grey, bottom) and barycentric orbits (red and blue, top) for a binary system.

The mass ratio is obtained by combining $K_{1,2}$ with Newton's second law of motion. This gives

$$q = \frac{m_2}{m_1} = \frac{K_1}{K_2} = \frac{a_1}{a_2}. \tag{4.6}$$

For SB2 systems both K_1 and K_2 are known. Combining Kepler's third law (Eq. 4.1) and the Equations (4.5) and (4.4), the minimum masses can be obtained:

$$m_{1,2} \sin^3 i = P(1-e^2)^{3/2}(K_1 + K_2)^2 K_{2,1}/(2\pi G) < m_{1,2}. \tag{4.7}$$

Determining either i for Equation (4.7) or the barycentric semi-major axis a for Kepler's third law yields the absolute masses of the two components:

$$m_1 = \frac{4\pi^2}{G}\frac{a^3}{P^2(1+q)} \qquad \text{and} \qquad m_2 = \frac{4\pi^2}{G}\frac{a^3}{P^2(1+1/q)}. \tag{4.8}$$

Instead of plotting the radial-velocity curve as a function of ν the phase ϕ is commonly used. At a certain time, ϕ is given by

$$\phi = (t - T0)/P - \text{floor}((t-T)/P), \tag{4.9}$$

where the second part on the right-hand side refers to the rounded down result of the division. It is used to phase-fold the data, which is equivalent to positioning all data points as if they were taken in the same orbit. Figure 4.4 is plotted as a function of the phase.

4.4 Close-binary interactions

In the 1940's, binaries were observed where the most massive component appeared to be a main-sequence star and the less massive component showed clear signs of being more evolved, for example of being a giant. Binaries of this kind are called Algol systems or Algols, after the prototypical binary that bears this name. The observation that the more massive star appears to be less evolved is in contrast with single star evolution theory (Chapter 2), as the more massive component should evolve faster. This is known as the *Algol paradox* (Kuiper, 1941). It became clear that binary interactions, and more precisely mass transfer, are necessary to explain this type of binary. The paradox is explained as follows: the initially more massive star, which is now the less massive evolved star, already lost a considerable amount of mass. The mass lost from the initially more massive star is captured by the initially less massive star, which will now become the more massive star. Algol-type binaries show that mass transfer can occur between the two components.

In the initial binary, with the more massive star or primary evolving faster than the initially less massive star or secondary, the two components are not interacting. The gravitational field of the binary, which depends on the masses of the two components and their motion, determines whether or not the two components will interact with each other. A schematic version of the gravitational potential is given in Figure 4.6 in 3D and 2D (left) and for a slice along the x-axis (right). In the left panel, the droplet-like shapes inside the inner solid eight-figure are the Roche lobes of the two components. Matter inside the Roche lobe is attracted by the respective component inside the Roche lobe. The first Lagrangian point L_1, the crossing point of the solid eight, is the point where matter is attracted by both the primary and secondary component. Matter behind the second and third Lagrangian point L_2 and L_3 is lost from the binary system. L_1 is the lowest point in the potential and mass loss will first happen through L_1.

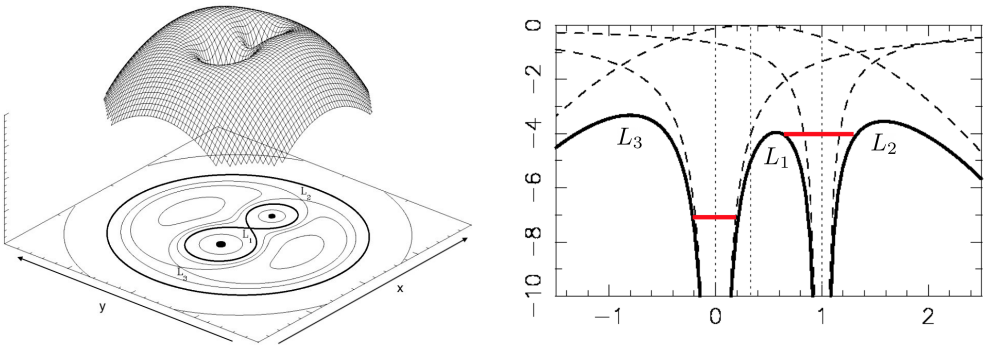

Figure 4.6: The Roche-lobe potential. Left: In 3D and 2D. Figure credits to Marc van der Sluys. Right: A slice along the x-axis. The red lines indicate the position of the stars in the potential. A bar at the height of the first Lagrangian point means the star is filling its Roche lobe.

Credits to Keith Horne. The first, second and third Lagrangian points L_1, L_2 and L_3 are indicated in both panels.

Initially, the two binary components reside within their Roche lobe. As the binary evolves, it is possible that the primary will start to fill its Roche lobe. This can be either due to the radial expansion of the primary as it evolves or due to the shrinkage of the orbit, caused by angular momentum loss. When the primary expands beyond its Roche lobe, Roche-lobe overflow (RLOF) is initiated and mass flows through L_1 towards the secondary. In the right panel of Figure 4.6 the red bars indicate the position of the stars in the gravitational potential, RLOF would be indicated by one of the red bars at a height slightly above L_1. Binaries which are observed in the process of mass transfer are called *semi-detached binaries*.

Terminology The star which is filling its Roche lobe and is losing mass through L_1 is called the donor (subscript 'd'). The star which is receiving mass is called the accretor (subscript 'a'). At the onset of mass transfer, the donor will be the primary component of the binary system and the accretor the secondary.

RLOF is initiated when the radius of the donor becomes larger than the Roche-lobe radius R_L. The Roche-lobe radius is defined as the radius of a sphere with the same volume as the lobe. It is dependent on the mass ratio $q \equiv M_{\text{donor}}/M_{\text{accretor}}$ of the two components and is defined as (Eggleton, 1983a)

$$\frac{R_L}{a} = r_L = \frac{0.49q^{2/3}}{0.6q^{2/3} + \ln\left(1 + q^{1/3}\right)}. \tag{4.10}$$

Depending on when mass transfer occurs in the evolution of the components, the system and components will respond to mass transfer differ-

ently.

Before describing the effects of mass transfer, another effect is explained: tidal interactions.

4.4.1 Tidal interactions in close binaries

In close binaries, tidal effects will lead to: circularisation of the orbit and synchronous rotation of the two components.

Circularisation Take an initially eccentric orbit. The stars are not rigid and their shapes can get distorted. The gravitational attraction between the two components causes bulges away and towards the other component[2]. At periastron, the gravitational pull on the surface of the other component will be strongest. As the bulges do not rise and fall instantaneously, the bulges will lag with the actual gravitational pull as the components move around each other. This lag pulls the components back as they move towards the apastron. The new apastron will be lowered compared to the apastron of the previous orbit. Hence the eccentricity is lowered and will eventually reach zero.

Synchronisation When the rotation rates of the two components are synchronised with the orbital period, the system is said to be synchronised. Synchronisation of the binary system is based on the same principle as the circularisation. If the rotational velocities are not synchronised with the orbital period, the changing bulges arising on the surface of the two components during the orbit will induce torque on the components. This torque will synchronise the rotation velocities of the components with the orbital period. The binary is now tidally locked as the two components are always facing the same surface towards one another.

For massive main-sequence stars, the tidal synchronisation timescale is short compared to their main-sequence lifetime if the orbital period is shorter than about a week (Zahn, 1975). In systems with orbital periods shorter than 2-3 days, synchronous rotation implies rapid rotation rates (e.g. Detmers et al., 2008).

4.4.2 Mass transfer and the orbital parameters

The change in the orbital parameters due to mass transfer is investigated by looking at the total angular-momentum change of the system. The total

[2]These bulges are also seen in the oceans on Earth. The tides are a result of the changing gravitational pull due to the Earth's rotation around its axis and the Sun.

angular momentum of the system is the sum of the angular momentum of both components and is given by

$$J^2 = G\frac{M_1^2 M_2^2}{M_1 + M_2} a\left(1 - e^2\right). \tag{4.11}$$

The change in orbital angular momentum is defined by

$$2\frac{\dot{J}}{J} = \frac{\dot{a}}{a} + 2\frac{\dot{M_1}}{M_1} + 2\frac{\dot{M_2}}{M_2} - \frac{\dot{M_1} + \dot{M_2}}{M_1 + M_2} - \frac{2e\dot{e}}{(1 - e^2)}, \tag{4.12}$$

where the derivatives are represented by a dot over the parameter. In the following discussion on mass transfer, the parameters belonging to the primary and secondary component will be replaced by their respective status as donor and accretor. Mass is lost from the donor and hence $\dot{M_1} = \dot{M_d} < 0$. The accretor gains mass and thus $\dot{M_2} = \dot{M_a} > 0$. In close binaries the orbit is circularised and $e = 0$. The rest of the Section assumes a circularised orbit.

Conservative mass transfer

If mass transfer is conservative, it follows that

$$\dot{M_a} = -\dot{M_d} \quad \text{and} \quad \dot{J} = 0. \tag{4.13}$$

The equation of orbital angular-momentum change can then be simplified to

$$\frac{\dot{a}}{a} = -2\left(\frac{\dot{M_d}}{M_d} + \frac{\dot{M_a}}{M_a}\right) = 2\frac{\dot{M_d}}{M_d}\left(\frac{M_d}{M_a} - 1\right). \tag{4.14}$$

The factor $\dot{M_d}/M_d < 0$ as the donor loses mass. The orbit will thus shrink when $M_d > M_a$ and expand when $M_d < M_a$. The onset of mass transfer will shrink the Roche lobe. When mass reversal is reached during mass transfer the period/Roche lobe will widen again.

Using Kepler's third law $P^2 \propto a^3$ whilst solving the previous equation results in the following relation between the initial and final masses and period

$$\frac{P}{P_0} = \left(\frac{M_{d,0}}{M_d}\frac{M_{a,0}}{M_a}\right)^3, \tag{4.15}$$

where the initial values are denoted with the subscript '0'.

Non-conservative mass transfer

In this scenario mass is lost from the system through the second Lagrangian point. The following relations hold for non-conservative mass transfer

$$\dot{M_a} = -\epsilon\dot{M_d} \quad \text{and} \quad \dot{J} \neq 0. \tag{4.16}$$

Here, ϵ is the fraction of mass lost from the donor that is accreted by the accretor. It generally consists of three contributions (Soberman et al., 1997):

- Fraction of mass lost from the donor through winds - α: The mass lost from the donor through winds is assumed not to interact with the system. It takes away angular momentum from the donor.
- Fraction of mass ejected from the surface of the accretor - β: In some cases, mass transferred to the accretor can be immediately re-ejected from the surface of the accretor through enhanced winds.
- Fraction of mass lost from a circumbinary toroid - δ (with radius $a_r = \gamma^2 a$): Matter can gather around the binary components as a circumbinary disk/toroid. Mass can be transferred to/from this disk.

The mass-transfer efficiency ϵ is defined as $\epsilon = 1 - \alpha - \beta - \delta$. Following Tauris and van den Heuvel (2006), the solution of Equation (4.12) is

$$\frac{a}{a_0} = \left(\frac{q}{q_0}\right)^{2(\alpha+\gamma\delta-1)} \left(\frac{q+1}{q_0+1}\right)^{\frac{-\alpha-\beta+\delta}{1-\epsilon}} \left(\frac{\epsilon q+1}{\epsilon q_0+1}\right)^{3+2\frac{\alpha\epsilon^2+\beta+\gamma\delta(1-\epsilon)^2}{\epsilon(1-\epsilon)}}, \quad (4.17)$$

where the subscript '0' denotes initial values. Be reminded that $q \equiv M_d/M_a$ and thus it is possible that for the final system $q > 1$. It is worth noting that a system which is observed post-mass transfer, such as an Algol system, will by definition still have $q \equiv M_2/M_1 \leq 1$ for the observer as the primary is the more massive component. It is only when the evolution of the system is analysed that it becomes clear that, compared to the initial system, the original donor (the original primary) now became the secondary an the initial secondary now became the primary.

Conservative or non-conservative?

One of the questions in binary interactions is when and how mass transfer happens conservatively. An example is the spin-up of the accretor. The spin-up of the accretor should prevent mass transfer from being conservative. The tidal interactions in close binaries will prevent the spin-up of the accretor as they will carry away the angular momentum gained by the accretion of material. Mass transfer in close binaries is indeed shown to be conservative (de Mink et al., 2007). For binaries which are sufficiently far apart for tidal interactions not to be effective, the accretor is expected to spin up. In practice, close-to-conservative mass transfer also happens in systems in which the accretor is expected to spin up significantly, in systems with an orbit which is too wide for tidal interactions to counteract the spin-up. The mechanisms behind it is not yet understood.

4.4.3 Response of the components

As the donor loses mass, it is brought out of hydrostatic equilibrium. The star consequently has to grow or shrink to re-establish its equilibrium. Also the accretor is brought out of equilibrium and will need to restore it by expanding or shrinking. Above, it was demonstrated that the onset of mass transfer will shrink the orbit and consequently the Roche lobe.

The stability of mass transfer depends on three factors:

1. How the radius of the donor responds to the mass loss.
2. How the orbit (and R_L) change during mass transfer.
3. How the accretor reacts to the mass that is transferred.

The stability of mass transfer is derived from points 1. and 2. If the radius of the donor shrinks at a rate smaller or comparable to the shrinkage of R_L, mass transfer is stable. If the radius of the donor expands (rapidly), mass transfer will become unstable. Stable mass transfer will not 'destroy' the binary, meaning that the result of stable mass transfer is still a binary but possibly with other fundamental parameters. Unstable mass transfer may lead to a destruction of the binary in the sense that the two components may merge to become one single massive star.

The next two Sections distinguish three cases of mass transfer: case A, case B and case C. They are defined according to the evolutionary state of the donor upon initiation of mass transfer. Here, the response of the donor and accretor are discussed.

Response of the donor

We distinguish between two internal structures of the star: a star with a radiative envelope and one with a convective envelope.

If the envelope of a star is *radiative*, the outermost layers have a low density. Consequently, if the donor loses its outermost radiative layers it will not alter its structure significantly. The consequence is that the radius of the donor will shrink and it becomes denser.

If the donor loses the outer layers of its *convective* envelope, its radius will expand. The inner layers of a convective envelope are hotter and more luminous. Upon mass loss these hotter layers will be brought to the surface of the star. In order to restore equilibrium, the donor will have to expand.

Effects on the accretor

The accretor gains mass in the process of mass transfer. This extra mass will influence the evolution and parameters of the accretor in three clear ways:

Table 4.1: Summary of radial response of the donor and accretor to mass transfer

Donor	$\dot{M} < 0$	radiative envelope	$R \searrow$
		convective envelope	$R \nearrow$
Accretor	$\dot{M} > 0$	radiative envelope	$R \nearrow$
		convective envelope	$R \searrow$

- Rejuvenation: Section 3.2 has shown how the lifetime of the star decreases with increasing mass. The mass gained during mass transfer results in a new higher mass than the accretor initially started with. This will thus lead to a decrease in the lifetime of the accretor. It will now evolve further as if it were initially born with the new higher mass. Although the star will have lived for a longer time already, it will appear as it has lived shorter on the evolutionary track of a single star with its corresponing new mass. This effect is called rejuvenation of the accretor.

- Spin-up: The mass that is transferred also carries angular momentum. As the mass falls on the accretor, its angular momentum will increase and lead to a spin-up of the star. This can bring the accretor to rotate close to its critical rotation velocity, above which the rotational force will tear the star apart. The accretor only needs to receive 10% of its original mass to rotate close to this critical velocity (Packet 1981). In order to get rid of this rotation, the accretor might induce enhanced winds, which carry away angular momentum. This process leads to non-conservative mass transfer. Spin-up does not occur in close binaries as tidal interactions transfer the angular momentum to the orbit.

- Re-adjustment of equilibrium: Also the acrcetor will be brought out of equilibrium by mass transfer. The mass which is gained will compress the outer layers of the envelope, releasing gravitational energy. When this energy release is larger than the luminosity of the star, it is brought out of equilibrium. When the envelope is *radiative*, the accretor will expand to restore its equilibrium. If the envelope is *convective*, the accretor will shrink.

Table 4.1 summarises the radial response of the donor and accretor to mass transfer. If the accretor expands as a response to mass transfer, it might also fill its Roche lobe. The result is a *contact binary*, which is a binary in which both the donor and accretor are filling their Roche lobe.

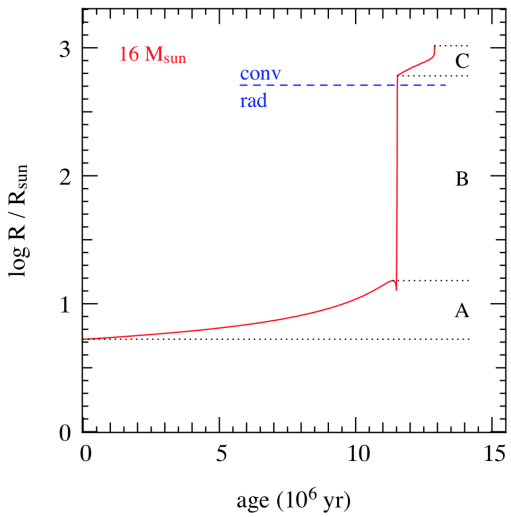

Figure 4.7: Radial expansion of a $16M_{\odot}$ star as a function of its age. The parts A, B and C correspond to the types of mass transfer (case A, case B and case C). The point in the evolution where the envelope becomes convective is also indicated. Figure taken from Pols' lecture notes.

4.4.4 Case A

In this case, mass transfer happens whilst the donor is still burning hydrogen on the main sequence. The envelope of the donor (a massive star) is thus radiative. Case-A mass transfer is stable. As explained in Chapter 2, the radius of the star expands already slightly during the main-sequence evolution. The same figure used there is here presented again here, in Figure 4.7. The different types of mass transfer are indicated with their respective letters (A, B and C).

A diagram of the effect of mass transfer on the components is given in Figure 4.8 for a binary with $M_1 = 10.0M_{\odot}$, $M_2 = 8.9M_{\odot}$ and $P = 2.2$ days. The two upper panels are discussed first. From A to B in the diagrams, the primary is evolving according to single-star evolution. At point B, the primary fills its Roche lobe and RLOF is initiated. Between point B and C the equilibrium radius of the donor is larger than R_L. When mass transfer is initiated, the donor will first have to re-adjust its radius to find equilibrium. This leads to a rapid phase of mass transfer happening on the thermal timescale of the donor. At point C the donor has re-established thermal equilibrium and the rapid phase of mass transfer is followed by a slow phase of mass transfer, driven by the main-sequence evolution of the donor. Mass transfer now continues on the nuclear timescale of the donor. Point D corresponds to the end of the main sequence phase of the donor, when it detaches from its Roche lobe for a short time. During hydrogen

shell-burning the donor re-expands, giving rise to further mass transfer past point D (on a much faster timescale as it is driven by the rapid expansion of the donor). Everything happening after point D does not belong to case A anymore and is not further discussed in this section. Case-A mass transfer is thus characterised by a phase of fast mass transfer on a thermal timescale, followed by a phase of slow mass transfer on a nuclear timescale.

The other panels in Figure 4.8 show the effect of mass transfer on both components. From B to C, both components are brought out of equilibrium. The donor is somewhat less luminous due to mass loss, whilst the secondary is somewhat more luminous as a result of accretion (for a reference to single-star evolution, see Figure 2.7). At point C both stars have re-gained thermal equilibrium. Phase C–D is a long-lived phase of nuclear-timescale mass transfer. The accretor has a luminosity and radius appropriate for a main-sequence star of its increased mass. The now less-massive donor is over-luminous for its mass and has a larger radius than the accretor.

These properties are common for Algol-type binaries.

4.4.5 Case B, C and common envelope

Additionally to case A, there is also case B and C mass transfer. These are also indicated in Figure 4.7 for a $16M_{\odot}$ star. Case B is referred to as mass transfer which is initiated at the time when the donor left the main sequence and started hydrogen shell-burning. Case-C mass transfer is when the donor also finished hydrogen shell-burning and initiated helium burning.

These two cases are not important for the research performed in this thesis. Therefore, if the reader wants to know in more detail how mass transfer happens in these two cases, Tauris and van den Heuvel (2006) and Pols' lecture notes (ch. 6-8, available online[3]) are excellent sources. The end result of unstable mass transfer is briefly explained here.

At the time of helium shell-burning and, depending on the mass, partly during hydrogen shell-burning, the envelope of the star is convective. As explained in Section 4.4.3, the star will even expand more when mass transfer is initiated whilst the envelope is convective. Mass transfer during this stage is a runaway process, leading to a common envelope phase. The donor expands so rapidly that its envelope engulfs the other component. Due to friction the period shrinks, causing a spiral-in of the two components. The envelope can either be expelled or the two stars merge. The theory behind common envelope evolution is not well understood, especially for massive stars as observational constraints are scarce (Taam and Sandquist, 2000).

[3] https://www.astro.ru.nl/~onnop/education/binaries_utrecht_notes/

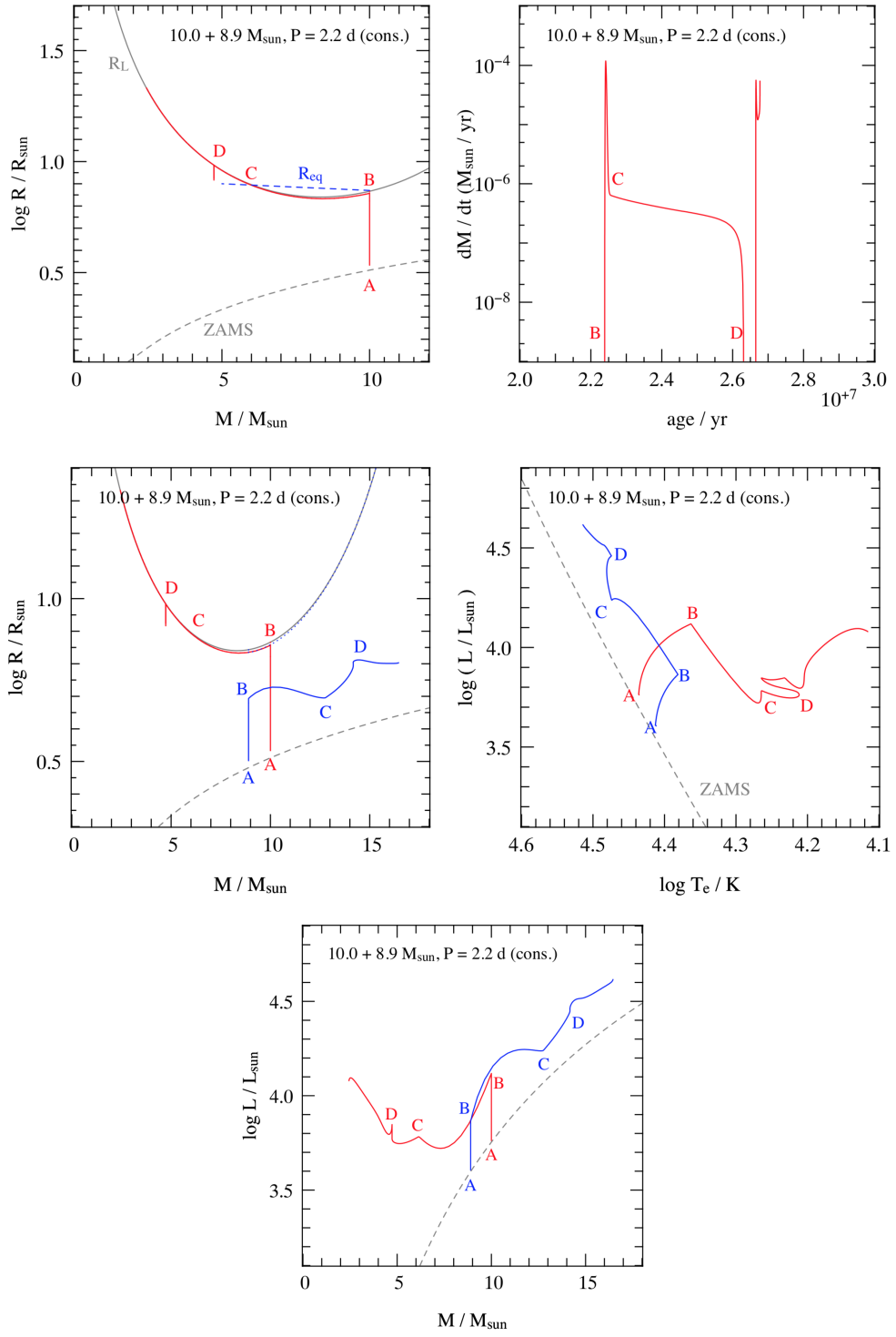

Figure 4.8: Mass-radius diagram of the primary star in a massive binary with initial parameters $M_1 = 10.0 M_\odot$, $M_2 = 8.9 M_\odot$ and $P_{\rm initial} = 2.2$ days. The blue-dashed line indicates the equilibrium radius. The grey-solid line indicates the Roche-lobe radius R_L. The red-solid line shows the path of the primary/donor. The upper-right diagram shows the corresponding mass transfer rate as a function of time. The middle-left panel shows the same mass-radius diagram as above also showing the secondary (blue). The middle-right panel shows the HRD tracks of the two components. The bottom panel shows the luminosity-mass diagram for both components. Points A, B and C are marked. See text for explanation. Figure taken from Prof. O. Pols' lecture notes.

4.5 Detecting compact objects

Binaries provide a unique way of observing the most massive compact objects: BHs (other compact objects are of course also observed with binaries). The interaction between a BH and its companion star reveals the presence of this otherwise practically invisible object.

First there is the detection of SB1s. The star companion to the BH, which is still radiating, is observed with clear motion, but no companion is detected. A further analysis of such a system could lead to the discovery that the hidden companion is a BH.

Mass transfer onto a compact object results in the production of X-rays. Binaries where a compact object is accreting and emitting X-rays are called X-ray binaries.

Recently, modern gravitational wave detectors have observed the merger of two compact objects (e.g. Abbott et al., 2016b,a, 2017). This made it possible to probe one of the final stages in binary evolution.

Although clear signs of binary interactions exist (X-ray binaries, Algols, ...), observational evidence for establishing binary-evolution schemes remains scarce. Below, two schemes are explained involving very close massive binaries. The components are close and massive enough such that tidal forces make them rapid rotators. As explained in Chapter 2, rapidly rotating massive stars are thought to evolve homogeneously. Although the rotational-mixing efficiency is uncertain, low-metallicity environments are favoured as weaker winds prevent the spin-down of stars (Yoon and Langer, 2005). Hence rotational mixing might be more effective here.

4.5.1 Black-hole mergers

The merger of BHs within the Hubble timescale, i.e. such that we can observe the event, requires BHs in very close orbit with each other. In most scenarios, the evolution from an OB+OB binary towards a double compact-object binary involves an OB+OB binary with an orbital separation large enough to avoid early merger. Consequently, a phase of common envelope is needed to shrink the orbit. As previously stated, the common envelope phase for massive stars is theoretically not well understood (Taam and Sandquist, 2000). The uncertainties for double BH systems are so large that the predicted rates of BH binaries from the common envelope channel are very uncertain (Abadie et al., 2010).

Marchant et al. (2016) and de Mink and Mandel (2016) proposed a new evolutionary scenario towards massive-BH merger within the Hubble timescale that does not involve uncertain binary interactions. They suggest homogeneously evolving massive binaries with short (< 2 days) orbital periods to be the progenitors of the BH mergers. The homogeneous

evolution of these massive stars (due to the rapid rotation) prevents radial expansion of the components. This prevents the orbit from widening due to binary interactions, keeping the binary in a close orbit. A schematic representation of their proposed evolutionary scenario is given in Figure 4.9. It shows the evolution of a binary with $M_1 = 70M_\odot$, $M_2 = 56M_\odot$ and $P_{\text{initial}} = 1.1$ days. What is seen in the first stage at the zero-age main sequence (ZAMS) is that the stars are in contact with each other. They are born so close to each other they both fill their Roche-lobe. Mass will flow from the primary towards the secondary until they have equal masses (at the terminal-age main sequence or TAMS). The primary explodes as a supernova (SN) or produces a gamma-ray burst (GRB), which is an extremely bright gamma-ray source most likely thought to be associated with the core collapse of a homogeneously evolved massive star. The primary is now a massive BH and the secondary also evolves towards a SN/GRB. The two massive BHs merge on a timescale of 1 700 Myr.

4.5.2 Ultra-luminous X-ray sources

In systems similar to the ones described above but with extreme mass ratios ($M_2/M_1 < 0.5$), only the more massive star is massive enough to undergo strong mixing from rotation (Marchant et al., 2017). The primary star evolves homogeneously and becomes a massive BH. The secondary does not evolve homogeneously as it is not massive enough. It will expand as it evolves and might initiate mass transfer onto the BH. The accretion of the BH would be seen as an ultra-luminous X-ray source (ULX). This stage in the evolution would be seen as an extremely luminous X-ray point source ($L_X > 10^{39}$ erg s). It is often observed in star-forming regions (Kaaret et al., 2017). A scheme of binary evolution towards the ULX phase is shown in Figure 4.10.

With their high X-ray luminosities, ULXs defy our understanding of accretion physics and challenge BH models as they have luminosities above the Eddington limit.

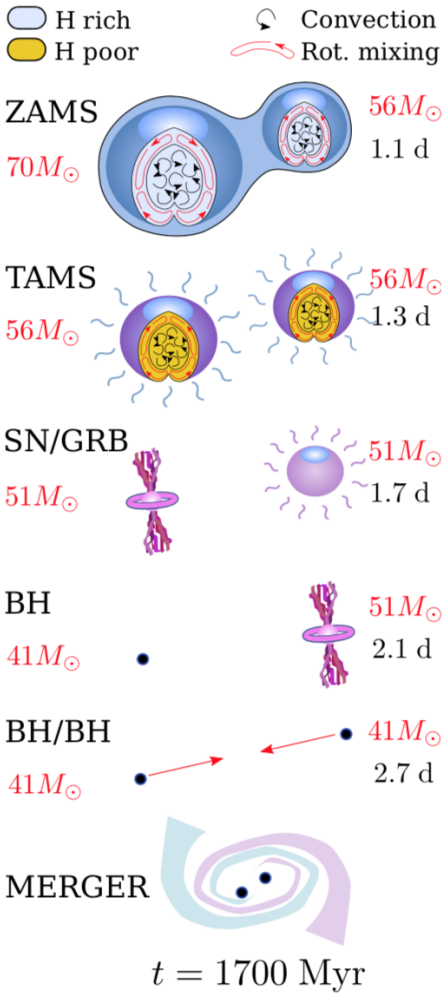

Figure 4.9: Evolution scheme of a binary with $M_1 = 70M_\odot$, $M_2 = 56M_\odot$ and $P_{\rm initial} = 1.1$ days towards a BH merger. Different critical stages are indicated, together with the masses (red) and period (under secondary mass) at that stage. See text for more explanation. Figure taken from Marchant et al. (2016).

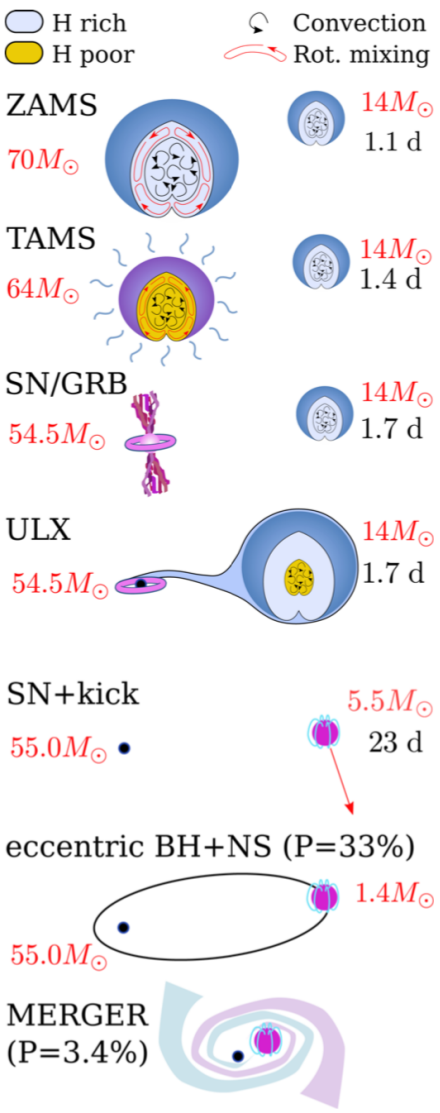

Figure 4.10: Evolution scheme of a binary with $M_1 = 70M_\odot$, $M_2 = 14M_\odot$ and $P_{\rm initial} = 1.1$ days towards the ULX phase. Different critical stages are indicated, together with the masses (red) and period (under secondary mass) at that stage. See text for ore explanation. Figure taken from Marchant et al. (2017).

5 A brief history of BAT99 126

The name BAT99 126 is taken from the IVth catalogue of WR stars in the LMC by Breysacher et al. (1999). In 1964, Westerlund and Smith classified BAT99 126 (or as they named it WS50, also called HD269956 or HD38472) as a single WN star. Merely four years later, it was classified as a WN4 + OB binary (Smith, 1968). As time went by, our telescopes became more and more advanced, resulting in higher-resolution data and more precise analysis.

Roughly 30 years later, an orbital period was derived. Foellmi et al. (2003b) suggested that BAT99 126 was a WN4 + O8 binary system, with an (uncertain) orbital period of 25.5 days. They claimed the orbit to be "suspicious, although (weak) periodic signals were visible". In 2011, Graczyk et al. derived a photometric period of 1.55 days from the OGLE light curve. This photometric period is significantly smaller than the previously derived period.

Shenar et al. (2019) noticed the inconsistency of the two derived periods. They gave two possible explanations: BAT99 126 might be a triple system or an error occurred on the orbital period derivation. They classify BAT99 126 as WN3 + O7 V + OB. They applied for more data with the Very Large Telescope in Chile, as they suggested it is a rare progenitor candidate of a gravitational wave merger. These data were obtained and will be used in this thesis.

The combination of the WR star and the close 1.55 day period - whether this period belongs to the orbit of the WR star or not - make BAT99 126 an excellent environment for investigating close-binary interactions and the influence of binarity on the formation of WR stars. As the WR star is so short-lived, it is an excellent age estimator for the system. With a known age it is possible to perform tailored modelling of the system, in order to investigate whether the close binary can be explained by general close-binary physics.

Part II

Analysis and Results

The used methods and results of the analysis of BAT99 126 are presented here. Before that, the data is first presented in Chapter 6.

Chapter 7 presents all the results obtained from a spectroscopic analysis, by using the 10 high-resolution spectra available. Chapter 8 combines the results obtained in the previous chapter with the available photometric data. After all the data is analysed, simulations are performed to investigate the evolution of the system. The methods and results of the evolutionary analysis are explained in Chapter 9.

This part ends with the conclusions and outlook in Section 10.

6 Data & Reduction

This Chapter provides some preliminary information about the data used for the analysis later on. The two types of data used are spectroscopic and photometric data, described in Sections 6.1 and 6.2 respectively.

6.1 Spectroscopic data

The spectroscopic data used in this thesis were taken with the high-resolution Ultraviolet and Visual Echelle Spectrograph (UVES, Dekker et al., 2000) mounted on the Very Large Telescope in Chile. It has a blue and a red arm, covering a wavelength range of 3 800 - 5 000 Å and 5 800 - 9 000 Å respectively. We note that there is a gap in the observations between 5 000 - 5 800 Å. All data that was obtained has a resolution $R \sim 31\ 500$.

The spectra are taken over a period of two months, starting October 3rd 2018 until December 5th 2018. Table 6.1 shows the dates of the observations. The first column is the modified Julian Date (MJD) which is equal to the Julian Date [1] minus 2 400 000.5. The second column is the Heliocentric Julian Date (HJD). Instead of using the time at which the light of the star reaches Earth, this is the time at which the light has reached the centre of the Solar system. The third column shows the time of the observation in UTC time. Calculations from MJD to UTC time are performed with the online NASA calculator[2]. The second to last column shows to what phase of the 1.55-day orbit the observation corresponds. It can be seen there is a good phase coverage available for this close binary, as the observations cover phases roughly $\Delta\phi \approx 0.1$ apart. The last column shows to what phase of the 25.5-day orbit the observation corresponds.

[1] The Julian Date is a dating system often used in astronomy. It is a continuous count of days since the beginning of the Julian Period. The reference day/epoch is January 1st 4713BC at 12 o'clock.

[2] `https://heasarc.gsfc.nasa.gov/cgi-bin/Tools/xTime/xTime.pl`

Table 6.1: Dates on which the UVES spectra were taken. The second-to-last column shows to what phase of the 1.55-day orbit the observation corresponds. The last column shows to what phase of the 25.5-day orbit the observation corresponds.

MJD	HJD	YYYY-MM-DD HH:MM:SS UTC	$\phi_{1.55d}$	ϕ_{25d}
58394.29	58394.80	2018-10-03 06:59:36	0.32	0.05
58411.23	58411.73	2018-10-20 05:31:12	0.23	0.72
58413.24	58413.74	2018-10-22 05:45:36	0.52	0.80
58437.31	58437.81	2018-11-15 07:26:24	0.03	0.74
58438.22	58438.71	2018-11-16 05:16:48	0.61	0.77
58444.10	58444.61	2018-11-22 02:24:00	0.40	0.0
58446.09	58446.61	2018-11-24 02:09:36	0.68	0.08
58446.25	58446.63	2018-11-24 06:00:00	0.78	0.09
58448.28	58448.78	2018-11-26 06:43:12	0.09	0.17
58457.29	58457.80	2018-12-05 06:57:36	0.89	0.52

The spectra were taken with a desired signal-to-noise-ratio (S/N) > 100. This is in order to detect components with spectral types B1 V and earlier. The desired S/N > 100 requires a total exposure time of about one hour for each observation. In order to filter out any cosmic radiation that might reach the telescope during this exposure, each observation is split into three subsequent observations of about 20 minutes.

Adding subsequent spectra

Each observation consists thus of six observations, three blue parts and three red parts, taken with the blue and red arm respectively. The spectra that are used are reduced with the UVES pipeline. These individual spectra are then added together[3] to create a spectrum with the desired S/N. The average S/N of each individual spectrum is around ~ 60. The coadded spectra have on average S/N ~ 110. An example of the difference in S/N between one of the three individual spectra on each arm and the coadded spectrum is shown in Figure 6.1, the blue part on the left and for the red part on the right. The y-axis shows the mean-subtracted flux. The bottom panels show a zoom-in on part of the upper panels in order to see the difference better. Figure 6.2 shows an individual spectrum and the coadded spectrum zoomed in on a section where a cosmic ray is present in the single spectrum (note that it is not the same spectrum as in Figure 6.1). It can be seen that for the added spectra the presence of the cosmic ray is reduced.

[3]By adding spectra together, the S/N is enhanced by $\sqrt{N}$ with N the number of spectra.

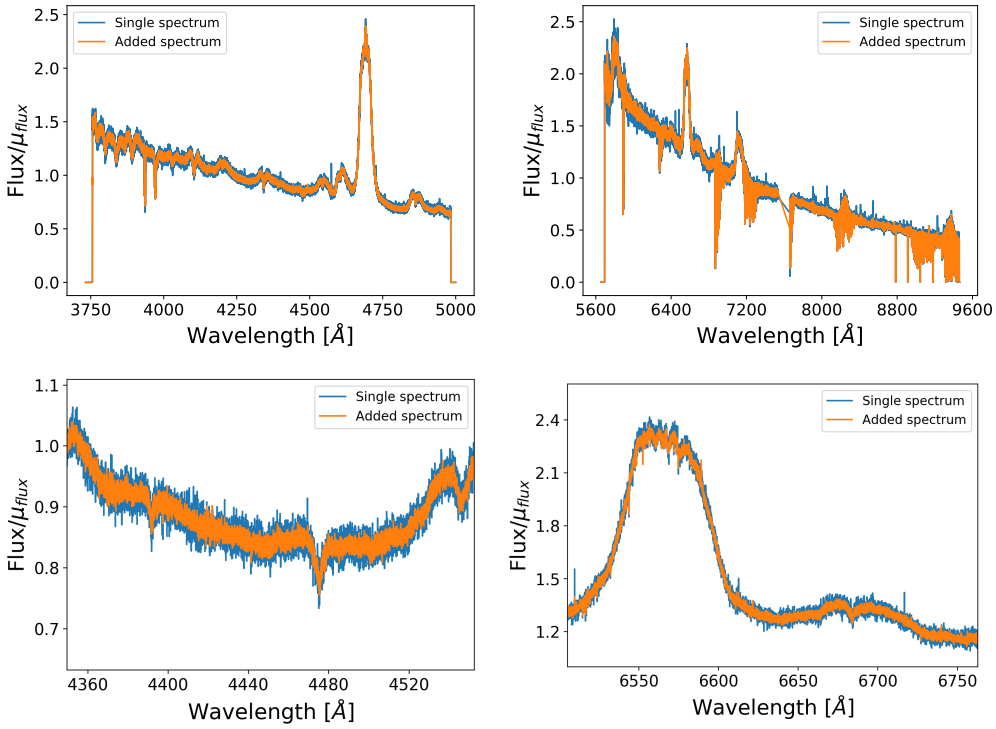

Figure 6.1: Single spectrum (blue) and the resulting spectrum after adding the three subsequent spectra (orange). The y-axis shows the mean-subtracted flux. Left: blue part. Right: red part. Top: whole wavelength range. Bottom: zoom-in.

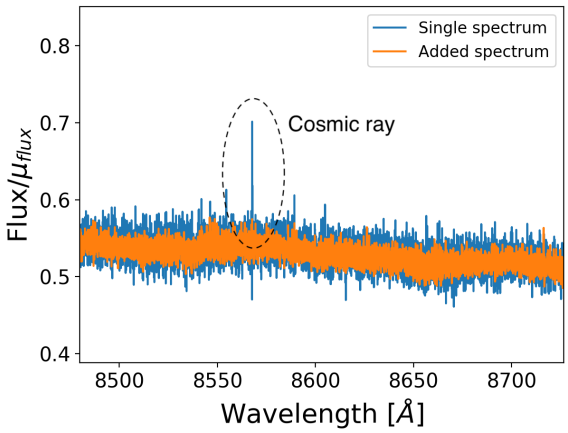

Figure 6.2: Same as Figure 6.1, but zoomed in on a region where a cosmic ray is present in the single spectrum and filtered out in the coadded spectrum.

Normalisation

For the research done in this thesis, only the spectral lines are of interest. With a raw spectrum, it is hard to determine the Doppler-shifted wavelengths of the emission lines, as it is equally hard to compare the relative strengths of different emission lines. The reason for this is that it is only the intensity relative to the continuum that matters. Therefore the spectrum is normalised, which means that the continuum of the star is put equal to one at all wavelengths.

For most stars a spline of the continuum can be created by interpolation of manually selected points in the spectrum. Due to the broad emission lines from the WR star however, the continuum is lost, making the normalisation difficult.

Each of the two spectra, coming from the red and blue arms, was separately normalised by using a model spectral energy distribution (SED). As the wavelength coverage of the spectra ($\sim$ 3 800 Å - 9 000 Å) is in the Rayleigh-Jeans domain, massive stars in this regime will have a very similar SED (Section 3.4). Therefore the model SED was chosen to be a PoWR model, belonging to an O-type star with an effective temperature $T_{\text{eff}} = 40\ 000$ K and $\log g = 4.0\,[\text{cm s}^{-2}]$.

This model represents the SED of the star without it being affected by interstellar reddening or thus the intrinsic energy distribution of the star. The light that reaches the telescope is however influenced by this interstellar reddening and thus this needs to be accounted for whilst using the model. The normalisation procedure for each spectrum is fitting the model SED to the spectrum whilst applying reddening to the model (see Appendix A for details on how this reddening is taken into account). The fitting procedure determines the optimal reddening for the model whilst obtaining the optimal fit. The fit was performed with the built-in Python function *scipy.optimize.minimize*[4]. The method that was used to find the optimal continuum fit is the Newton-Raphson method.

In order to obtain the normalised spectrum, the original spectrum is divided by the fitted curve. A visualisation of this normalisation procedure for one of the spectra is shown in Figure 6.3. The upper panel shows the data of the blue arm of UVES and the lower panel shows the data of the red arm. The original mean-subtracted spectrum, i.e. before normalisation, is shown in blue. The fitted model is shown with a dashed orange line. The normalised flux, obtained by dividing the original data by the fitted model, is shown in green. Figure 6.4 shows the concatenated normalised flux from the same spectrum. The gap in wavelength between the red and blue arm between $\sim$5 000 Å - 5 800 Å can be seen as a noiseless part in the spectrum

[4] `https://docs.scipy.org/doc/scipy/reference/generated/scipy.optimize.minimize.html`

with a value of one.

The end result is ten normalised spectra with a S/N > 100, covering both the short 1.55-day orbital period published by Graczyk et al. (2011) and the spectroscopic 25.5-day orbit suggested by Foellmi et al. (2003b).

Spectral lines visible in the spectrum

There are four types of spectral lines/features visible in the spectra. One of them is the presence of cosmic lines in the individual spectra. However, as shown in Figure 6.2 the cosmic lines are filtered out by coadding the spectra.

Three types of spectral lines are visible in the spectrum. There are the absorption and emission lines belonging to the different components of the system. An example of each was already given in Figure 3.3. As the telescope is ground-based, the radiation of the star passes through the atmosphere of the Earth. As such, also absorption features corresponding to the molecules present in the Earth's atmosphere, such as OH, will be visible in the spectrum. Absorption lines corresponding to atmospheric molecules are called *telluric lines*. An example is shown in Figure 6.5. Other features found in spectra are diffuse interstellar bands, caused by material in the interstellar medium.

6.2 Photometric data

The photometric data available for BAT99 126 is a light curve (LC) and data points from different passbands. The LC is taken in the frame of the Optical Gravitational Lensing Experiment (OGLE) project (Udalski et al., 1992). The resolution of OGLE is 0.44"/pixel, meaning that it can resolve objects at 0.44" distance from each other. At a distance of 46.97 kpc (Pietrzyński et al., 2013), in the LMC this corresponds to an angular resolution of about 3.3×10^{13} km. Objects closer together will hence be seen in the same light curve.

The OGLE LC covers a time span of roughly 13 years (October 2001 - March 2014), in which over 800 data points were accumulated. The photometric data is shown in Figure 6.6 as a function of the time they were taken. It can be seen that some larger blocks of data points are alternated with some gaps. This is most likely due to the setup of the monitoring program. On average, every 5 days a data point is obtained. An image of the OGLE LC phased with the published period of 1.552945 days (Graczyk et al., 2011) is shown in Figure 6.7. Two eclipses can be seen, one at $\phi = 0$ and one at $\phi = 0.5$. This indicates a circular orbit. Moreover it can be seen

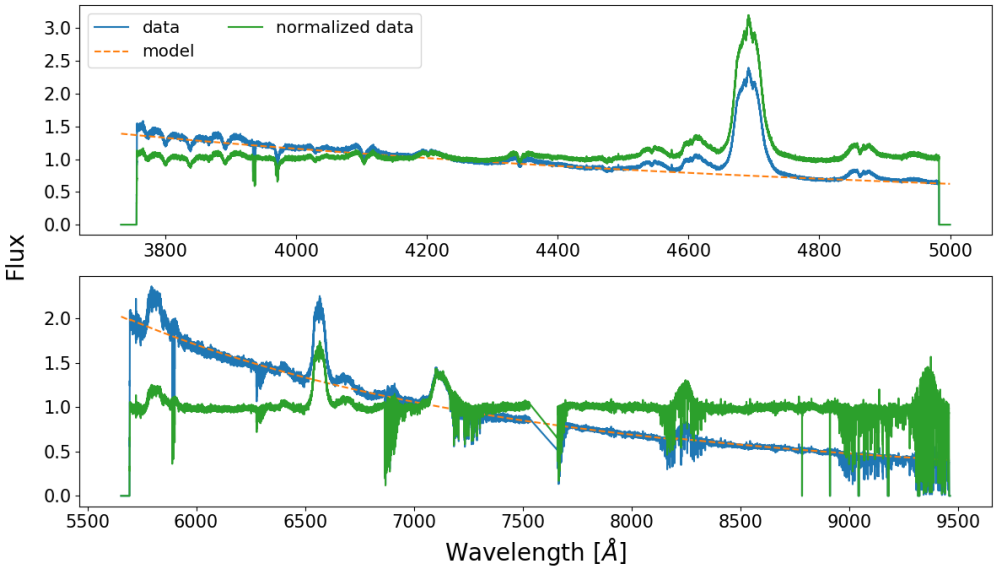

Figure 6.3: Visualisation of the normalisation process for one of the spectra. The original data is shown in blue, the reddened and fitted model is represented by the dashed orange line and the normalised flux is shown in green. The upper panel shows the data from the blue arm and the lower panel the data of the red arm.

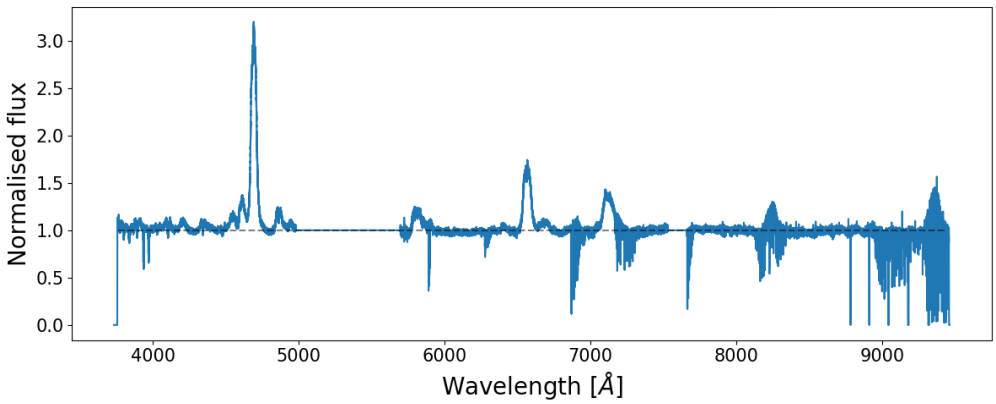

Figure 6.4: The concatenated normalised flux from the same spectrum as in Figure 6.3. The dashed black line shows a value of one for the normalised flux.

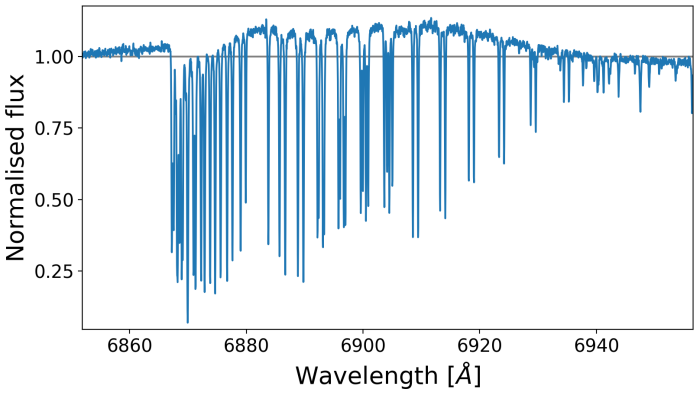

Figure 6.5: Telluric lines in the spectrum of BAT99 126. Note that the telluric lines are here located in an emission line of the WR star.

that both components have a similar luminosity/brightness as the eclipses have similar depths.

Other photometric observations in different bands are also available for BAT99 126. These data cover the wavelength range from 2 000 Å up to 220 000 Å. Table C.1 in Appendix C shows the flux and magnitude at the corresponding passbands of the available data points.

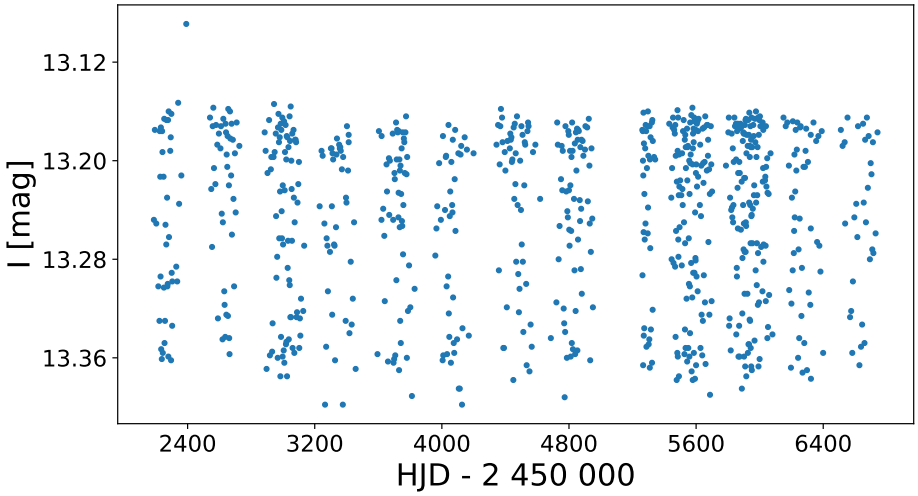

Figure 6.6: Photometric data as a function of time at which it was taken for BAT99 126 obtained with OGLE.

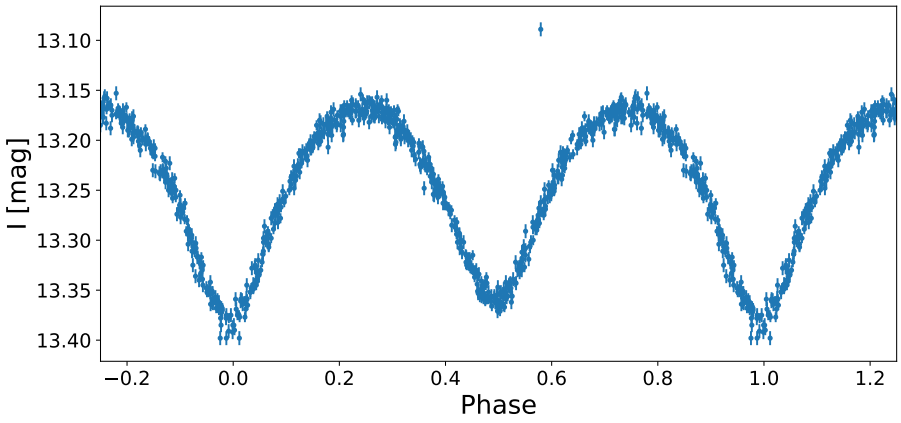

Figure 6.7: OGLE light curve of BAT99 126 phase folded with a 1.55-day orbit.

7 Spectroscopic analysis

The spectrum of a (multiple) system holds a lot of information. It tells the observer how many components are present in the system. For each component, the spectral type and radial velocities can be determined. Since massive stars have a lot of mutual spectral lines, the task of classifying the spectral lines to the correct component can be a difficult one.

This Chapter explains the analysis and results obtained from a study of the spectroscopic data. First, the multiplicity of the system is derived in Section 7.1. Based on these results, it is possible to calculate the rotational velocities (Section 7.2), make a spectral classification of the components (Section 7.3) and determine their radial velocities (Section 7.4). Section 7.5 goes into detail about the contribution of the individual components to the total spectrum. Finally, this Chapter ends in Section 7.6 with a discussion on the obtained results.

7.1 Multiplicity of the system

Before anything else, the multiplicity of the system is derived. In order to determine the number of components present in the system all, the spectral lines visible in the spectrum are identified. Some lines will show multiple components whereas other lines will be only coming from one of the components. By identifying the number of features at each atomic transition, the multiplicity of the system can be easily deduced.

Figure 7.1 shows different spectral lines with multiple components. Different spectra correspond to different phases in the 1.55-day orbit. Not all spectra are shown in order to increase the visibility of the individual spectra. The WR star, whose presence was already known, is called component A. It is responsible for the broad emission features in the figures. There are also two other components visible in these lines. In the bottom right panel only three spectra are shown. This is to show clearly the two

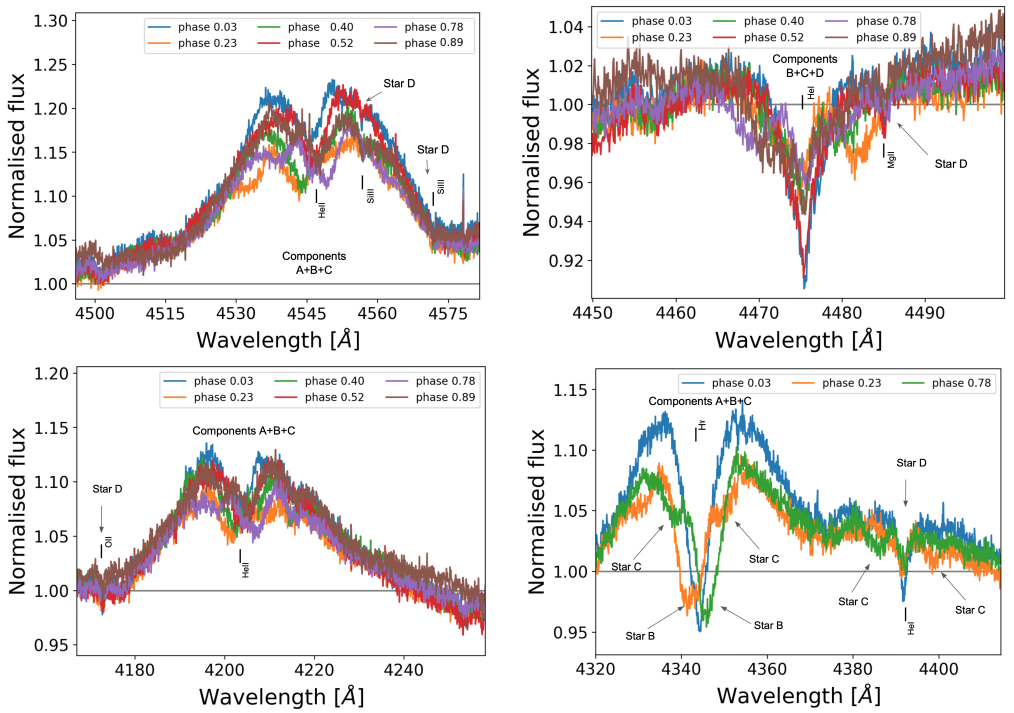

Figure 7.1: Different spectral lines showing multiple components. Spectra correspond to different phases of the 1.55-day orbit, indicated in the legend. The WR star is labeled star A. Three other components (B, C and D) are also indicated on the figures.

different absorption features visible in the broad emission lines. A motion of the spectral lines from component B and C can be seen. Component B is defined as the star which is first moving towards us (blue-shifted). Component C is the star first moving away from us (red-shifted). In the upper left panel the features of Si III are indicated. They are very narrow. The spectral features in the He II line in the same region are very broad. The same effect is noticeable in the upper right and bottom left panel for the narrow Mg II and O II features. Such narrow spectral lines must belong to a different star than the ones showing the broad He/H absorption lines. Do note that in the figures the spectral line indications are not positioned at their rest wavelength. As BAT99 126 is located in the LMC, it is most likely that it moves away from us with approximately the same velocity as the LMC, which is $v_{\mathrm{LMC}} = 262.2$ km/s (Pietrzyński et al., 2013).

The spectra of BAT99 126 thus show four components. Table 7.1 shows all spectral lines which are (clearly) distinguishable in the spectrum. The wavelengths indicated in the table are the rest wavelengths of the atomic transitions in vacuum, obtained from the NIST Atomic Spectra Database[1].

[1] `https://physics.nist.gov/PhysRefData/ASD/lines_form.html`

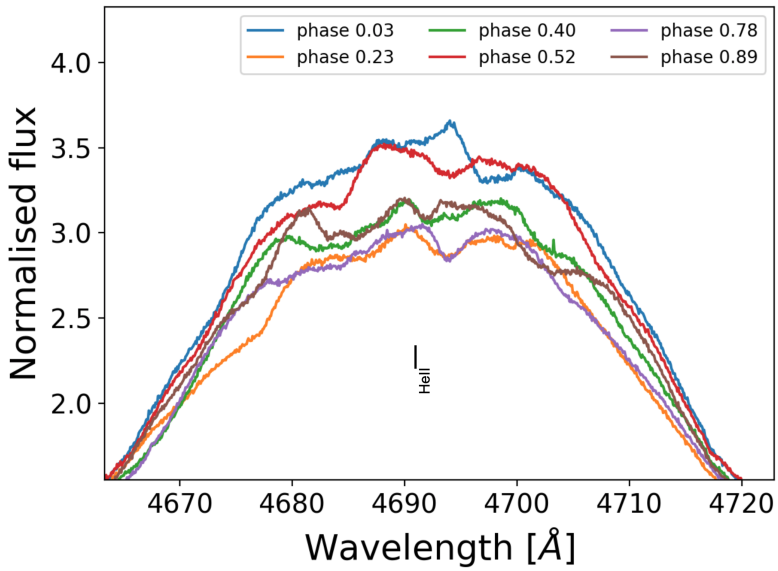

Figure 7.2: The strong He II λ4685.76 line of the WR star. Different colors represent spectra corresponding to different phases of the 1.55-day orbit.

For the WR star, the hydrogen lines (Balmer lines) are blended with nearby He II lines. Certain transitions belonging to He II have wavelengths very similar to the transitions from hydrogen. Shenar et al. (2019) have shown the WR star has a hydrogen abundance of zero.

It is very likely that more spectral lines are present in the system in the sense that not all spectral lines of each component are listed in Table 7.1. Because of the multiplicity of the system some features become too weak to be identified. Especially for component D, which shows to be very weakly present compared to the other components, some spectral lines are too weak to be seen. Question marks in the table represent doubt on the presence of the component in the spectral line. This can be due to the strength of other spectral lines and variability therein. An example is shown in Figure 7.2, showing the top of the strong He II λ4685.76 line of the WR star with clear variability in it. Nonetheless it is not clear which feature should belong to another component.

In order to increase the visibility when showing multiple spectra stacked on top of each other, each spectrum in the images shown in this Section is binned with a factor of 5. This means that instead of plotting every point that is measured, the mean of 5 flux-points is calculated and this is plotted at the average wavelength of the 5 points. The binning of data should be done with caution, as it can weaken the features even further. For the true identification of the spectral lines, binning was not used.

Table 7.1: Spectral lines present in the spectra and their components. Question marks indicate if a contribution is uncertain. Wavelengths of the atomic transitions are the rest wavelengths in vacuum, obtained from the NIST Atomic Spectra Database.

Spectral line		A (WR)	B	C	D
Si III	λ3806.54				x
He I	λ3819.61		?	x	x
O II	λ3911.96				x
O II	λ3945.04				x
O II	λ3954.36				x
Hϵ/He II		x	x	x	?
He II	λ4026.19	x	x	x	x
O II	λ4069/4072.16/4075.86			?	x
Si IV	λ4088.85			x	?
Hδ/He II		x	x	x	?
He I	λ4143.76			?	x
O II	λ4169.22				x
He II	λ4199.86	x	x	x	
Hγ/He II		x	x	x	?
O II	λ4347.42/4351.26			?	x
O II	λ4349.43			?	x
He I	λ4387.93			x	x
O II	λ4414.91/4416.97				x
He I	λ4471.48		x	x	x
Mg II	λ4481.13/4481.33			?	x
He II	λ4541.61	x	x	x	
Si III	λ4552.62/4567.82/4574.76				x
N V	λ4603.73/4619.98	x			
He II	λ4685.76	x	?	?	?
Hβ/He II		x	x	x	x
He I	λ4921.93			x	x
N V	λ4944.56	x			
C IV	λ5801.33/5811.98	x			
He II	λ6406.44	x			
Hα/He II		x	?	?	?
He II	λ6683.26	x			
N IV	$\sim \lambda$7111	x			
He II	λ7177.50	x			
He II	λ8236.51	x			

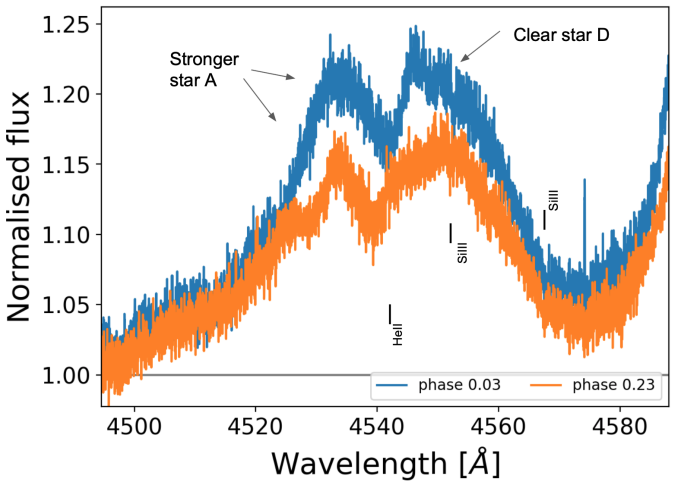

Figure 7.3: Example of a more prominent component A and D when component B and C are eclipsing. The blue spectrum is the one corresponding to $\phi = 0.03$ in the 1.55-day orbit. The orange spectrum corresponds to $\phi = 0.23$ in the 1.55-day orbit.

Two spectra are taken at a time where the spectral lines of component B and C nearly fully overlap, meaning the two stars eclipse each other. It follows that less flux is contributed by component B and C simultaneously, as part of their surface is blocked by the component moving in front. As such, component A and D are more prominent in the spectra where the other components eclipse. A clear example of this effect is shown in Figure 7.3.

7.2 Rotational velocities

Component B, C and D are classified with the help of model spectra in the next Section. From the spectrum it becomes clear that component B and C are much more rapidly rotating than star D. It was shown in Figure 3.5 that rotational broadening affects the spectral lines. If we want to reproduce star B and C with a model, it is clear that rotational broadening needs to be taken into account in order for the model spectrum to fit the spectral lines.

Gray (1973) developed a method of obtaining the rotational velocity by using a Fourier transforming technique. A python script based on his method is used. The method will calculate the Fourier transform of a spectral line, where the first minimum of the resulting curve is thought of as corresponding to the rotational velocity of the star. Examples of the usage of this method can be found in e.g. Simón-Díaz and Herrero (2014). The uncertainty on the derived rotational velocity is determined by the width of the peak. The spectral lines of the components are entangled and for com-

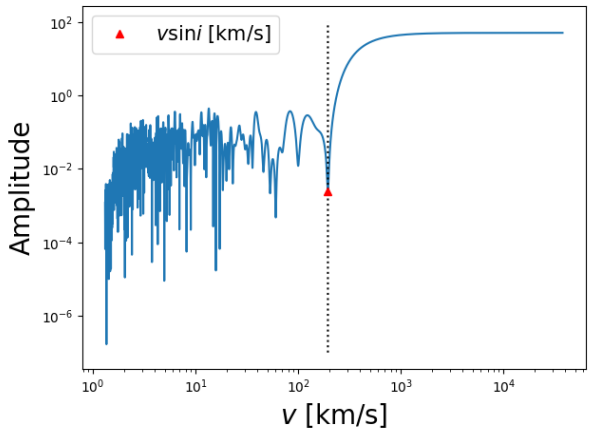

Figure 7.4: Fourier transform of the He I λ4471.48 line of star C. The first minimum or thus the rotational velocity of the star is indicated.

Table 7.2: Rotational velocities of components B, C and D, obtained from performing a Fourier transformation on the spectral lines.

Component	$v_{\rm rot} \sin i$ [km/s]
B	330 ± 40
C	200 ± 30
D	40 ± 10

ponent B and C they are also broadened. Hence, the wings of these spectral lines may be hard to recognise. This is especially the case for components B and C. Therefore, the precision of the rotational velocity is rounded off to be a multiple of 10, but is likely underestimated. The boundaries of the spectral lines of star D can be more precisely established as they are much narrower. Figure 7.4 shows an example of the results obtained using Gray's method on the He I λ4471.48 line of star C. The first minimum is located furthest to the right and represents the rotational velocity of the star. Table 7.2 lists the derived rotational velocities of component B, C and D and their respective uncertainties. For components B and C the He I λ4471.48 line is used in order to avoid that the wings of the spectral lines are lost in the WR emission line. For star D the O II λ4414.91/4416.97 lines are used, such that there is a smaller contribution from components B and C. The rotational velocity that is obtained is not the true rotational velocity, but the projection of the rotational velocity $v_{\rm rot} \sin i$.

We discuss whether these velocities are an indication of synchronous rotation of the components, after we derived the orbits and radii in Section 8.1.2.

Table 7.3: Classification of the WR stars of the nitrogen sequence. Part of the classification table from van der Hucht (2001).

Type	Nitrogen emission lines	Other criteria
WN2	N V weak or absent	He II strong
WN2.5	N V present, N IV absent	
WN3	N IV < N V, N III weak or absent	
WN4	N IV ≃ N V, N III weak or absent	
WN4.5	N IV > N V, N III weak or absent	

Spectral lines used for the classification of WN stars in the spectral range are: He II 4340, He II 4541, He II 4686, He II 4861, He II 6560, N III 4634/4641, N IV 4058, N V λ4603, N V λ4619 and N V λ4933/4944.

7.3 Spectral classification

The spectral lines of the components are identified. They serve as a mean to obtain their spectral type and their effective temperature. This Section will assign a spectral type and/or effective temperature to each component.

7.3.1 The WR star

In Section 7.1, component A was chosen as the WR star. Table 2 of van der Hucht (2001) is used to classify it (partly presented here in Table 7.3). Based on the absence of N III λ4634/4641 and the absence/marginal N IV λ4058 lines, types WN4 and later are excluded. The N V lines are clearly present. The WR star is classified as WN2.5-3 type, in agreement with the previously determined WN3 type of Shenar et al. (2019). As the emission lines of WR stars originate from their winds and not from their stellar surface, their spectral types are not directly coupled to their effective temperature or luminosity.

7.3.2 Components B and C

Components B and C are classified by the use of the non-LTE stellar-atmosphere code TLUSTY (Lanz and Hubeny, 2003). Instead of measuring differences between the relative strengths of spectral lines, model spectra are plotted against the observations. Whilst carefully selecting the model(s) that represent the two components best, special attention is given to the He I λ4471.48 and He II λ4541.61. The relative strength of these spectral lines is a good indicator for the effective temperature, as these lines come from the same atomic transition, only in a different ionisation level. It can

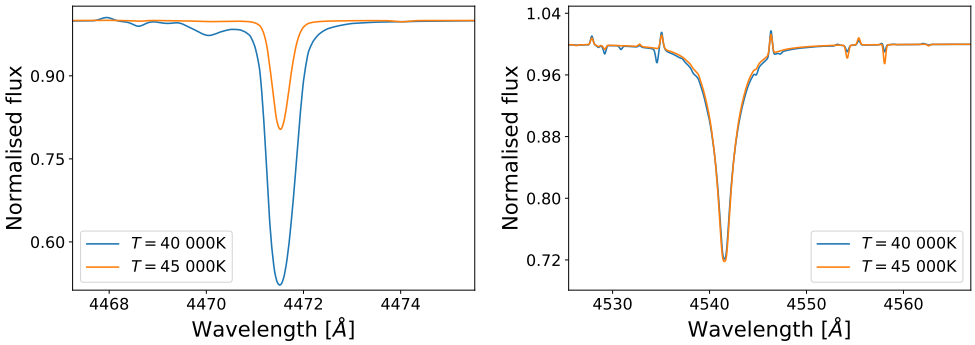

Figure 7.5: The He I λ4471.48 (left) and He II λ4541.61 (right) line for two TLUSTY model spectra with a temperature of 40 000 K (blue) and 45 000 K (orange).

indeed be seen in Figure 7.5 from the TLUSTY model spectra that the relative strength between the two lines is very temperature-sensitive. The strength of the He II 4541.61 line barely changes with effective temperature, whereas the He I 4471.48 is clearly stronger in the cooler model (40 000 K, blue) than in the hotter model (45 000 K, orange).

Moreover, most of the other spectral lines of star B and C are blended with the strong emission lines of the WR star, hence making it difficult to see if models reproduce the other lines well.

The clear presence of He II lines for both of the components indicates both stars are of O-type. The He I lines of star C are stronger than those of star B. For the He II lines it is the other way around. This indicates that star C is cooler than star B.

Also the surface gravity of the two stars needs to be estimated. If star B or C were a supergiant, it would dominate the whole spectrum. As this is not the case, both stars B and C are classified as main-sequence stars or dwarfs (V). Their $\log g$ is estimated to be 4.00 [cm s^{-1}], which is the standard value for main-sequence stars.

A comparison of different models to the observations result in effective temperatures of $T_{\mathrm{eff},1} = 42\ 500 \pm 2\ 500$ K and $T_{\mathrm{eff},2} = 37\ 500 \pm 2\ 500$ K for the first and second O-type star respectively. The uncertainties on the effective temperatures are determined by the grid size of the TLUSTY models, which is 2 500 K. Rotational broadening was applied to the models to derive these temperatures.

For O-type stars in the Galaxy, the corresponding parameters of the spectral type were already calibrated (Martins et al., 2005). However, for O-type stars in the LMC this is not the case. The most general way of classifying a star is according to the equivalent width of certain spectral

Table 7.4: Classification criteria for O-type stars taken from van der Hucht (1996, Table 2). The criteria are based on the ratio of the equivalent width of the He I λ4471.48 and He II λ4541.61 line, here defined on a logarithmic scale.

Subtype	$\log W'$	Subtype	$\log W'$
O3	< -0.90	O7	-0.10 to -0.01
O4	-0.90 to -0.61	O7.5	$+0.00$ to $+0.09$
O5	-0.60 to -0.46	O8	$+0.10$ to $+0.19$
O5.5	-0.45 to -0.31	O8.5	$+0.20$ to $+0.29$
O6	-0.30 to -0.21	O9	$+0.30$ to $+0.44$
O6.5	-0.20 to -0.11	O9.5	$+0.45$ to $+0.65$
		O9.7	$+0.65$ to $+1.00$

lines, which is a measure of the line strength.

The entangled lines make it difficult to obtain the equivalent widths directly from the observations. As the two O-type stars both have a model spectrum assigned, it is possible to obtain an estimate of the spectral types using this model. It is an unusual way of doing so, but it is currently also the only option available. The classification schemes of several studies are combined in van der Hucht (1996). His results are presented in Table 7.4. The classification criterion is based on the ratio of the equivalent width of the He I λ4471.48 and He II λ4541.61 lines. The criteria are given on a logarithmic scale ($\log W'$). The two O-type stars are classified as O4 $^{+1.5}_{-1}$ V and O6.5 $^{+1}_{-1}$ V respectively for the hotter (star B) and cooler (star C) component.

Unless otherwise stated, the two O-type stars will be individually referenced as O_1 and O_2 for the hotter and cooler O-type star respectively.

7.3.3 Component D

The presence of Si III and O II lines combined with the absence of He II lines indicates a rather cool (compared to the other components) B-type massive star. For the classification of star D, the criteria presented by Evans et al. (2015) are used. A reasoning similar to those applied for the two O-type stars results in a classification of star D as a main-sequence star or dwarf (V). Hence the results for B-type dwarfs from Evans et al. (2015) are used (in this report repeated in Table 7.5).

For the classification, the spectrum corresponding to one of the eclipses of the two O-type stars is used, as star D is more prominent here. Figures of the lines used for the classification are shown in Figure 7.6. The spectral-line indicators in each panel are not positioned at their rest wavelength but are shown to indicate clearly where the spectral line is located. Analysis shows that Si III λ4553 and Mg II λ4481 are clearly present. Furthermore,

Table 7.5: Classification of B-type dwarfs in the LMC (Evans et al., 2015).

Type	Criteria
B0	Si IV λ4089 > Si III λ4553 > He II λ4542
B0.2	Si IV λ4089 > Si III λ4553; He II λ4542 marginal
B0.5	He II λ4542 absent; Si III λ4116 marginal/absent
B0.7	He II λ4686 marginal/absent; Si III λ4116 marginal/absent
B1	Si III λ4553 > Si IV λ4089; Si IV λ4116, He II λ4686 absent
B1.5	Si IV λ4089 absent; Si III λ4553 $\sim$ Mg II λ4481
B2	Si III λ4553 < Mg IIλ4481
B2.5	Si III λ4553 absent; Si II $\lambda\lambda$4128-32 marginal

Si III λ4553 $\gtrsim$ Mg II λ4481, making the B-type star of earlier type than B2. An absorption feature of Si IV λ4089 is also present in the spectrum. This feature is much broader than the other two spectral lines. The general shape of the feature indicates that it belongs to one of the O-type components rather than to star D. If star D presents any absorption feature belonging to Si IV λ4089, it is extremely weak. It follows that Si IV λ4089 < Si III λ4553, pointing to the fact that it is of later type than B0. Given the composition of the spectra, it is impossible to distinguish between the minor details of the types between B0 and B2. Therefore the star D is classified as a B1$\pm$1 V.

The B-type star will have a $\log g \approx 4$ [cm s^{-1}], as it is classified as a main-sequence star. Comparing models with this $\log g$ to the observations will result in the determination of the effective temperature. The small rotational broadening derived earlier is applied in order to compare the models with observations. The obtained effective temperature is $T_{\text{eff}} = 25\,000 \pm 3\,000$ K, where the uncertainty is determined by the grid size of the TLUSTY B-type models (1 000 K).

7.4 Radial-velocity determination

From Figure 7.1 it can be clearly seen that stars B and C (or thus the two O-type stars) are moving around in the system. However for the WR star and the B-type star this is less clear. The radial velocities are determined in order to gain insight into the orbital configuration.

Section 7.4.1 describes the methods used for the calculation of the radial velocity, after which Sections 7.4.2-7.4.4 discuss the radial velocity for the WR star (component A), the B-type star (component D) and the two O-type stars (component B and C) respectively.

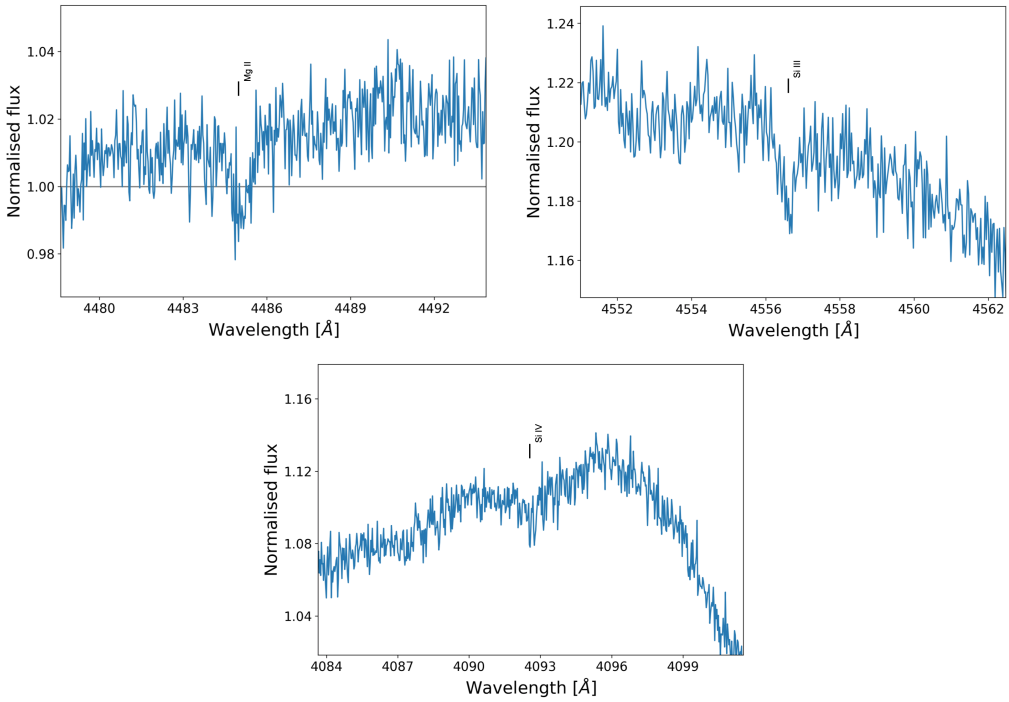

Figure 7.6: The Mg II λ4481, Si III λ4553 and Si IV λ4089 spectral lines used to classify star D. The images are of the spectrum corresponding to one of the eclipses of the two O-type stars (MJD 58437.31, $\phi = 0.03$).

7.4.1 Methods

By measuring the difference between the rest wavelength of a specific atomic transition and the wavelength at which that specific atomic transition is visible in the spectrum - or thus the Doppler shift - the radial velocity (RV) of the star can be obtained at the moment the spectrum was taken. In general, when the star is not rapidly rotating, in contact with another star or the spectral line is not a strong wind emission line, the spectral line is well represented by a narrow Gaussian (see Section 3.4). By fitting a Gaussian to a spectral line, the central wavelength of that spectral line can be determined. The velocity of the star is then calculated by using Doppler's law given in Eq. (3.21).

The method to determine the wavelength shift can differ from star to star and system to system, depending on the behaviour of the spectral lines of the star(s) and whether spectral lines of different components are blended. In this project, two methods were used: the method of cross-correlation (Zucker and Mazeh, 1994; Zucker, 2003; Shenar et al., 2019) and line-profile fitting.

Cross-correlation

The cross-correlation method is used for the components with spectral lines which are not blended with those from other components or for the most prominent component in a blend of spectral lines.

The idea of cross-correlation is that a mask, which serves as a reference frame, is used to determine the velocity shift of an observation with respect to that mask. The mask is a wavelength regime in a template. The template is being shifted over a certain velocity range. For every step the template and spectrum are multiplied. In this way, the cross-correlation function (CCF) is created. Where the CCF peaks the best-fitting RV is identified. An example is shown in Figure 7.7.

The implementation of the cross-correlation method follows Zucker (2003). For the following notations, it is assumed the spectrum is normalised. Using the same notation as Zucker, a point in the spectrum and template are referred to as $f(n)$ and $g(n)$ respectively. The shift of the template is s. Denote the number of bins by N. The CCF is then defined as

$$C(s) = \frac{R(s)}{s_f s_g}, \tag{7.1}$$

with

$$R(s) = \frac{1}{N} \sum_n f(n) g(n - s),$$

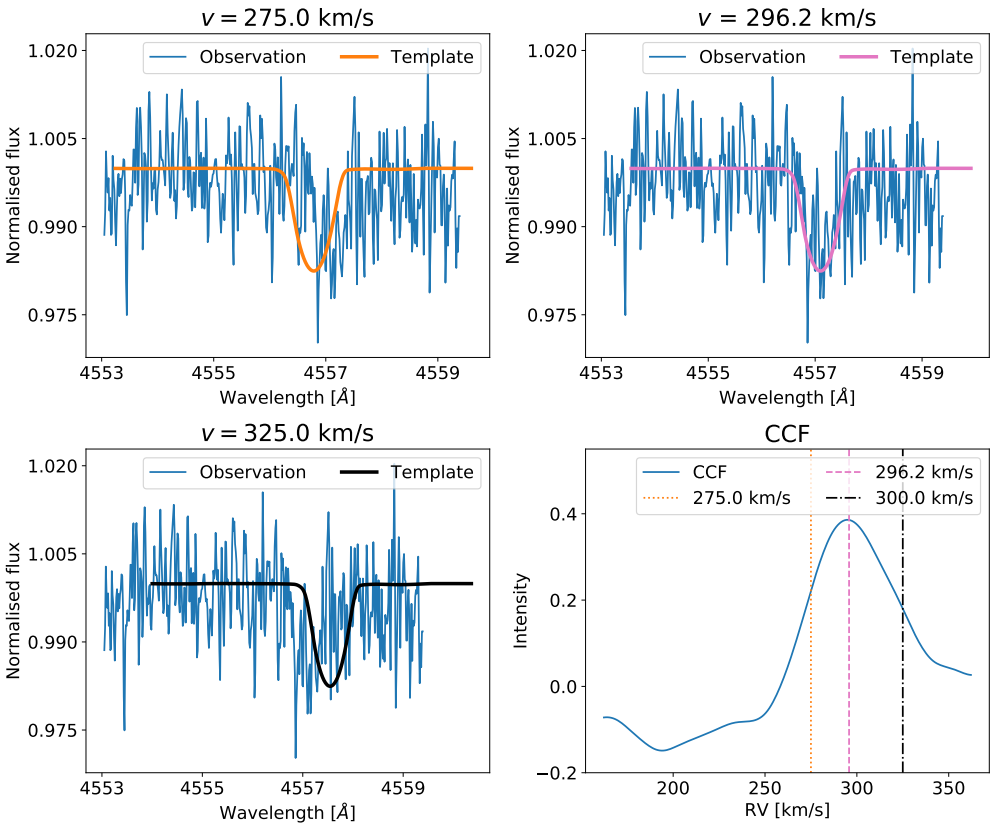

Figure 7.7: The cross-correlation method. The bottom-right panel shows the CCF with three vertical lines in different colors indicated at different velocities. The other panels show the observation and the template shifted according to a certain velocity. Top left: the template at a velocity of 275 km/s, corresponding to the dotted orange line in the bottom-right panel. Bottom left: the template at a velocity of 325 km/s, corresponding to the dot-dashed black line in the bottom-right panel. Top right: the template at the optimal velocity found by the the cross-correlation method (here 269.2 km/s), corresponding to the dashed pink line in the bottom-right panel.

$$s_f^2 = \frac{1}{N}\sum_n f^2(n),$$

$$s_g^2 = \frac{1}{N}\sum_n g^2(n),$$

where s_f and s_g are the standard deviations of the spectrum and the mask respectively and $R(s)$ defines the value of s which maximizes the CCF.

The error on s is given by

$$\sigma_s^2 = -\frac{1}{N}\frac{C(s)}{C''(s)}\frac{1-C^2(s)}{C^2(s)}, \tag{7.2}$$

where $C''(s)$ is the second derivative of the CCF.

In order to find the peak of the CCF, a polynomial fit is performed with the built-in Python function *numpy.polyfit*[2]. The method performs a least-squares n-degree polynomial fit to the data. The least-squares method minimises the sum $S = \sum_{i=0}^{N}(y_i - x_i)^2$ where the sum is over all data points (i) and x and y respectively represent the data and the fit.

Depending on the component on which the method is performed, the mask is either a model or one of the spectra. For components which are not well represented by a model, the mask is one of the spectra itself and thus the RVs that are determined are relative RVs instead of absolute RVs. For components where the model is used as a mask, the RVs are absolute.

In order to increase the S/N of the spectrum template, the different observations are stacked according to their first RVs derived. This also decreases the contribution of other components. As the spectra are coadded according to the RVs of the component in question, the contribution of all other components not moving with the same RVs decreases. Cross-correlation is then repeated with the improved template. An example of a coadded template compared to a spectrum is shown in Figure 7.8.

Line-profile fitting

It is not always preferable to use the cross-correlation method. For example when several lines are entangled, i.e. multiple components show the same spectral line, the cross-correlation method will not always find all components, but only the most prominent features. There is a way to use the cross-correlation method on two components simultaneously (TODCOR: TwO-Dimensional CORrelation, Zucker and Mazeh, 1994), however it is time-consuming to implement it. Therefore another method to determine the RVs is used, namely that of line-profile fitting. This technique uses

[2] `https://docs.scipy.org/doc/numpy/reference/generated/numpy.polyfit.html`

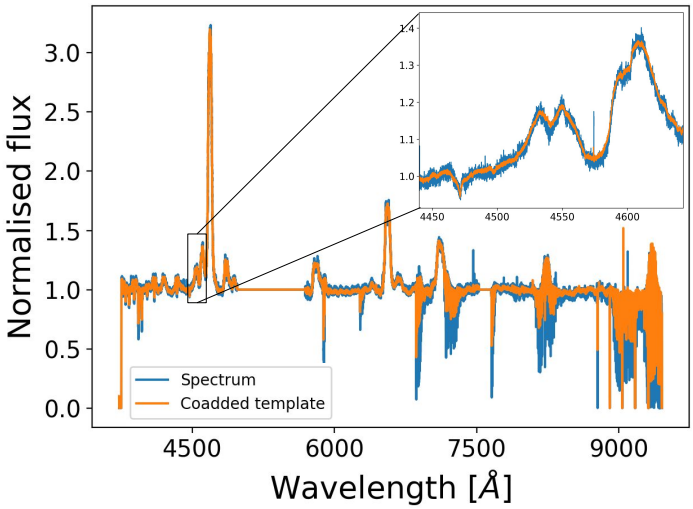

Figure 7.8: Spectrum (blue) and coadded template (orange) used to derive RVs with the cross-correlation method.

Gaussians, related functions, or models fitting them simultaneously to the data. Via an optimisation procedure it finds the best fit to the selected line(s).

The optimisation method used is the same as the one used for the normalisation, namely the built-in function *scipy.optimize.minimize*[3] using the Newton-Raphson method. Other optimisation methods were also considered, however the resulting RVs did not differ significantly from each other.

The most significant influence on the RV determination comes from the choice of initial guesses. This is why only the spectral lines for which good initial guesses can be made are chosen to be fitted.

The errors on the obtained values are calculated by the optimisation method itself. It returns the covariance matrix of the solution, out of which the uncertainties can be obtained from the values on the diagonal.

Using these two techniques, the RVs of all the components are obtained.

7.4.2 The WR star

The WR star shows the very broad emission lines which dominate the spectrum. Therefore, the radial velocities of the WR star are obtained with the cross-correlation method. The spectral lines that are used to determine the RVs of the WR star are given in Table 7.6. The N V/IV and C IV lines are formed rather close to the stellar photosphere, as opposed to He II lines.

[3] `https://docs.scipy.org/doc/scipy/reference/generated/scipy.optimize.minimize.html`

Table 7.6: Spectral lines used to determine the RVs of the WR star. The last column shows some additional remarks about the usage of the spectral lines.

Spectral line		Name in Fig.	Additional comments
N V	λ4603.73	NV4604	Used for creating coadded template
N V	λ4944.56	NV4945	Not used in final results
C IV	λ5801.33/5811.98	CIV5801	
N IV	$\sim \lambda$7111	NIV7111	

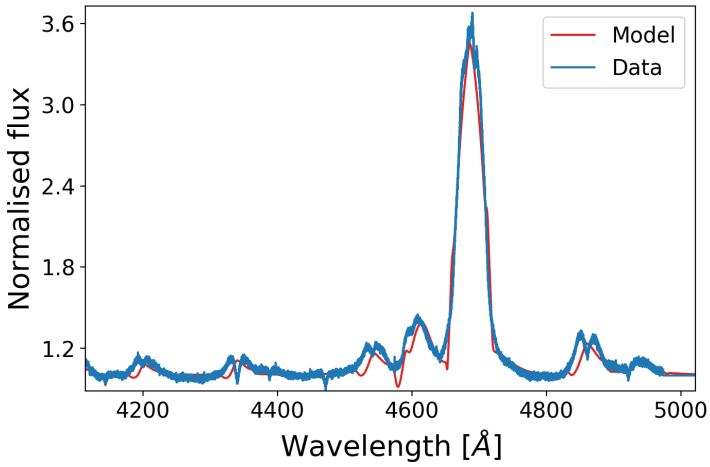

Figure 7.9: Best-fitting PoWR model of the WR star (red) and one of the spectra of BAT99 126 (blue).

The latter are formed over a wide region in the winds. It is commonly believed that the lines of higher ionisation levels are more trustworthy because of this reason. Hence, no lines belonging to the transitions of helium are used. They are subject to variability, of which an example was shown in Figure 7.2. Moreover, they are highly blended with the other components, of which examples are shown in Figure 7.1.

The template used for the radial velocity determination of the WR star is one of the spectra. Although model spectra including the strong winds of WR stars exist (e.g. PoWR, Hamann and Gräfener, 2003), their winds remain very hard to model[4]. An image of the 'best-fitting' PoWR model of the WR star is shown in Figure 7.9 together with one of the spectra. It can be seen that the spectral lines of the model do not match well with the observed spectral lines.

[4]As a wise man once told me: "Models are just models. Sometimes the best model is the star itself." - Dr. T. Shenar.

As explained in the previous section, a coadded template is created by stacking all spectra according to their derived radial velocity. The coadded template is created using the N V λ4603.73 line. It has a very smooth CCF when deriving RVs using a single spectrum. An example is shown in Appendix D in Figure D.1. The derived RVs are then used to shift each spectrum during the coadding procedure.

The RVs derived from the N V λ4944.56 line appeared to deviate from the measurements taken with the other three lines whilst using a single spectrum as the template. A possible reason for this is variability in the winds of the WR star. This would explain the discrepancy between the measurements of the N V λ4944.56 line and the measurements of other three lines. Moreover, the CCFs of the measurements were sometimes not optimal. An example is shown in Appendix D. This could also be caused by the fact that the N V λ4944.56 line is much weaker compared to the other three lines, allowing noise and small features in the vicinity to influence the measurements.

For the reasons mentioned above, the N V λ4944.56 line is not further taken into account for the RV determination of the WR star. More information can be found in Appendix D.

Figure 7.10 shows the obtained RVs for the three spectral lines of the WR star. The template used is the coadded spectrum calculated from the RVs of the N V λ4603.73 line. It can be seen that the data points corresponding to different spectral lines are slightly scattered for most of the observations. We note that the derived value of the RV is not an absolute value and is respective to the coadded template. To calculate the average RV, the mean of the three data points coming from the three different spectral lines is taken. The uncertainty is calculated by taking the standard deviation of these three data points. The average RVs and their uncertainties are plotted in Figure 7.11. Within the uncertainty, a possible slight variation can be detected, however it needs to be taken into account that the uncertainties are most likely underestimated.

Additionally, it was researched whether performing the cross-correlation method on multiple lines at once would alter the results. One would not expect this method to give results very different from the average obtained by the individual line fitting. The values obtained from fitting the N V λ4603.73, C IV λ5801.33/5811.98 and N IV $\sim$ λ7111 were indeed in agreement with the previously obtained values.

A question we try to solve is whether the orbit derived by Foellmi et al. (2003b) can be excluded. The RVs they derived were absolute, i.e. with respect to the rest wavelength of the atomic transitions. The RVs obtained in this work thus need to be calibrated in order to compare them to the radial-velocity curve obtained by Foellmi et al. (2003b). This is done by

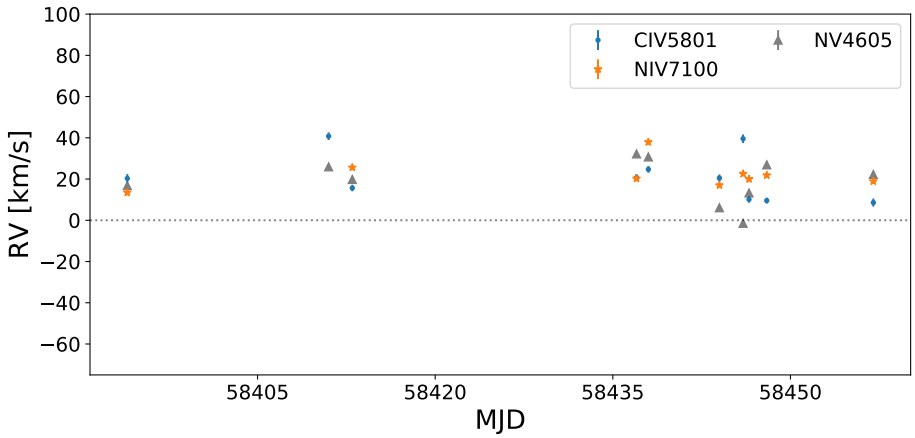

Figure 7.10: RVs for the WR star determined with the coadded template according to the RVs of the N v λ4605 line. Different colors and symbols represent RVs from different spectral lines.

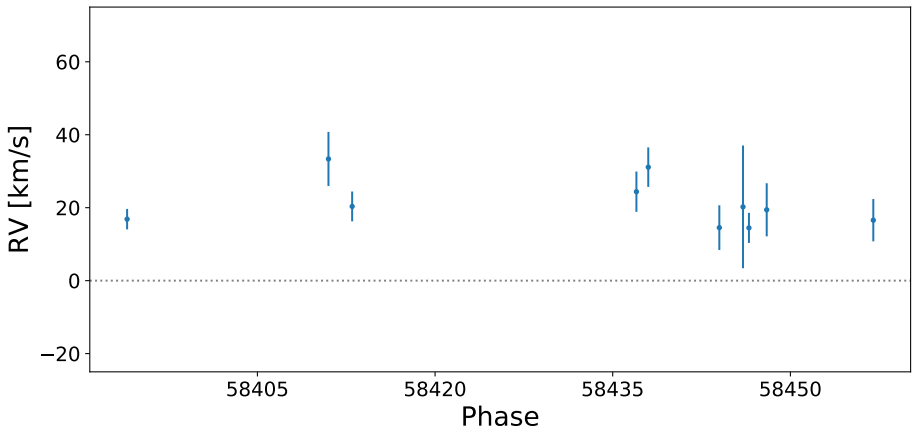

Figure 7.11: Average RVs for the WR star.

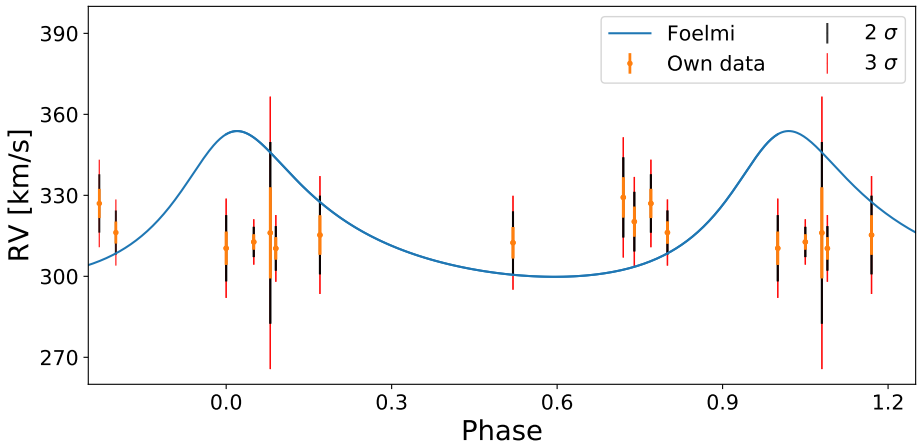

Figure 7.12: The RVs derived for the WR star (orange dots) compared to the 25.5-day orbit derived by Foellmi et al. (2003b) (blue curve). The black and red bars show two times and three times the derived uncertainty on the data points, indicated with 2σ and 3σ respectively.

taking the average of the obtained RVs and calibrating it such that it is equal to the systemic velocity derived by Foellmi et al. (2003b). Figure 7.12 shows the obtained RV data for the WR star plotted in phase of the 25.5-day orbit. The blue curve shows the radial-velocity curve derived by Foellmi et al. (2003b). The black and red bars correspond to two times and three times the derived uncertainty on the data points, indicated with 2σ and 3σ respectively. It can be seen that within 3σ the 25.5-day orbit cannot be reproduced with this data.

7.4.3 The B-type star

The B-type star has very narrow spectral lines, clearly distinguishable from any other spectral lines. Therefore, the RVs of this components are also obtained with cross-correlation. The spectral lines used for determining the RVs of star D are listed in Table 7.7. Although the He I lines belong to the stronger spectral lines of the B-type star, they are not used as they are highly blended with the cooler O-type star, which is also strongly present in these lines.

The spectral lines of the B-type star are much narrower than those of the WR star and are not formed in dense winds. This star is well represented by a model. The RVs are therefore derived with one of the spectra used as a template and using a model as the template. Before actually deriving the RVs, it is noted that most of the chosen lines lie in the wings of the emission lines of the WR star. Because they are so narrow and well separable from the emission line, it is possible to renormalise small parts of the spectra

Table 7.7: Spectral lines used to determine the RVs of the B-type star. The last column shows some additional remarks about the usage of the spectral lines.

Spectral line		Name in Fig.	Additional comments
Si III	λ3806.54	SiIII3807	Renormalised
O II	λ3945.04	OII3954	
O II	λ4069/4072.16/4075.86	OIItriplet4070	Renormalised
O II	λ4347.42/4351.26	OIItriplet4350	Renormalised; Not used in final results
O II	λ4349.43		
O II	λ4414.91/4416.97	OIIdoublet4415	
Si III	λ4552.62	SiIII4553	Renormalised
Si III	λ4567.82	SiIII4567	Renormalised

around the desired spectral line. Renormalising the regions in the spectra is necessary in order to perform cross-correlation with a model. The models are for single stars and hence do not show the broad emission lines of the WR star. Also when using one of the spectra as a template, we want to filter out the variations of the WR star. The renormalisation procedure is done by manually selecting points, following the wings of the WR star. Caution is needed when performing this procedure as in some regions the lines of the B-type star are barely visible and it is easy to accidentally filter them out. The last column of Table 7.7 has a comment on the lines which were renormalised. An example of the five spectral lines before and after renormalisation is given in Figure 7.13, one for each spectrum corresponding to MJD 58437.31.

Using a spectrum as the template was optimal for the WR star, however for the B-type star this has proven not to be the case. As its spectral lines are rather weak they are easily dominated by noise. When using a noisy spectrum as the template and cross-correlating this with another noisy spectrum, the noise will quickly overtake the true RV signal. The CCFs showed this effect when using one of the spectra as a model, as their shapes were distorted from a smooth polynomial. The spectral lines of the WR star are so strong that the cross-correlation method can easily overcome this effect and thus it is not a problem there. If a model is used as a template for the weak lines of the B-type star, the noise in the spectral lines does not dominate anymore as the smooth shape of the model will be the main fitting factor. An example of the difference in CCF when using a spectrum and a model for the B-type star is given in Figure 7.14. Given the unreliable results when using one of the spectra as the template, only the RVs derived with the model template are shown. The RVs that are derived are thus absolute RVs and are not relative to any reference

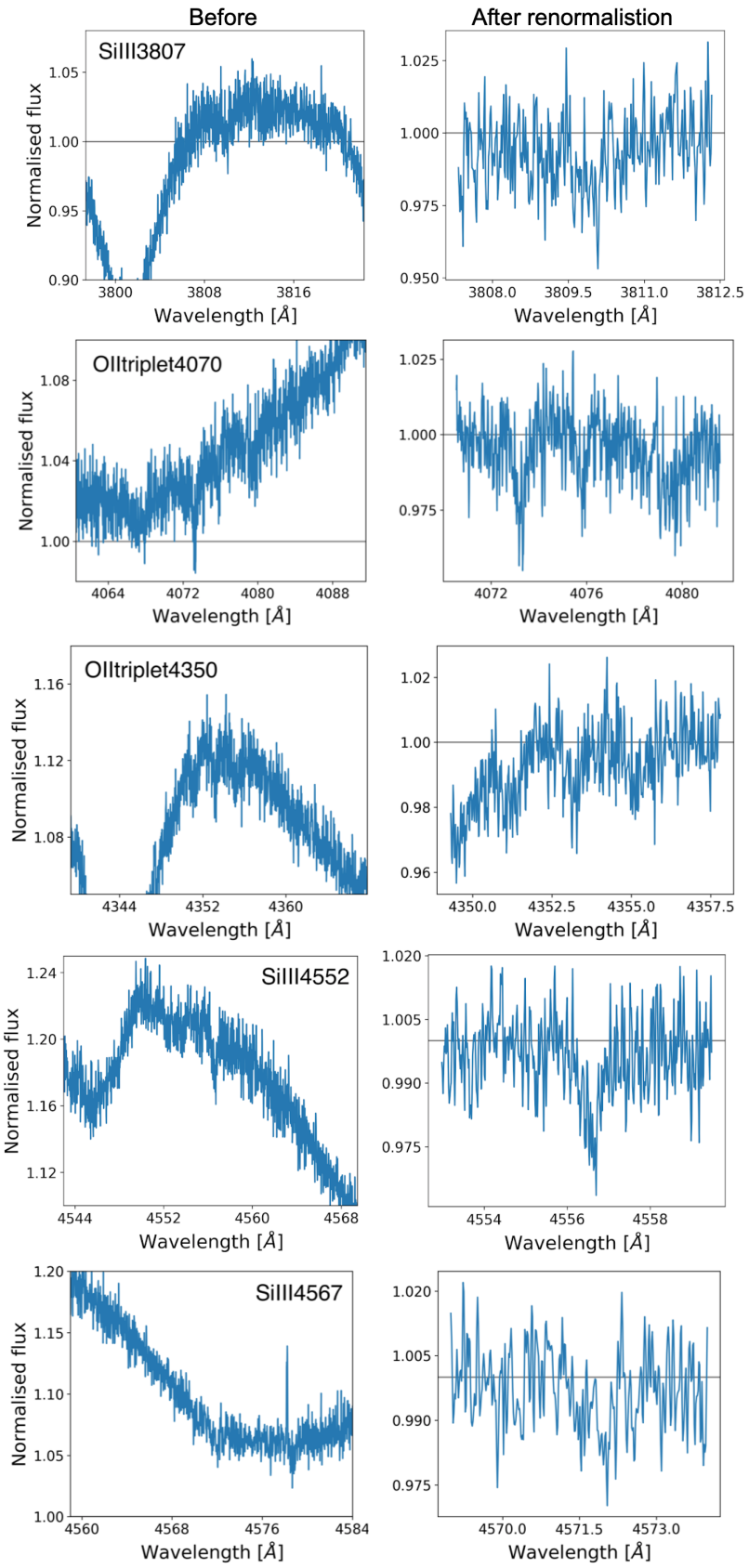

Figure 7.13: Images of the five spectral lines listed in Table 7.7 that were renormalised, before (left) and after (right) renormalisation.

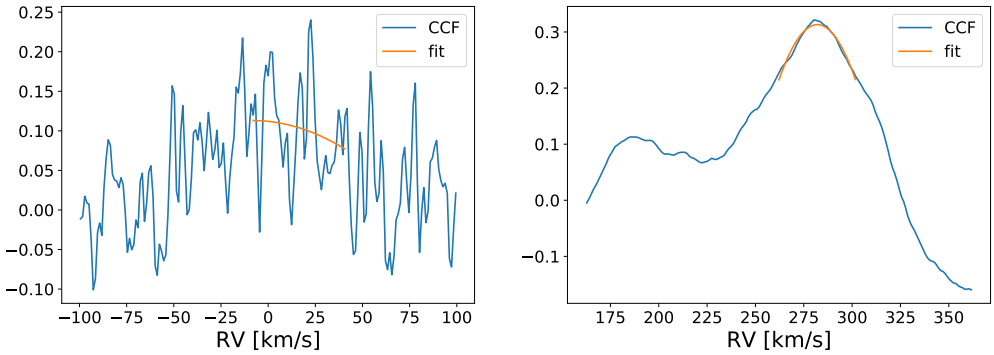

Figure 7.14: The CCF for an RV measurement for the B-type star using one of the spectra as the template (left) and using a model (right). The CCF is for the same spectrum and same spectral line, here MJD 58444.10 and O II λ3945.04. The blue line is the CCF and the orange line is the polynomial fit to the CCF.

observation.

The model that was used is the TLUSTY model with $T_{\text{eff}} = 25\,000$ K and $\log g = 4\,[\text{cm s}^{-2}]$ with an applied rotational velocity of 40 km/s, derived in Section 7.2. The model also needs to be scaled to the amount the B-type star contributes to the spectrum. A contribution of 10% is estimated for the B-type star. This is based on scaling the model to different values for the contribution. A much higher value results in model spectral lines which are too strong. A much lower value means the spectral lines are all barely visible. A more thorough derivation of the contribution is performed in Section 7.5.

The obtained RVs are shown in Figure 7.15 for different spectral lines. Different colors and symbols represent RVs from different spectral lines. The gray solid line in the figure shows the LMC velocity $v_{\text{LMC}} = 262.2$ km/s (Pietrzyński et al., 2013). It can be seen that the measurements corresponding to the O II λ4347.42/4351.26 and O II λ4349.43 are sometimes not in agreement with the obtained RVs from the other spectral lines. In order to understand why this is the case, the spectral lines in the vicinity are analysed. The O II λ4347.42/4351.26 and O II λ4349.43 lines are in the model located in the wings of the Hγ line. This causes the model continuum in this region to deviate from one. The region was renormalised in the observations and thus the continuum is here equal to one. As such, the cross-correlation method in some cases does not find the true optimal solution. Since there are multiple spectral lines which do not show this problem and show good fits, it was chosen not to adjust the model and discard the measurements obtained from the O II λ4347.42/4351.26 and O II λ4349.43 lines (in Tables and Figures referred to as the OIItriplet4350

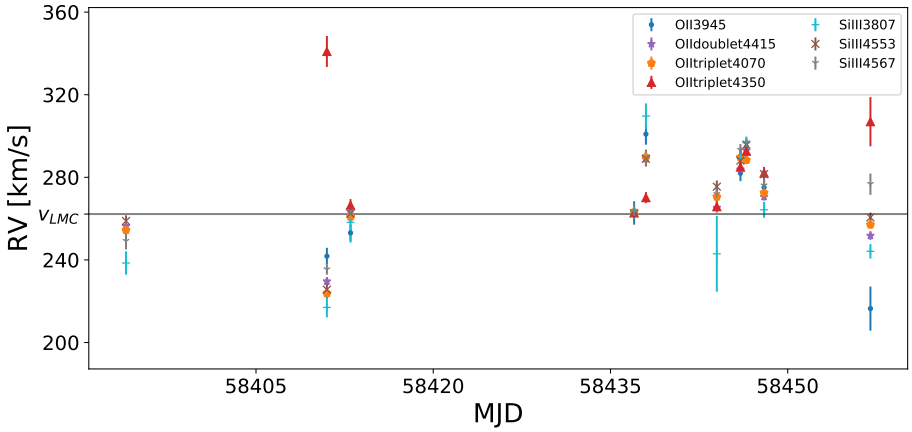

Figure 7.15: RVs for the B-type star obtained with a model template. Different colors and symbols represent RVs from different spectral lines. The RVs are not calibrated. The solid gray line in the figure shows the LMC velocity $v_{\mathrm{LMC}} = 262.2$ km/s (Pietrzyński et al., 2013).

line, see Appendix D).

Figure 7.15 also shows that the RVs measured at MJD 58437.31 are centred around the velocity of the LMC. The measurements are not calibrated to have the same RV anywhere. It appears that all measurements fall around the LMC velocity here.

Figure 7.16 shows the average RVs derived for the B-type star, excluding the measurements for the O II λ4347.42/4351.26 and O II λ4349.43 lines, as explained above. The average RVs and the uncertainties are calculated in the same way as for the WR star. As opposed to the WR star, here the uncertainties do not exclude a small variability in the RVs. The solid gray line shows the LMC velocity $v_{\mathrm{LMC}} = 262.2$ km/s (Pietrzyński et al., 2013).

Before drawing a conclusion on the movement of the B-type star, the spectra showing the two extreme RVs (most negative RV: MJD 58411.23, most positive RV: MJD 58438.22) are compared. This is done in order to see if this motion van be detected by eye. Figure 7.17 shows the spectral lines corresponding to O II λ4069/4072.16/4075.86, O II λ4414.91/4416.97 and Si III λ4552.62 in the two spectra in the different panels. It can be seen that the RV shift in the spectral lines is also detectable by eye. In the discussion at the end of this Chapter (Section 7.6), we discuss the possible implications this has.

WR star + B-type star

The question is now whether the B-type star can be the companion of the WR star. Figure 7.18 shows the obtained RVs of the WR star and B-type

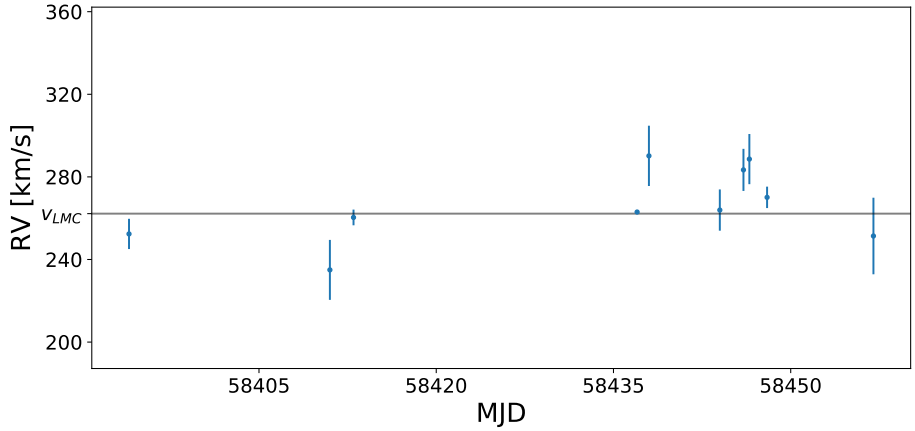

Figure 7.16: Average RVs for the B-type star. The RV measurements derived for the O II λ4347.42/4351.26 and O II λ4349.43 lines are not included in the average. See text for more details. The gray solid line in the figure shows the LMC velocity $v_{\rm LMC}$ = 262.2 km/s (Pietrzyński et al., 2013).

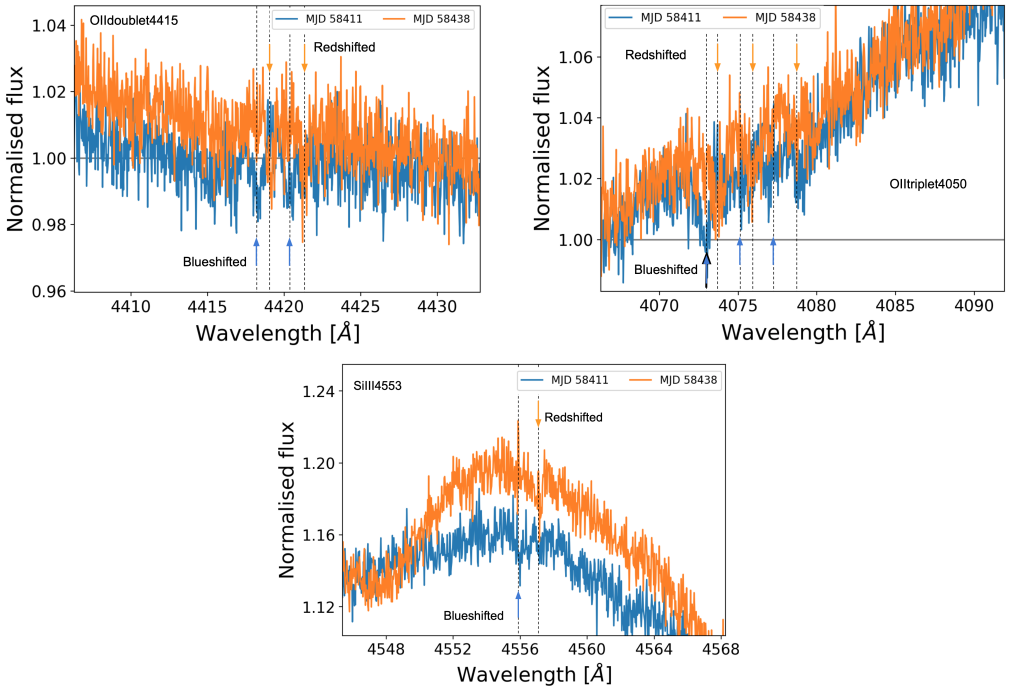

Figure 7.17: Three spectral lines of the B-type component in the spectra taken at MJD 58411.23 (blue) and MJD 58438.22 (orange). The spectral lines are indicated with arrows in the corresponding color of the spectrum.

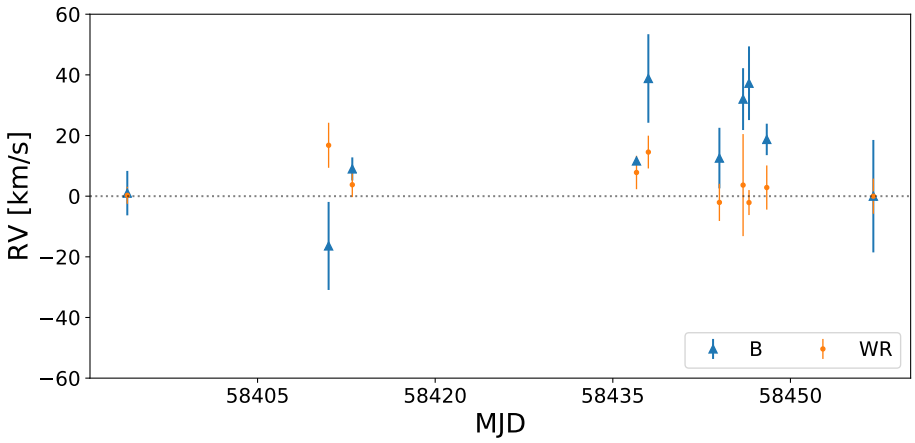

Figure 7.18: The RVs of the WR stars and the B-type star as a function of the time at which the observation was taken. They are scaled such that the RV of the final observation is equal to zero.

star plotted together as a function of the time at which the observation was taken. They are scaled such that the RV of the final observation is equal to zero. The data might suggest an anti-phase motion of the two stars, however given the uncertainties it remains inconclusive whether the two stars are in orbit with each other.

7.4.4 The two O-type stars

The cross-correlation method was not used for these two components as they 1) have almost all spectral lines in common and hence the cross-correlation method cannot distinguish between the two, and 2) they share almost all their spectral lines with the emission lines of the WR star. The latter will dominate for the cross-correlation method.

The RVs of the two O-type components are determined with the technique of line-profile fitting. The spectral lines that are used are listed in Table 7.8. Each spectral line has both components present. As could be seen in Table 7.1, the regions around the spectral lines of the two O-type components also show spectral lines from the other two components. The last column of Table 7.8 repeats which additional components are present in the region of the spectral lines. The line-profile fitting will thus have to be done for multiple components at the same time.

Figure 7.19 and 7.20 show respectively an example of the fits obtained with the line-profile fitting for the He I λ4471.48 and He II λ4541.61 lines. In both Figures, the left panel shows the fit for the spectrum corresponding to a phase $\phi = 0.23$ in the 1.55-day orbit and the right panel corresponds to $\phi = 0.78$ in the 1.55-day orbit. It can be seen that the two O-type stars alternate between bluer and redder wavelengths in anti-phase, indicating

Table 7.8: Spectral lines used to determine the RVs of the two O-type stars. The last column shows some additional components present in the region of the spectral line.

Spectral line		Name in Fig.	Additional components
He I	λ3819.61	HeI3819	B
He II	λ4199.86	HeII4199	WR
He I	λ4471.48	HeI4471	B
He II	λ4541.61	HeII4541	WR

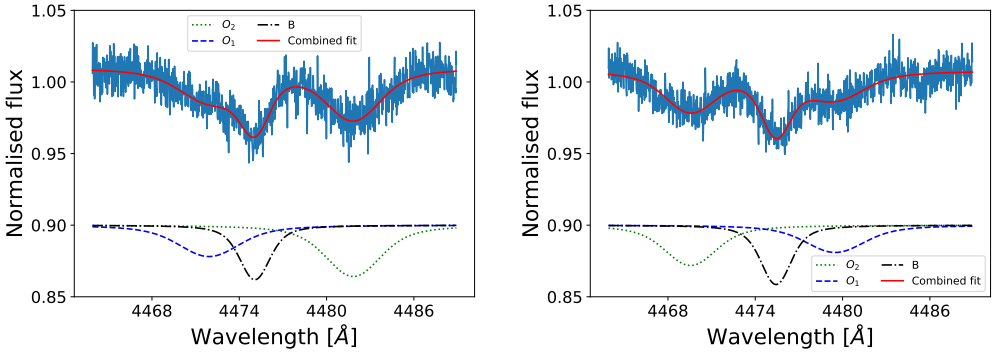

Figure 7.19: Examples of the fits obtained with line-profile fitting on the He I λ4471.48 line. Three components are present: the hottest O-type star O_1 (dash-dotted blue), the coolest O-type star O_2 (dotted green) and the B-type star (dashed black). The combined fit is shown in red on top of the data. Left: for the spectrum corresponding to a phase $\phi = 0.23$ in the 1.55-day orbit. Right: for the spectrum corresponding to a phase $\phi = 0.78$ in the 1.55-day orbit.

they are in orbit with each other.

The obtained radial velocities of the two O-type components are further investigated phase-folded onto the 1.55-day orbit. This is shown in Figure 7.21 for different spectral lines, where different symbols and colors correspond to different spectral lines. For each spectral line, the radial velocities of both components have a different symbol but the same color. For symbols which are not shown the uncertainty could not be derived during the fitting. One of the reasons for this is that during certain phases, the contribution of one of the components can be barely visible. Consequently, the fitting algorithm might not find a corresponding fit of the spectral line. The gray solid line in the figure shows the LMC velocity $v_{\rm LMC} = 262.2$ km/s (Pietrzyński et al., 2013). It is noted that this is not necessarily the systemic velocity of the two components.

The two O-type stars are in anti-phase with each other, indicating they are the components in the 1.55-day orbit. Looking at the overall movement

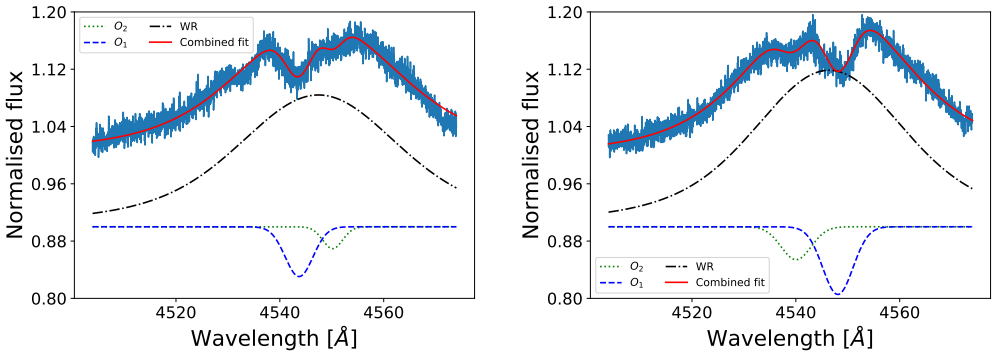

Figure 7.20: Examples of the fits obtained with line-profile fitting on the He I λ4541.61 line. Three components are present: the hottest O-type star O_1 (dash-dotted blue), the coolest O-type star O_2 (dotted green) and the WR star (dashed black). The combined fit is shown in red on top of the data. Left: for the spectrum corresponding to a phase $\phi = 0.23$ in the 1.55-day orbit. Right: for the spectrum corresponding to a phase $\phi = 0.78$ in the 1.55-day orbit.

of the two components, it is expected that the radial velocities at phases $\phi = 0.0$ and $\phi = 0.52$ are around the velocity of the LMC. There are two aspects to notice:

- Not many fits found values for the radial velocities in these observations. This is because at phases $\phi = 0.0$ and $\phi = 0.52$ there is always one of the components which is (almost fully) eclipsed and hence (almost) invisible in the observation. It is thus logical the fitting algorithm only finds (accurate) results for only one of the components. For most of the fits however, the algorithm could not obtain valid uncertainties, most likely due to the stated problem.
- The measured radial velocities are deviating from the expected value. This is again related to the same issue.

Therefore, the radial velocities at phases $\phi = 0.0$ and $\phi = 0.52$ are chosen to be left out in all further calculations.

Figure 7.22 shows the average radial velocities of the two O-type components. As discussed above, the measurements at phases $\phi = 0.0$ and $\phi = 0.52$ are not included in the plot. It is clear the two O-type stars are orbiting around each other and that they produce the 1.55-day signal in the light curve.

7.5 Contributions of the individual components

The contribution of each component to the total flux in the spectrum can be obtained from an analysis of the spectrum. Adding up the model spectra

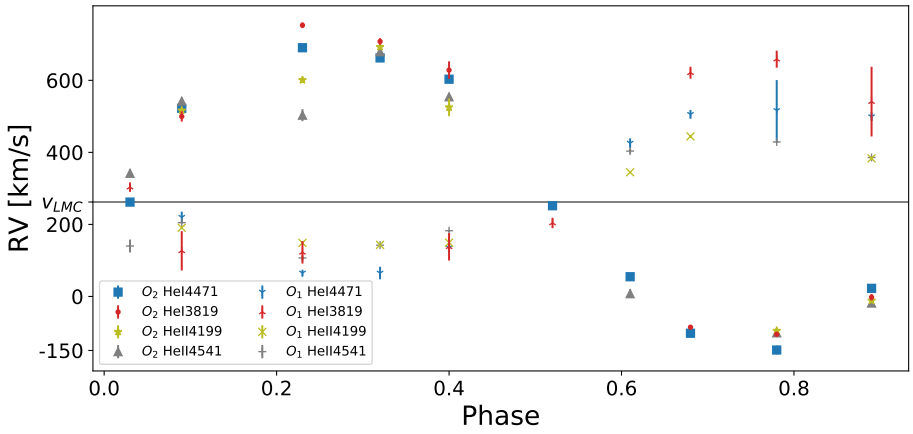

Figure 7.21: Radial velocities obtained for the two O-type stars from different spectral lines as a function of phase in the 1.55 day orbit. For each spectral line, the radial velocities of both components have a different symbol but the same color. For symbols which are not shown the uncertainty could not be derived during the fitting. The gray solid line shows the LMC velocity $v_{\rm LMC} = 262.2$ km/s (Pietrzyński et al., 2013).

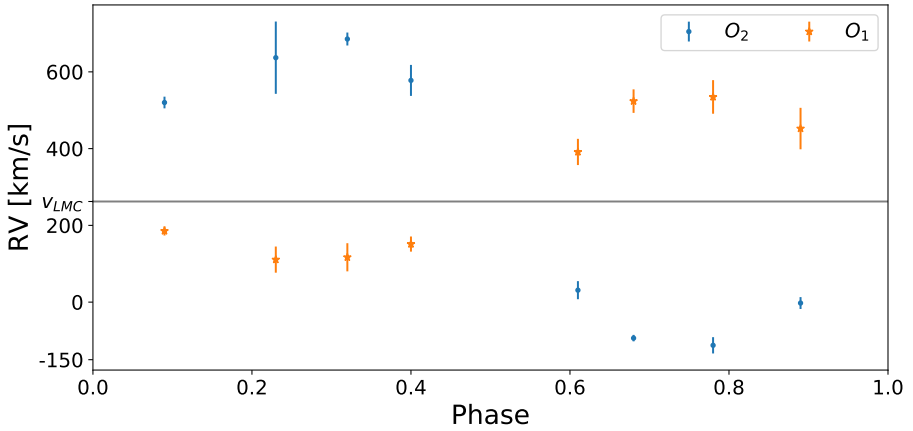

Figure 7.22: Average radial velocities obtained for the two O-type components as a function of phase in the 1.55 day orbit. Blue dots correspond to the cooler component (O_2) and orange stars to the hotter component (O_1). The measurements at phase $\phi = 0.0$ and $\phi = 0.52$ are not included. See text for more details.

Table 7.9: Obtained contributions of the components of BAT99 126 in the spectrum.

	O_1	O_2	WR	B
Contribution [%]	35 ± 5	25 ± 5	30 ± 5	10 ± 1

of all components will result in a model spectrum of the system. Different contributions of the components will result in different strengths of spectral lines.

The two O-type stars and the B-type star have a TLUSTY model spectrum assigned to them after the determination of their spectral type and effective temperatures. For the WR star, the model which is derived by Shenar et al. (2019) is used. They derived wind parameters and luminosities such that the model is customised to best fit this WR star. Nonetheless, it was shown in Figure 7.9 that even this model does not fully reproduce the system. Therefore, the fitting of the contributions is mostly focused on the three other components.

The fitting is done by visual inspection. A more complex fitting procedure is not used because of the WR star. Most of the spectral lines of the two O-type components are located in the broad emission lines of the WR star. As the model does not reproduce these emission lines well, it is difficult to estimate the strength of the true contribution of the two O-type stars here.

One spectral line from which the effect of changing the individual contributions is carefully analysed is the He I 4471.48 line, as the WR star does not contribute here and the three other components are clearly visible. The spectra on which the analysis is performed are the spectra taken at a phase $\phi = 0.23$ and $\phi = 0.78$ in the 1.55-day orbit of the two O-type stars. The two O-type stars and the B-type star can be best seen here. The original models are shifted according to the derived RVs. The models are then scaled to different percentages until a satisfactory fit is found.

The estimated contribution for each component is given in Table 7.9. Figure 7.23 shows the model of each component scaled to the estimated contribution on the He I λ4471.48 line. The solid black curve represents the combined model. The left and right panels show respectively the spectrum corresponding to a phase $\phi = 0.23$ and in $\phi = 0.78$ the 1.55-day orbit. Figure 7.24 shows more examples of the model fits, all for the spectrum corresponding to a phase $\phi = 0.23$ in the 1.55-day orbit. The two top panels show examples where the overall model represents the data well. Both the N V λ4944.58 line of the WR star and the He I λ4143.76 and He I λ4921.93 line of the B-type star model are in good agreement with the observations for the estimated contributions. The two bottom panels show two less good fits. The difficulty here is that the model of the WR star does not represent

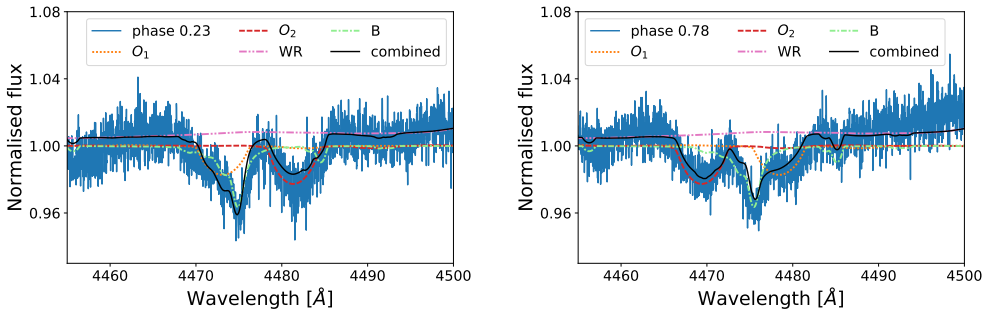

Figure 7.23: Example of the model fits to the spectra on the He I λ4471.48 line. The black line shows the combined model. Left panel: for the spectrum corresponding to a phase $\phi = 0.23$ in the 1.55-day orbit. Right panel: for the spectrum corresponding to a phase $\phi = 0.78$ in the 1.55-day orbit.

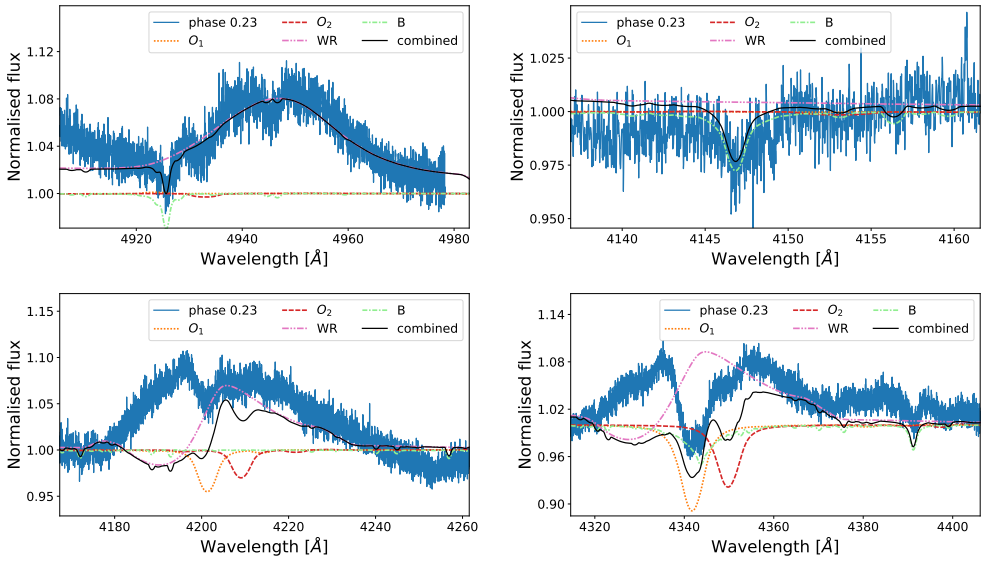

Figure 7.24: Other examples of the model fit to the spectrum corresponding to a phase $\phi = 0.23$ in the 1.55-day orbit. Top panels: good fits. Bottom panels: show how the model for the WR star hinders a precise comparison of the contributions in the spectral lines belonging to He II transitions.

the shape of the observed He II lines well. The combined model will thus also show discrepancies with respect to the observations. Estimating the contributions of the two O-type stars from these lines thus also becomes difficult. This justifies why the main focus of deriving the contributions was on the He I λ4471.48 line.

7.6 Discussion

The system comprises four components: two O-type stars, a WR star and a B-type star. For each component the spectral type was derived. The spectral types of the two O-type stars were derived using the relative line strengths from the model which was chosen to best represent the star. The entanglement of the spectral lines of the two O-type components with the WR star made the process of estimating the correct model temperatures a difficult task. The temperatures are derived from a visual comparison between the spectral lines. As there is no standard model representing the WR star well, it could not be subtracted from the data to improve upon the measurements of the effective temperatures. Although deriving the spectral type from a model is not common, it is currently the only method available. For the WR star and B-type star the spectral type is more robust, as it is based on the relative strengths of the spectral lines in the observations.

The temperatures of the components are derived using spherical symmetry. However, rapidly rotating stars are more oblate and this could alter their spectral line profile (Abdul-Masih et al., 2020). It thus needs to be kept in mind that this gives an extra uncertainty on the obtained effective temperatures.

The uncertainties on the RVs of the WR star are most likely underestimated. One of the reasons is that there are not many spectral lines for which the RVs could be derived and the spectral lines for which the RV was derived showed some variability. Within 3σ the 25.5-day orbit derived by Foellmi et al. (2003b) can be excluded.

The B-type star clearly shows movement in the spectra. There are three options. The B-type star

- orbits the two O-type stars
- is in orbit with WR star
- has a companion which is not detected in the data

The data are inconclusive on the orbital configuration of the WR star and B-type star, such that it is not certain which of the three options is correct.

The orbital motion of the two O-type stars can be clearly seen. Moreover, they are the two stars producing the 1.55-day signal in the LC. Since the minimisation method used can be dependent on the initial guesses that are given, the line-profile fitting was performed multiple times with different initial guesses. For most of the spectral lines that were fitted, the results converged to the same value within errors. The spectral lines for which this did not happen were omitted from the calculations. These were other He II lines, in which the cooler O-type star was barely present, or other He I lines, in which the hotter O-type star was almost not visible.

The complexity of the system makes an estimation of the contributions of the individual components a difficult task. The contributions were estimated by focusing mostly on He I λ4471.48 spectral lines. The contributions are also dependent on the the exact choice of model. A change in the effective temperature of the model also changes the line strengths of the spectral lines, which in turn leads to different contributions. This shows the uncertainty of the estimated contributions.

8 Photometric analysis

This Chapter explains the analysis that is performed on the photometric data. Each method explained in the Chapter also includes results obtained from the spectroscopic analysis. Two analyses are performed with the data: the orbital analysis and calculating the luminosities of the individual components. This Chapter ends with a discussion on the photometric analysis.

8.1 Orbital analysis

Orbital analysis is a precise tool to determine accurate model-independent masses for the components of a binary system. These are important to constrain the evolution of the system and calibrate models.

As mentioned in Chapter 6, the data available of BAT99 126 are photometric and spectroscopic data. The photometric data provides a light curve (LC) and from the spectroscopic data the radial velocities (RVs) have been determined (Section 7.4). For binaries, these two are sufficient to obtain the orbital solution (Section 4.3). It was established in Section 7.4.4 that the two O-type stars produce the 1.55-day signal. The LC of BAT99 126 is used to derive the orbital parameters for these two components.

The software used to model it is discussed in Section 8.1.1, after which Section 8.1.2 discusses the orbital solutions.

8.1.1 PHOEBE

The software used to obtain the orbital solution is the binary modelling code PHOEBE (Prša and Zwitter, 2005). It is both able to calculate synthetic light and radial-velocity curves (LC and RV curve) with estimated values of systemic parameters, as well as to obtain a fit to the provided data by varying these parameters. The parameters included for the fit-

ting are the orbital parameters (Section 4.3) and parameters characterising the components, such as the effective temperatures. Without any initial guesses however, the search for an initial fit can take a very long time or not converge to a fitting solution. It is therefore recommended to provide first estimates for the values of the parameters and, if possible, exclude some parameters which can be easily estimated.

Table 8.1 lists the parameters that are used for the fitting of the photometric and radial-velocity data. It is also indicated which synthetic curve is influenced by which parameters (for the formula of the RV curve, see Eq. (4.2)). For example, the centre-of-mass velocity γ will not influence the shape of the LC. The orbital parameters have been explained in Section 4.1. Additionally, some other parameters which also influence the shape of the LC are listed in Table 8.1. The ones that are newly introduced are explained here and for the others it is explained which values they take:

Surface potentials - Ω_1, Ω_2 Are a measure of the radius of the stars. For each component, there is a critical value below which the star is filling its Roche lobe. The critical value is denoted by $\Omega_{1,2}(L_1)$ which is the value of the potential at L_1.

Synchronicity parameters - F_1, F_2 These parameters determine how fast the stars are rotating compared to the orbital period. A value of one corresponds to synchronous rotation, a value below one to under-synchronous rotation - i.e. the star does not revolve around its axis once a period - and a value above one corresponds to over-synchronous rotation - i.e. the star revolves around its axis faster than it finishes one orbit.

Gravity darkening (Explained in Section 3.5) A value of one corresponds to very effective gravity darkening, a value of zero means no gravity darkening is applied.

Surface albedo When two stars are very close to each other and they have a large surface albedo, they will appear more bright due to the reflection of the light of the other component. In circular systems this effect would just be seen as a general higher luminosity of the total system and deeper eclipses. The values for the surface albedo in PHOEBE range from 0 to 1, where 0 is no reflection.

Luminosity levels - l_1, l_2 Are a measure of the magnitude of the stars. They are dependent on the filter which is chosen and the extinction. Therefore, they do not represent the true luminosity of the star.

Table 8.1: Parameters used for fitting the photometric and radial-velocity data. The last two columns indicate which synthetic curve is affected by each parameter.

Orbital parameter		LC	RV curve
Period	P	×	×
Semi-major axis	a		×
Mass ratio	q		×
Centre-of-mass velocity	γ		×
Inclination	i	×	×
Argument of periastron	ω	×	×
Orbital eccentricity	e	×	×
Other parameters		**LC**	**RV curve**
Surface potentials	Ω_1, Ω_2	×	
Effective temperatures	$T_{\text{eff},1}$, $T_{\text{eff},2}$	×	
Synchronicity parameters	F_1, F_2	×	
Gravity darkening		×	
Surface albedos		×	
Luminosity levels	l_1, l_2	×	
Third light		×	
Metallicities	Z_1, Z_2	×	
Limb darkening		×	

Third light Is a way to tell PHOEBE that another light source is contributing to the light curve. It is given in units of percentage. For example, if one wants to say that another star is in the background, contributing to 50% of the total luminosity of the LC, then the third light takes a value of 0.5.

Fitting procedure and formal errors

The fitting of the RV curve and LC is an iterative procedure. The photometric and radial-velocity data are fitted separately. An adjustment of the inclination obtained by fitting the LC will lead to different best-fit parameters for the RV curve. The reverse is also true: a different inclination obtained from the RV data will result in a different LC fit. This is why parameters that affect both curves are only fitted with one curve. The parameters that were fitted with the RV data are the semi-major axis, the mass ratio and the centre-of-mass velocity. All other parameters are fitted with the LC data.

The fitting procedure implemented in PHOEBE also calculates errors on

the fitted parameters. Some of the errors however do not represent formal errors and parameters such as the masses, which are not directly fitted but calculated by PHOEBE itself, are not explicitly given. The instructions for the determination of the formal errors on the values obtained with PHOEBE are explained in the PHOEBE manual (Prsa and Harmanec, 2010) and are repeated here:

1. First, the inclination is set to 90°. The parameters a, q and v_γ are now fitted by using the RV curve only. The value of a here represents the value of $a \sin i$. We obtained the formal errors on the three parameters: $\sigma_{a \sin i}$, σ_q and σ_{v_γ}. We discard the newly obtained value for a and replace it again with the old value.

2. All parameters except for a, q and v_γ are now fitted with both the LC and RV curve. We do not adopt the correct values, but we use the errors.

3. The formal error on a is calculated as

$$\sigma_a = \frac{\sigma_{a \sin i} + a \cos i \sigma_i}{\sin i}. \tag{8.1}$$

It is important to note that that i and σ_i are originally in degrees and need to be converted into radians (rad = $\pi/180°$).

4. The formal errors on the masses come from error propagation on Kepler's third law for the individual components (Eq. (4.8)). The errors are

$$\begin{aligned} \sigma_{M_1} &= M_1 \left(3\frac{\sigma_a}{a} + 2\frac{\sigma_P}{P} + \frac{\sigma_q}{1+q} \right), \\ \sigma_{M_2} &= M_2 \left(3\frac{\sigma_a}{a} + 2\frac{\sigma_P}{P} + \frac{\sigma_q}{q(1+q)} \right). \end{aligned} \tag{8.2}$$

5. The errors on the radii are given by

$$\sigma_{R_i} = \left| \frac{1}{A_1} \right| \sigma_{\Omega_i} + \left| \frac{A_2}{A_1} \right| \sigma_q + \left| \frac{A_3}{A_1} \right| \sigma_e + \left| \frac{A_4}{A_1} \right| \sigma_F, \tag{8.3}$$

with

$$A_1 = -\frac{1}{R_i^2} - \frac{q(R_i + e - 1)}{[R_i^2 + (1-e)^2 - 2R_i(1-e)]^{3/2}} - \frac{q}{(1-e)^2} + F^2(1+q)R_i,$$

$$A_2 = \frac{1}{[R_i^2 + (1-e)^2 - 2R_i(1-e)]^{1/2}} - \frac{R_i}{(1-e)^2} + \frac{1}{2}F^2 R_i^2,$$

$$A_3 = -\frac{q(R_i + e - 1)}{[R_i^2 + (1-e)^2 - 2R_i(1-e)]^{3/2}} - \frac{2qR_i}{(1-e)^3},$$
$$A_4 = F(1+q)R_i^2. \tag{8.4}$$

8.1.2 Orbital solution

The parameters that were fixed to perform the orbital analysis are given in Table 8.2 with the values they were fixed to. Another software tool called Period04 [1] was used to obtain the period. It calculates the Fourier transform of the LC and returns the most prominent frequencies. Period04 did not manage to obtain any periodic signal. This is most likely because of the gaps in the data and the average time between the data points (Figure 6.6). Therefore, the period $P = 1.552945$ days, published by Graczyk et al. (2011), is used. The HJD0 is obtained by fixing the primary eclipse at a phase $\phi = 0$ and a value of HJD -2 450 000 = 6001.1828 is used. The effective temperature of the hottest O-type star $T_{\text{eff},1}$ is obtained from the spectroscopic analysis and is set equal to 42 500 K. The effective temperature of the coolest O-type star is not fixed in order to obtain a second independent measure of this parameter. Since the eclipses are located at $\phi = 0$ and $\phi = 0.5$, the eccentricity is close to zero. The eccentricity was at first included in the fitting, resulting in a value of $e = 0.006 \pm 0.006$. This is in agreement with a value of zero and hence $e = 0$ is used. As explained in Section 4.3, the argument of periastron ω is now fixed to 90°.

As the two components are estimated to be massive, hot and in such a close orbit, the surface albedo, synchronicity parameter and gravity darkening of both components is fixed to one. Since the two O-type stars have effective temperatures $> 35\,000$ K, the square-root law is used to account for the limb darkening (see Section 3.5).

In Section 7.5 it was obtained that the WR star and the B-type star in total contribute $\sim 35\%$ to the total light of the system. Hence, the value of the third light was fixed to match this value.

We also estimated the effective temperature of the secondary star $T_{\text{eff},2}$ and the mass ratio of the binary q. $T_{\text{eff},2}$ is estimated with the value obtained from the spectroscopic analysis. q is determined by dividing the difference between two outermost radial velocity measures of each component. Rounded, this gives 0.5.

The values of the parameters obtained for the orbital analysis are given in Table 8.3. The hottest O-type star is the more massive star in the binary system and is hence referred to as the primary. The cooler O-type star is referred to as the secondary. The uncertainty on the bolometric

[1] `https://www.univie.ac.at/tops/Period04/`

Table 8.2: Parameters that are fixed for the fitting and their values.

Parameter	Value	Parameter	Value
HJD0	6001.1828	Surface albedos	1
[HJD - 2 450 000]		Gravity brightening	1
P [days]	1.552945	Limb darkening	Square root
$T_{\mathrm{eff},1}$ [K]	42 500	Synchronicity parameters	1
e	0	Third light [%]	35
ω [°]	90		

Table 8.3: Values for the systemic parameters obtained from orbital analysis with PHOEBE. $T_{\mathrm{eff},1}$ was not fitted, but was fixed at 42 500 K and is hence not mentioned in this table.

Parameter	Value	
q	0.41 ± 0.03	
a [$R_\odot$]	20.95 ± 0.67	
i [°]	65.49 ± 0.22	
γ [km/s]	296.15 ± 6.95	
Parameter	Value O_1	Value O_2
M [$M_\odot$]	36 ± 4	15 ± 2
R [$R_\odot$]	9.37 ± 0.09	6.68 ± 0.06
$\log g$ [cm s^{-2}]	4.1 ± 0.9	4.0 ± 0.8
T_{eff} [K]		$38\,000 \pm 2\,000$
Ω	2.76 ± 0.24	2.65 ± 0.57
l	5.55 ± 0.03	2.55 ± 0.03
M_{bol}	$-8.69 \,^{+\,0.34}_{-\,0.39}$	$-7.52 \,^{+\,0.58}_{-\,1.27}$

magnitudes $M_{\mathrm{bol},(1,2)}$ were obtained by setting all other variables to their extremes and allowing PHOEBE to recalculate the value. Figure 8.1 and 8.2 show respectively the obtained synthetic LC and RV curve plotted over the data. The results were not significantly altered when the third light was varied between 30% and 40%.

The obtained mass ratio q is lower than originally estimated. At the phase $\phi \approx 0.23$, the fit tends to an RV of the secondary towards the extreme within the uncertainty. This explains the offset of the estimate. The effective temperature of the secondary $T_{\mathrm{eff},2}$ is in agreement with the value obtained from the spectroscopic analysis.

The $\log g$ values of both stars correspond well with those of main-sequence stars, implying the stars are still burning hydrogen. The critical value of

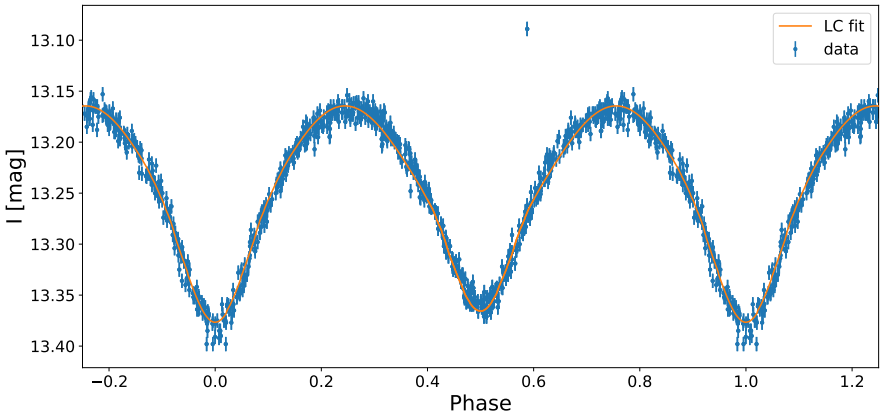

Figure 8.1: The synthetic LC (labeled as 'LC fit') with the data.

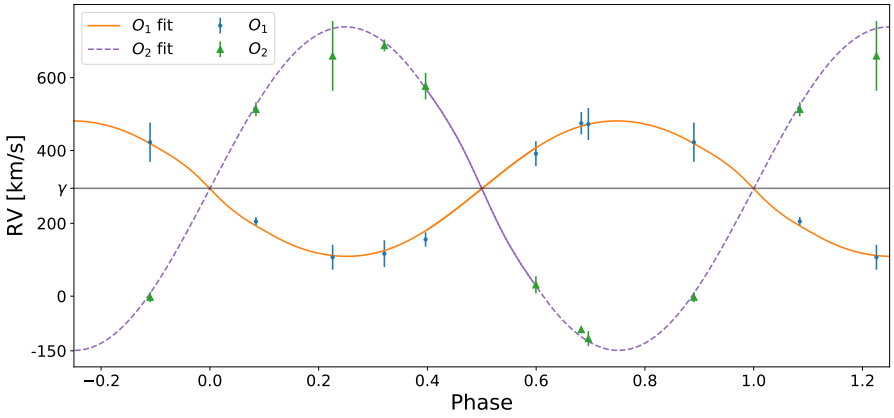

Figure 8.2: The synthetic RV curve with the data. The blue dots and the solid orange curve correspond to the data and RV curve of the primary. The green triangles and dashed purple curve correspond to the data and RV curve of the secondary.

the surface potential for both components is respectively $\Omega_1(L_1) = 2.70$ and $\Omega_2(L_1) = 2.45$. Within the uncertainty, it can not be excluded that one or both stars are filling their Roche lobe.

The luminosity of the two O-type stars can be calculated by using their radii and effective temperatures in Eq. (3.3) and from the bolometric magnitude using Eq. (3.8). The uncertainty on both values can be obtained by using error propagation. The luminosities obtained for both components are:

	L_1 $[10^5 L_\odot]$	L_2 $[10^5 L_\odot]$
From radii and effective temperatures	25.68 ± 6.53	7.92 ± 2.25
From bolometric magnitudes	$30.20 \,^{+\ 0.46}_{-\ 0.53}$	$8.02 \,^{+\ 0.25}_{-\ 0.54}$

or on a logarithmic scale

	L_1 $[\log(L/L_\odot)]$	L_2 $[\log(L/L_\odot)]$
From radii and effective temperatures	5.41 ± 0.13	4.90 ± 0.15
From bolometric magnitudes	5.48 ± 0.01	$4.90 \,^{+\ 0.01}_{-\ 0.03}$

The values obtained with both calculations are in agreement with each other.

Now that we have obtained the radii of the two O-type components, the rotational velocities for a synchronous rotation can be determined. For a synchronous rotation, the rotational period in Eq. (3.6) can be replaced with the orbital period. Table 8.4 shows the rotational velocities obtained from the orbital analysis $v_{\mathrm{rot,oa}}$. As a comparison, the rotational velocities obtained from the spectral lines $v_{\mathrm{rot,sl}}$ are also shown. These velocities were the projected rotational velocities and thus they need to be divided by $\sin i$ in order to compare them. It can be seen that the values obtained from the orbital analysis and the spectral lines do not fully agree with each other for the primary. As mentioned when calculating the rotational velocities from the spectral lines, the lines of the two O-type components are entangled, and the uncertainty is most likely underestimated.

8.2 SED-luminosity calculations

From the orbital analysis we have obtained the luminosities of the two O-type components. The luminosities of the other two stars - the WR star and the B-type component - cannot be obtained in the same way, as no

Table 8.4: Rotational velocities for the two O-type stars obtained from the orbital analysis, assuming synchronous rotation. Last column shows the rotational velocities obtained from the spectral lines (Section 7.2).

Component	$v_{\mathrm{rot,oa}}$ [km/s]	$v_{\mathrm{rot,sl}}$ [km/s]
O_1	294 ± 3	360 ± 50
O_2	209 ± 2	220 ± 30

orbital solution could be established. Another method is used to determine their luminosity.

This new method is explained in Section 8.2.1, after which Section 8.2.2 presents the obtained results.

8.2.1 Method

The luminosity of a star can also be obtained by fitting a model SED to photometric data. For multiple systems the total SED is a combination of the SEDs of the individual components. In order to generate a model SED for such a multiple system, the contribution of each of the components in a certain passband is used to scale the individual models. The contributions are obtained in Section 7.5. These are the contributions in the V-band.

The SED models are generated by the same non-LTE model-atmosphere codes as the spectra, namely PoWR (Hamann and Gräfener, 2003) for the WR and TLUSTY (Lanz and Hubeny, 2003) for the other three components. One caveat to keep in mind when combining PoWR and TLUSTY model SEDs is that they have different units.

The PoWR model SEDs are calculated assuming the star is at a distance of 10 pc and for a given luminosity, meaning that also a radius is assumed. The luminosity was estimated from previous research done by Shenar et al. (2019) and corresponds to $\log(L/L_\odot) = 5.6$. The model is scaled to the distance of the LMC in the following way:

$$F_{\mathrm{PoWR},\, d_{\mathrm{LMC}}} = F_{\mathrm{PoWR}} \left(\frac{10pc}{d_{\mathrm{LMC}}} \right)^2 , \tag{8.5}$$

where $d_{\mathrm{LMC}} = 49.97$ kpc (Pietrzyński et al., 2013). The PoWR models are in units of erg s^{-1} cm^{-2} Å^{-1}.

The TLUSTY models are not scaled to a certain distance and are calculated for a plane-parallel surface, meaning no assumption is made on the radius of the star. The TLUSTY models thus need to be rescaled to the distance of the LMC and a certain radius:

$$F_{\mathrm{TLUSTY},\, d_{\mathrm{LMC}}} = F_{\mathrm{TLUSTY}} \left(\frac{R}{d_{\mathrm{LMC}}} \right)^2 , \tag{8.6}$$

with R the estimated radius of the component. The TLUSTY models are in units of erg s^{-1} cm^{-2} Hz^{-1} and they are converted in units of wavelength (Å). This is done by combining $|F_\lambda \mathrm{d}\lambda| = |F_\nu \mathrm{d}\nu|$ and $\nu = c\lambda$ to obtain

$$F_\lambda = F_\nu \frac{c}{\lambda^2}. \tag{8.7}$$

The way the models are scaled in the V-band is

$$A_x F_x = F_{\mathrm{ref}} \frac{C_x}{C_{\mathrm{ref}}}, \tag{8.8}$$

where the subscript 'x' denotes the component whose flux is scaled, the subscript 'ref' denotes the reference component to which the flux is scaled and 'C' is the contribution in the specific band. A_x in the formula represents the multiplication factor for the flux that needs to be scaled in order for the equality to hold. We denote now the reference star as S_{ref} and additional components with S_{i}. The 'new' luminosities and fluxes of the components become:

$$L_{S_{\mathrm{ref}}} = L_{S_{\mathrm{ref}}} \quad \text{and} \quad F_{S_{\mathrm{ref}}} = F_{S_{\mathrm{ref}}}$$
$$L_{S_i} = A_{S_i} L_{S_i} \quad \text{and} \quad F_{S_i} = A_{S_i} F_{S_i} \quad \text{with} \quad A_{S_i} = \frac{C_{S_i}}{C_{S_{\mathrm{ref}}}} \frac{F_{S_{\mathrm{ref}}}}{F_{S_i}}$$

The total SED of the system is calculated as

$$F_{\mathrm{sys}} = F_{S_{\mathrm{ref}}} + \sum_i F_{S_i}$$

where the sum is over all additional components.

During the whole procedure, the primary O-type star is taken to be the reference star and the additional components are the secondary O-type star, the WR star and the B-type star. Figure 8.3 shows the combined model SED.

The next step is to fit the model SED of the system to the photometric data. As previously mentioned (Section 3.5.1), photometric data is affected by interstellar reddening and this needs to be taken into account for the fit. For an elaboration on how the reddening is treated, the reader is referred to Appendix A and Appendix C lists the photometric observations.

The reddening, and thus the fit, is determined by a χ^2-minimisation of the difference between the observed photometric data and the model SED for different values of the reddening. The χ^2 values are calculated by

$$\chi^2 = \frac{1}{N - D} \sum_{i=1}^{N} \left(\frac{F_{i,\mathrm{obs}} - F_{i,\mathrm{mod}}}{\sigma_{i,\mathrm{obs}}} \right)^2. \tag{8.9}$$

Here, N is the number of data points, D is the number of free parameters, in this case the reddening and the relative extinction parameter, and $\sigma_{i,\mathrm{obs}}$

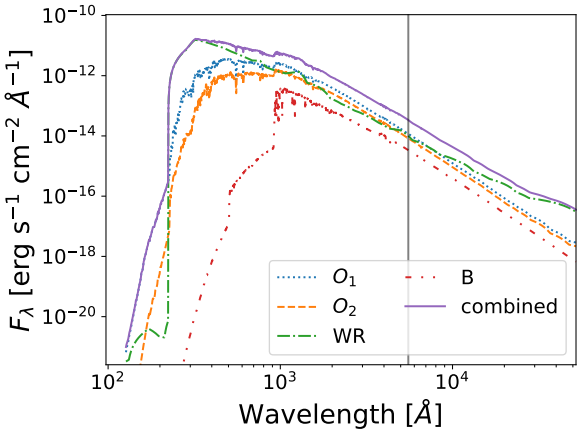

Figure 8.3: The combined SED from the scaled model SEDs of the components. The gray vertical line indicates the V-band wavelength.

is the error on the i-th observed data point. $F_{i,\mathrm{obs}}$ and $F_{i,\mathrm{mod}}$ refer to the i-th point of the observed flux and the corresponding flux value in the reddened model respectively. For every reddening of the model, it is scaled to a certain data point, which is the same at every step. The scaling factor of the step which yields the lowest χ^2 values is used to determine the final luminosities of the components.

In each step the model is thus rescaled, resulting in a different total flux of the system. The individual fluxes and estimated luminosities of the components are multiplied by this scaling factor in order to obtain their true luminosities.

Figure 8.4 shows the difference between the best fit for of the reddening of the model SED and the original combined model SED. The reddened model is a much better representation of the photometric data, which is affected by the interstellar reddening.

Error estimation

The error has two contributions. The first one comes from the error on the fit or thus on the reddening. To determine the error on the reddening value, a Monte Carlo simulation is done. This simulation creates a new data set out of the original observed visual data points, where every new point is created randomly. The relation between the old and new data points is given by

$$F_{V,\mathrm{new}} = F_{V,\mathrm{obs}} + \mathcal{N}(0,1)\sigma_{F_{V,\mathrm{obs}}} \tag{8.10}$$

where $\sigma_{F_{V,\mathrm{obs}}}$ is the error on the observed flux and $\mathcal{N}(0,1)$ represents a random number from a normal distribution with mean value zero and standard deviation one. In total, 1 000 new data sets are created, each of which has

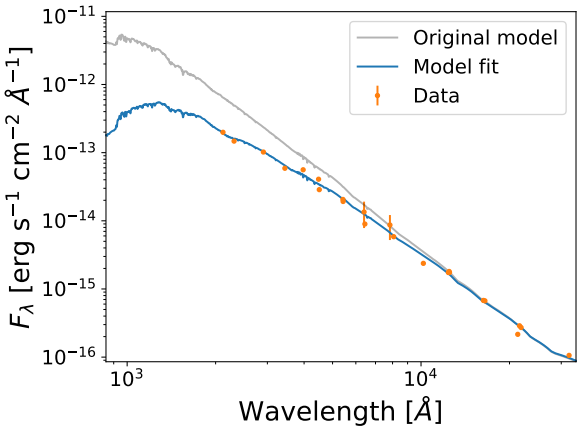

Figure 8.4: Best fit of the reddening of the model SED (blue) compared to the non-reddened model (gray). The photometric data is also shown (orange dots).

its own optimal reddening value, determined in the same way as for the original data.

A second addition to the error comes from the uncertainty on the derived contribution of the components in the spectrum. In order to take this into account, a grid of all possible combinations of contributions within the uncertainty is created, whilst of course making sure the sum of the contribution adds up to 100%. For each of these combinations a model SED is calculated and the fitting procedure is repeated.

8.2.2 Resulting luminosities

Table 8.5 shows the obtained luminosities from the fitting of the model SED. The last column also shows the luminosities that were obtained from the orbital analysis for the two O-type components (Section 8.1.2) and for the WR star the value obtained by Shenar et al. (2019).

The value of the primary O-type star is in agreement with the previously obtained value. The value of the secondary O-type star is in agreement with the previously obtained value if both values are taken close to their extreme value.

Shenar et al. (2019) used the same method to obtain the luminosity of the WR star, but only assumed two components in the system whilst performing the calculations. It is expected that this assumption does not significantly alter the luminosity of the WR star as the assumed second component is a combination of the three individual components. The obtained luminosity of the WR star is indeed in agreement with the value found by Shenar et al. (2019).

Table 8.5: Luminosities obtained from fitting the photometric data with model SEDs. The last column shows the luminosities that were already obtained for the component.

Component	Luminosity [$\log(L/L_\odot)$]	Previous [$\log(L/L_\odot)$]
O_1	5.33 ± 0.11	5.41 ± 0.13 [a]
O_2	5.04 ± 0.13	4.90 ± 0.15 [a]
WR	5.58 ± 0.05	5.61 [b]
B	4.25 ± 0.08	/

a) From the orbital analysis (Section 8.1.2); b) Shenar et al. (2019)

For the B-type component there is no previously found luminosity, since its radius is not known. The obtained luminosity would result in a radius of $R = 7 \pm 3 R_\odot$ when using Eq. (3.3) and the obtained effective temperature $T_{\rm eff} = 25\ 000 \pm 3\ 000$ K.

8.3 Discussion

The effective temperatures of the two components obtained with the spectroscopic analysis and the orbital analysis are in agreement with each other, given that the effective temperature of the primary O-type star is correct. The mass ratio of the system is quite extreme with a value of 0.41. This might indicate that the system is a possible ULX progenitor (see Section 4.5.2). Given the uncertainty on the surface potentials, it cannot be excluded that the close O+O binary in BAT99 126 is a contact system. Further simulations are performed to investigate the evolution of the close binary (Chapter 9).

The luminosities obtained with the SED method are not fully in agreement with the values obtained from the orbital analysis. For the secondary O-type star the luminosity seems to be slightly higher with the SED method. It should be kept in mind that the luminosities obtained with the SED method are based on the uncertain contributions of the components. The results might indicate the contribution of the secondary O-type star is slightly overestimated. The luminosity of the WR star is in agreement with the value obtained by Shenar et al. (2019).

9 Evolution of the system

The massive O+O binary is very close and has an extreme mass ratio. This indicates that the binary could be a candidate progenitor of a ULX or a BH+BH merger. It is therefore important to investigate how this close binary has formed and what its future evolution looks like. Moreover, it could serve as a test laboratory to see whether our understanding of (close-) binary physics is sufficient to explain the evolution of the system.

Shenar et al. (2019) have derived an age estimate of the WR star. They compared evolutionary tracks from the Binary Population and Spectral Synthesis (BPASS) code[1] (Eldridge and Stanway, 2016). Based on the luminosity derived for the WR star, they have obtained the age estimate. As this is based solely on the luminosity and the luminosity of the WR star obtained in this thesis is in agreement with their value, the age estimate of Shenar et al. (2019) can be used for the WR star. This in turn serves as an age estimate of the system, which allows us to perform tailored modelling of the system, and in particular of the close O+O binary. The age estimate is $\tau \approx 4.0 \pm 0.5$ Myr.

We first discuss the possibility of single-star evolution in Section 9.1, after which Section 9.2 explains the simulations that were performed to explore the binary evolution of the system. This Chapter ends with a discussion on the obtained results.

9.1 Single-star evolution

Now that the age of the system is known, the evolution of the close O+O binary can be determined. The first step is to investigate whether the two components of the system could have evolved according to single-star evolution, i.e. with no interactions between the two components during their evolution. The luminosity L and effective temperature T_{eff} of both compo-

[1] bpass.auckland.ac.nz

nents are compared in the HRD against main-sequence tracks for rotating stars from Brott et al. (2011). The current masses, radii, luminosities and effective temperatures are used as input for the online tool BONNSAI[2] (Schneider et al., 2014). BONNSAI, the BONN Stellar Astrophysics Interface, uses Bayesian statistics to compare all available observables simultaneously to stellar models whilst taking observed uncertainties and prior knowledge such as initial mass functions and distributions of stellar rotational velocities into account. The tool returns the age and initial mass of the matching star as well as its luminosity, effective temperature and current mass. Table 9.1 shows the parameters obtained from BONNSAI. There are two things which are important to notice.

- The first thing is the age discrepancy between the two components. The primary O-type star is much younger than the secondary. Given the proximity of the two stars, they most likely formed together. This would imply that if the two stars have evolved as single stars, they have the same age.
- Secondly, the luminosity and effective temperature for the secondary O-type star that are returned by BONNSAI are much lower than the values derived from the data. On top of that the mass is too high, even within uncertainties.

These two findings both point in the direction of a previous phase of mass transfer between the two components. The age discrepancy could originate from the rejuvenation effect of mass transfer on the primary (Mahy et al., 2020). The higher observed luminosity and effective temperature of the secondary could indicate that the secondary is more evolved and originally was more massive. This is reminiscent of the Algol paradox, explained in Section 4.4 and implies that the now secondary less massive star was initially more massive and the now primary more massive star was initially less massive. This is a typical characteristic of an Algol system, as discussed in Section 4.4.

Figure 9.1 shows the main-sequence HR tracks of Brott et al. (2011) for a $36M_{\odot}$- (left) and $15M_{\odot}$- (right) LMC star. The $36M_{\odot}$-star moves through the observed parameters at a young age. The $15M_{\odot}$-star does not move through the observed parameter space at all.

[2] `www.astro.uni-bonn.de/stars/bonnsai`

Table 9.1: Parameters for the two O-type stars. The relevant observed parameters for an evolutionary analysis are shown. Values for single-star evolution are obtained with BONNSAI. Values for the binary evolution are those of the simulation with conservative mass transfer that best fits the values of the observed parameters.

Parameter	Observed		Single		Binary (conservative)	
	O_1	O_2	O_1	O_2	O_1	O_2
$M_{\rm initial}$ $[M_\odot]$			37 ± 4	18 ± 2	23	29
Age [Myr]	4.0 ± 0.5	4.0 ± 0.5	$1.9^{+0.6}_{-0.4}$	$5.3^{+1.8}_{-1.2}$	4.0	4.0
$M_{\rm cur}$ $[M_\odot]$	36 ± 4	15 ± 2	36 ± 4	18 ± 2	32	19
$R_{\rm cur}$ $[R_\odot]$	9.37 ± 0.09	6.68 ± 0.06	$9.38^{+0.08}_{-0.10}$	$6.68^{+0.06}_{-0.06}$	8.75	6.73
$T_{\rm eff,cur}$ [kK]	42.5 ± 2.5	37.5 ± 2.5	$42.1^{+1.7}_{-1.8}$	$31.9^{+2.2}_{-1.5}$	40.7	36.4
$\log(L_{\rm cur}/L_\odot)$	5.41 ± 0.13	5.41 ± 0.13	$5.38^{+0.08}_{-0.06}$	$4.64^{+0.10}_{-0.09}$	5.28	4.85
$P_{\rm initial}$ [days]					1.2	
$P_{\rm cur}$ [days]	1.55				1.44	

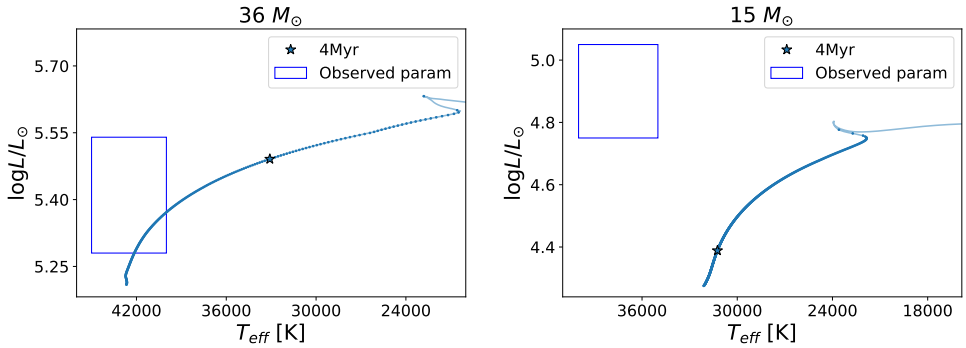

Figure 9.1: Main-sequence tracks for a $36M_\odot$- (left) and $15M_\odot$- (right) LMC star (right) from Brott et al. (2011), with rotational velocities of 329 km/s and 229 km/s respectively. The star symbol indicates an age of 4 Myr. The dots on the track are separated 20 000 years apart. The observed effective temperatures and luminosities of the O-type stars are shown with a blue frame in the corresponding plots.

9.2 Binary simulations

The evolution of the individual O-type stars in the close-binary system cannot be explained by single-star evolution. The evolution of the system will now be simulated with the stellar-evolution code MESA, which stands for Modules for Experiments in Stellar Astrophysics (Paxton et al., 2011, 2013, 2015). MESA is able to perform simulations for both conservative and non-conservative mass transfer using standard theory (Section 4.4). During the rest of this Section, the two O-type stars will be referred to as the donor for the now less massive star and the accretor for the now more massive star.

Below is described how MESA was set up to perform simulations that could reproduce the close 1.55-day-period binary of BAT99 126. A simulation is said to reproduce the system if the simulation parameters match with the observed ones (masses, luminosities, effective temperatures, radii and period). As will become clear, the grid size of simulations is coarse ($\Delta P = 0.1 - 0.5$ days, $\Delta M_{(1,2),i} = 2M_\odot$ and for the non-conservative case $\Delta\beta = 0.1$). Therefore, a discrepancy of 10% is allowed between the parameters returned by the simulation and the observed ones that have uncertainties much smaller than 10%. These are the period and radii.

This Section first introduces the setup of the simulations, followed by testing whether the observed masses and period could also have been the initial conditions (Section 9.2.2). Sections 9.2.3 and 9.2.4 explain simulations performed for conservative and non-conservative mass transfer scenarios. Finally, Section 9.2.5 discusses the future evolution of the system.

9.2.1 General setup

BAT99 126 is located in the LMC, hence has a lower metallicity than the Sun. This is accounted for by including opacity tables for the LMC[3]. These tables allow MESA to perform the simulations with LMC metallicities, without performing expensive opacity calculations in every step. As the metallicity alters stellar parameters it is therefore important to use the correct metallicities.

The simulations are performed for both non-rotating stars and rotating stars. For the rotating stars, the rotational-mixing efficiency is varied. The parameter in MESA accounting for this is `am_D_mix_factor`. Its value is varied from its standard value 0.033 (Heger et al., 2000) up to the extreme values of 20 times the standard value. For sufficiently massive and sufficiently fast-rotating stars, the mixing efficiency will have a critical threshold value above which the rotational mixing leads to homogeneous evolution.

Mass transfer was accounted for by using the model presented by Kolb and Ritter (1990), hereafter named the Kolb model. The Kolb model predicts that Roche-lobe overflow already happens before the star actually fills its Roche lobe. The standard Roche-lobe model only initiates Roche-lobe overflow when the star is actually filling its Roche lobe. This produces a sudden turn-on of mass loss from Roche-lobe overflow. The Kolb model does not have this sudden turn-on but rather has a continuous increase of mass loss. In this sense, the Kolb model is more stable than the standard model.

Non-conservative mass transfer can be accounted for in MESA by varying the parameters $\alpha, \beta, \gamma, \delta$ explained in Section 4.4.2 in the part of non-conservative mass transfer. In MESA these parameters are called `mass_transfer_alpha`, `mass_transfer_beta`, `mass_transfer_delta` and `mass_transfer_gamma`. They have a standard value of zero.

9.2.2 Simulation 0: Initial system parameters

The first simulation that was performed used as initial conditions the masses and period that are observed, i.e. $M_1 = 36M_\odot$, $M_2 = 15M_\odot$ and $P = 1.55$ days. In order to see whether this evolutionary scenario is robust, this simulation was repeated with primary and secondary masses in the range of their uncertainties. This simulation was done for varying rotational-mixing efficiencies or thus different values of `am_D_mix_factor`.

Simulations with a rotational-mixing efficiency of 0.33 or lower did not evolve homogeneously. The end results for all of these simulations are the same: *L2 overflow*. This is a termination code in MESA which means that

[3]https://github.com/orlox/mesa_input_data/tree/master/2016_binary_models

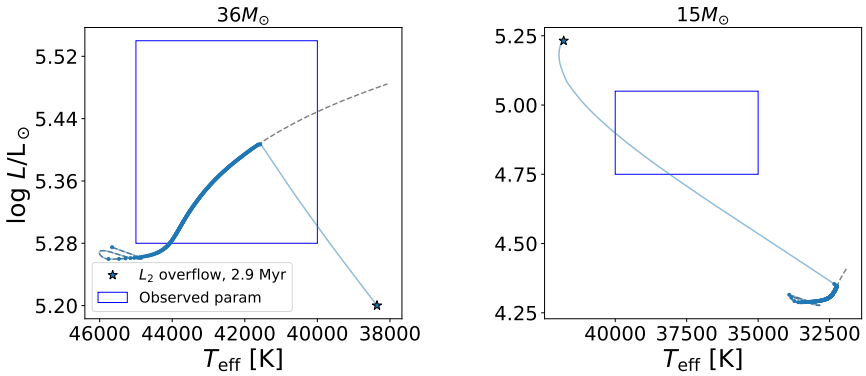

Figure 9.2: Evolutionary tracks for a $36M_\odot$- (left) and $15M_\odot$- star (right) with LMC metallicity, in an orbit of 1.55 days. No rotation is included. The dashed gray line shows the reference to single-star evolution. The star symbol indicates where the simulation stopped because of L_2 overflow, at an age of 2.9 Myr. The dots are positioned every 1 000 years.

mass is flowing out of the system through the second Lagrangian point L_2. The mass that is lost also carries a significant amount of angular moment, causing a rapid decrease in the orbital separation. This phase is unstable, most likely leading to the merger of the two stars.

The following results are for the case in which rotation is not included or equivalently a rotational mixing efficiency of zero. The results for higher rotational mixing efficiencies is qualitatively the same.

Figure 9.2 shows the evolutionary tracks for LMC stars with $36M_\odot$ (left) and $15M_\odot$ (right) in an orbit of 1.55 days. These tracks thus represent the observed configuration of the system in terms of masses and period. The point where the blue binary track deviates from the dashed gray single-star track is where Roche-lobe overflow is initiated. It can be seen that both stars move through the observed parameter space of the luminosity and effective temperature, indicated with the blue rectangle. The dots on the tracks are positioned every 1 000 year, indicating the stars pass through the rectangle rapidly. It is thus very unlikely that we were observing the system in this phase. Moreover, the age of the system at the time the components show the correct luminosity and effective temperature is not in agreement with the estimated age. Furthermore, also the radius of the $15M_\odot$-star at the point where it starts crossing the observed parameter space is already $7.88R_\odot$, which is well outside of the accepted range of values.

For an even more extreme rotational-mixing efficiency of 0.66, the more massive star now evolves homogeneously and mass transfer is not initiated. Part of the evolutionary track is shown in Figure 9.3 up until the age of 6 Myr. The difference between homogeneous evolution and non-

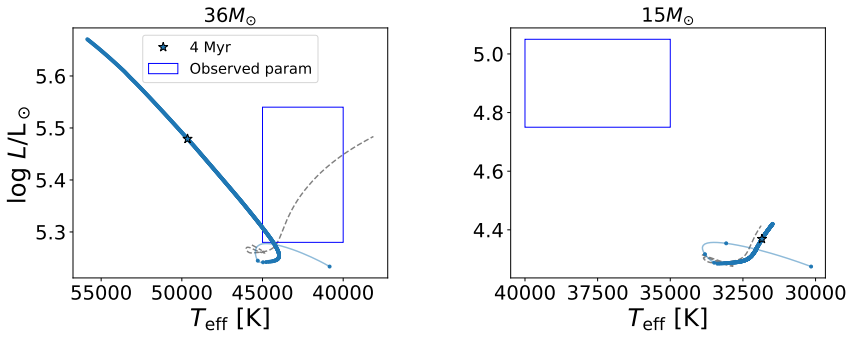

Figure 9.3: Evolutionary tracks for a $36M_\odot$- (left) and $15M_\odot$- star (right) with LMC metallicity and a rotational mixing efficiency of 0.66, in an orbit of 1.55 days. The dashed gray line shows as a reference the evolution of a non-rotating star. The star symbol indicates the estimated age of 4 Myr. The dots are positioned every 10 000 years.

homogeneous evolution is that the star moves to the left in the HRD as its material is constantly mixed. Qualitatively, it can be seen that the results are identical to the scenario of single-star evolution.

The scenario in which the observed values are also the initial conditions of the system is thus excluded as the evolution of the close O+O binary, as is the homogeneous-evolution scenario.

For the following simulations, rotation is excluded.

9.2.3 Simulation set 1: Conservative mass transfer

The first set of simulations was performed by varying the initial masses and periods, assuming the system went through a phase of conservative mass transfer. The difference between these and the previous simulations is that here the initial mass ratio and period are varied significantly compared to the observed values.

For conservative mass transfer, Eq. (4.15) provides the relation between the initial period and masses and the final period and masses of the system. The total initial mass and total final mass of the system are assumed to be identical throughout the calculations and equal to $M_{i,\rm tot} = M_{obs,\rm tot} = M_{1,\rm obs} + M_{2,\rm obs} = 51M_\odot$. The initial masses of the individual components are varied such that their sum matches this initial total mass. The period is then calculated for each of these initial mass combinations.

whilst performing some of the simulations, it became clear that neither masses, period or other parameters resembled the observed ones before the simulations terminated because of L_2-overflow.

A new range of parameters was explored. In order to allow for mass loss

of both components through winds, the total initial mass was set equal to $M_{i,\mathrm{tot}} = M_{obs,\mathrm{tot}} + 1 = 52M_{\odot}$. The value of one for the allowed extra mass is chosen under the assumption that the two stars will lose approximately $1M_{\odot}$ before mass transfer is initiated. Mass transfer itself is kept conservative.

Figure 9.4 shows the evolutionary tracks for a binary with for the two components $M_i = 23M_{\odot}$ and $M_i = 29M_{\odot}$ and an initial period of $P_i = 1.2$ days. Out of all simulations, this was the one which was reproducing the system best. Yet, there are still several problems with matching the observed parameters and the ones returned by the simulations. First, the Figure is explained.

The left panel shows the evolutionary track for the star with an initial mass $M_i = 23M_{\odot}$. This star has at the end of the track a mass $M_f = 36M_{\odot}$. This star thus corresponds to the observed primary star of the system. The right panel shows the evolutionary track for a star with $M_i = 29M_{\odot}$. At the end of the track this star reached a mass of $M_f = 14M_{\odot}$ and thus corresponds to the observed secondary of the close O+O binary. The evolutionary tracks are indicated in gray, where each dot is positioned at a distance of 5 000 years from the previous one. The part of the tracks indicated with orange plus symbols corresponds to the time during the evolution where the radius in the simulation matches within 10% of the observed value ($8.4 - 10.3R_{\odot}$). The blue crosses indicate the same, but for the masses. The '+' symbols and crosses are also positioned every 5 000 years. The observed luminosity and effective temperature are indicated with a blue rectangle. The stars indicate the boundaries between which the age of the star is equal to the estimated age of the system. Between the vertical lines the period of the simulation matches within 10% the observed value (1.40 - 1.70 days). There is only a very small part during the evolution of the initially more massive star for which both the radius and mass agree with the observed values. This is indicated with a pink triangle. In the right plot it is positioned right-hand above the point where the values are matching in order to show the track itself.

It can be seen from the figure that the primary and secondary do not match the observed parameters simultaneously. Although both stars move through the observed range of effective temperature and luminosity at the correct age with the correct period, the mass of the secondary does not agree with the observed values. At the point when the radius and mass of the secondary agree with the observed value, the period of the system does not anymore. A summary of the values of the parameters is given in Table 9.1.

The simulations of conservative mass transfer do not seem to fully agree with the observed values.

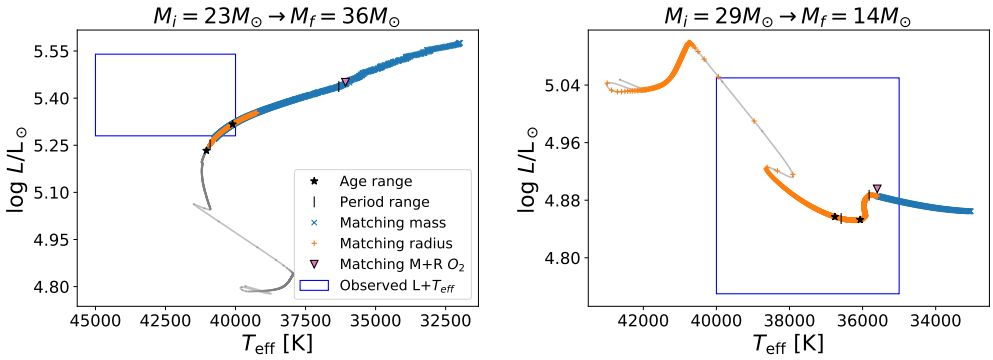

Figure 9.4: Evolutionary tracks for the 'best-fit' simulation of the close O+O binary. The observed luminosity and effective temperature are indicated with the blue rectangle. The evolutionary track is indicated in gray, where the dots are separated at 5 000 years apart. The orange '+' signs correspond to when the star has a radius that is matching with the observed one. The blue crosses represent the same for the mass. Crosses and '+' symbols are also positioned every 5 000 years. The star symbols indicate the boundaries between which the age of the star is matching with the estimated one. Also the range of a matching period is indicated with a vertical line. The left panel shows the now more massive O-type star, the right panel the now less massive O-type star. The pink triangle in both plots indicates where the less massive O-type star has both a matching radius and mass. The initial period of the binary simulation is 1.2 days.

9.2.4 Simulation set 2: Non-conservative mass transfer

Only the β parameter is varied for simulating non-conservative mass transfer. Eq. (4.17) is used to estimate the initial period and masses. Since a significant amount of mass will be lost from the system, the total initial mass of the system will be higher than the observed mass now. This is accounted for when calculating which initial masses and period could result in a simulation which reproduces the system. Simulations were then performed with for varying initial masses and initial periods close to the ones calculated.

Several values for β were explored, ranging from 0.1 to the extreme value of 1, which corresponds to fully non-conservative mass transfer. All simulations performed resulted in L_2-overflow before the observed parameters were matched. Moreover, the values of the parameters obtained from the simulations deviate even more from the observed values than for the previous simulations with conservative mass transfer.

For the most extreme cases, the simulations stopped when the mass ratio was close to unity. An extreme mass ratio as the one observed is not reached as too much mass is lost from the system, causing the orbit to shrink rapidly. Therefore L_2-overflow happens when the mass ratio is still close to unity.

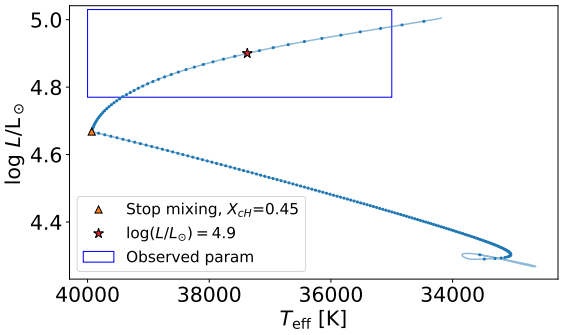

Figure 9.5: Evolutionary track of a $15M_{\odot}$-star with a first phase of homogeneous evolution or extreme mixing up until a hydrogen mass fraction of 0.45 is left in the core (orange triangle). After that, mixing is turned off and the star evolves further. The red star marks the point where the model of the synthetic star is created at $\log(L/L_{\odot}) = 4.9$. The observed luminosity and effective temperature range is indicated with the blue triangle. Blue dots are positioned at a time interval of 100 000 years.

9.2.5 Further evolution of the system

Although no simulation reproduces the close O+O binary, it might be interesting to investigate how the system will evolve further. In order to do this, we create a synthetic $15M_{\odot}$-star which corresponds to the observed luminosity and effective temperature. In order to do this, the stellar interior is artificially mixed up until a certain hydrogen fraction remains in the core. This homogeneous evolution makes the star evolve towards higher luminosities and effective temperatures. The moment mixing is turned off, the star will start evolving towards lower effective temperatures. Depending on when mixing is stopped, the synthetic star will evolve towards different effective temperatures and luminosities.

In order to simulate the first phase of extreme mixing, the mixing parameter `min_D_mix` is set to an extremely high value of `1d10`, which corresponds to 10^5 km/s.[4] When mixing is turned off, `min_D_mix` is set equal to zero. By fine-tuning the moment when mixing is turned off, a synthetic $15M_{\odot}$-star is created with the observed effective temperature and luminosity. The resulting synthetic model is one where mixing is turned off for a central hydrogen fraction of 0.45. Figure 9.5 shows the evolutionary track of the synthetic star. The red star shows the point where the model is created, at a value of $\log(L/L_{\odot}) = 4.9$. Also the radius at the time the model is created, $R = 6.52R_{\odot}$, matches the obtained radius from the orbital analysis. It can be seen that the star needs a long history of mixing in order to obtain the observed luminosity and effective temperature, showing how overluminous the observed $15M_{\odot}$ O-type star is.

[4]As a reference: the radius of the Sun is $\sim 7 \times 10^5$ km.

The next step is to use the synthetic model and put it in a 1.55 day orbit with a $36M_{\odot}$-star. According to the simulations, the $15M_{\odot}$-star is already filling its Roche lobe at the beginning of the simulation. The simulation quickly ends in L_2 overflow.

9.3 Discussion

The O-type components in the close binary did not evolve according to single-star evolution. The younger age for the primary O-type component is probably the rejuvenation effect that is an indication of mass transfer onto the star (Mahy et al., 2020). With these data, both single-star evolution and homogeneous evolution can be ruled out from the evolution of the close O+O binary.

Simulations with non-conservative mass transfer implemented seem to deviate more from the characteristics of the observed system than those with conservative mass transfer. Given the uncertainties and the complexity of the system, the simulations with conservative mass transfer manage to reproduce the system quite well.

It must be kept in mind that the effective temperatures and luminosities are estimated by fitting models onto spectral lines which are highly blended with the spectral lines of the WR star. Moreover, we assumed spherical symmetry of the components whilst deriving the effective temperatures. The faster the star rotates, the more oblate it gets and this might affect the estimation of the effective temperature (Abdul-Masih et al., 2020). As it is difficult to obtain the extremely high effective temperature and luminosity for the secondary O-type component (the least massive one), a possible reason why simulations are unable to fully reproduce the observed close O+O binary is that the effective temperature and luminosity of (at least) the secondary O-type star are overestimated.

The age discrepancy between the two stars will however not be solved with a slight adjustment of the effective temperature or luminosity, such that it remains excluded that the two components of the close O+O binary have evolved as single stars.

10 Conclusions & Outlook

From the high-resolution spectroscopic data of BAT99 126, we conclude that BAT99 126 is a quadruple system. However, the exact configuration of the system is not yet clear. Possibilities include a hierarchical quadruple system or the combination of two SB2 systems. The components are two O-type stars of subtypes O4 $^{+1.5}_{-1}$ V and O6.5 $^{+1}_{-1}$ V, a WR stars of type WN2.5-3 star and a B1 $\pm$ 1 V star.

The O4 V and O6.5 V stars, with masses of $M_1 = 36 \pm 4 M_\odot$ and $M_2 = 15 \pm 2 M_\odot$ respectively, are the components of a 1.55-day-period binary. We find that they have effective temperatures of 42 500 K and 37 500 K, each with an uncertainty of 2 500 K.

The luminosities of the four components are $\log(L/L_\odot) = 5.41 \pm 0.13$, $\log(L/L_\odot) = 4.90 \pm 0.15$ for the hottest and coolest O-type components respectively, and $\log(L/L_\odot) = 5.58 \pm 0.05$ and $\log(L/L_\odot) = 4.25 \pm 0.08$ for the WR star and B-type star respectively.

The previously suggested orbit of 25.5 days (Foellmi et al., 2003b) for the WR star is excluded by analysing the data. Within the uncertainty, no significant motion is detected during the time the data was taken, which is two months.

From the data, it is clear that the B-type star moves. However, no clear orbital motion can be derived within the time period covered by the data. The data are inconclusive on whether the WR star and the B-type star are in orbit with each other. Other possibilities for the B-type star are that it orbits the close O+O binary or that it has another companion, which is not detected with these data.

As no clear orbital motion is detected, it can also not be excluded that the WR star and the B-type star are not bound to the system. However, the possibility that they are stars in the line-of-sight of the close O+O binary is extremely unlikely, and it is even more unlikely that this is the case for both stars.

The age of BAT99 126 is estimated from the WR star, whose age is

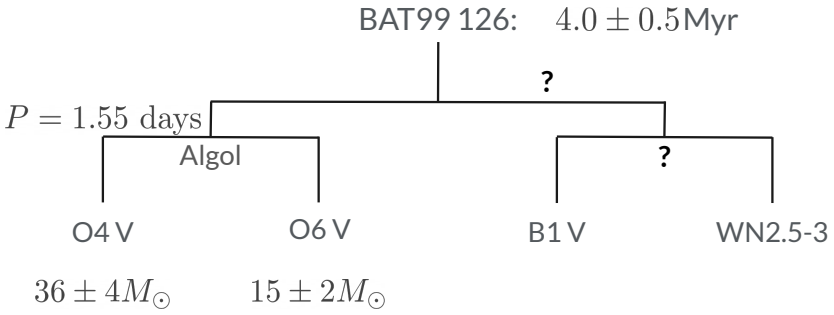

Figure 10.1: Schematic representation of BAT99 126. Question marks indicate that it is uncertain whether the components are bound to each other.

4.0 ± 0.5 Myr. Combining this with the masses and orbital separation of the O+O binary, tailored modelling of the evolution of this binary was performed. From the data, it is excluded that the two O-type components have evolved as single stars. The same goes for homogeneous evolution. We find that the close O+O binary is a high-mass Algol system, where the observed less massive star was originally the more massive star, explained by a previous phase of mass transfer. Binary simulations including both conservative and non-conservative mass transfer were performed, however there was no simulation matching the observed parameters within a 10% uncertainty. This implies that standard mass-transfer physics is not sufficient to reproduce the close binary with the observed parameters. However, it needs to be taken into account that the effective temperatures and luminosities of the components can be overestimated due to the complexity of the system. Since the deviations of the parameters were obtained with the conservative mass-transfer simulations, minor changes in the observed parameters might already be sufficient to account for these minor deviations.

The further evolution of BAT99 126 resulted in an almost immediate L_2-overflow. It could thus not be simulated whether the close O+O binary might evolve towards a ULX or a BH+BH merger. According to the scenarios proposed by Marchant et al. (2016, 2017) the progenitors of ULXs and BH mergers should evolve homogeneously. The simulations thus exclude this scenario. This is however not the only scenario that would lead to BH merger events. Due to uncertainties, the evolution towards a ULX or BH merger cannot be excluded.

Figure 10.1 shows a schematic representation of the configuration of BAT99 126. All four components are indicated, including the uncertainty on the orbital configuration regarding the WR star and the B-type star.

10.1 Outlook

The complexity of the system did not allow for a quick spectral disentangling of the system. However, this is planned to be performed in future work. This might increase the trustworthiness of the obtained effective temperatures and spectral types. However, the results are not expected to be extremely different. The factor that will be the hardest to implement here is the WR star.

If disentangling results in the same luminosities and effective temperatures it might be possible to include other elements in the evolutionary calculations. An option would be to allow for a disk to form around the system, which could interact with the components.

In order to resolve the components of BAT99 126, we applied for more data with the MUSE unit mounted on the Very Large Telescope in Chile. MUSE obtains a 3D cube of the field of view, which allows for a derivation of the spectrum at each pixel. This observation will bring certainty on the orbital configuration of the system. It will also give an extra measurement on the RVs of the WR star and B-type component. Moreover, this observation will be taken with a time difference of about 2 year compared to the UVES data. The derived RV will provide further constraints on the orbital configuration of the system.

The future spectral disentangling will give more certainty on the contributions of the components to the total light and their effective temperatures. With the new data we will be able to constrain the orbital configuration of the system, possibly revealing the component of the B-type star. This will bring us one step closer to unraveling the true nature of this complex system and constraining further close-binary interaction physics.

Bibliography

J. Abadie, B. P. Abbott, R. Abbott, Other collaborators, LIGO Scientific Collaboration, and Virgo Collaboration. TOPICAL REVIEW: Predictions for the rates of compact binary coalescences observable by ground-based gravitational-wave detectors. *Classical and Quantum Gravity*, 27 (17):173001, Sept. 2010. doi: 10.1088/0264-9381/27/17/173001.

B. P. Abbott, R. Abbott, T. D. Abbott, O. LIGO Scientific Collaboration, and VIRGO Collaboration. GW151226: Observation of Gravitational Waves from a 22-Solar-Mass Binary Black Hole Coalescence. *Physical Review Letters*, 2016a.

B. P. Abbott, R. Abbott, T. D. Abbott, Other collaborators, LIGO Scientific Collaboration, and Virgo Collaboration. Astrophysical Implications of the Binary Black-hole Merger GW150914. *The Astrophysical Journal Letters*, 2016b.

B. P. Abbott, R. Abbott, T. D. Abbott, Other collaborators, and S. South Africa/MeerKAT. Multi-messenger Observations of a Binary Neutron Star Merger. *The Astrophysical Journal Letters*, 848(2):L12, Oct. 2017. doi: 10.3847/2041-8213/aa91c9.

M. Abdul-Masih, H. Sana, J. Sundqvist, L. Mahy, A. Menon, L. A. Almeida, A. De Koter, S. E. de Mink, S. Justham, N. Langer, J. Puls, T. Shenar, and F. Tramper. Clues on the Origin and Evolution of Massive Contact Binaries: Atmosphere Analysis of VFTS 352. *Astrophysical Journal*, 880(2):115, Aug. 2019. doi: 10.3847/1538-4357/ab24d4.

M. Abdul-Masih, H. Sana, K. E. Conroy, J. Sundqvist, A. Prša, A. Kochoska, and J. Puls. Spectroscopic patch model for massive stars using PHOEBE II and FASTWIND. *Astronomy & Astrophysics*, 636:A59, Apr. 2020. doi: 10.1051/0004-6361/201937341.

C. Aerts. Stellar Structure and Evolution. Lecture notes for a KULeuven MSc course, 2019.

E. J. Aldoretta, S. M. Caballero-Nieves, D. R. Gies, E. P. Nelan, D. J. Wallace, W. I. Hartkopf, T. J. Henry, W. C. Jao, J. Maíz Apellániz, B. D. Mason, A. F. J. Moffat, R. P. Norris, N. D. Richardson, and S. J. Williams. The Multiplicity of Massive Stars: a High Angular Resolution Survey With the Guidance Sensor. *The Astronomical Journal*, 149(1): 26, Jan. 2015. doi: 10.1088/0004-6256/149/1/26.

P. Bartzakos, A. F. J. Moffat, and V. S. Niemela. Magellanic Cloud WC/WO Wolf-Rayet stars - I. Binary frequency and Roche lobe overflow formation. *Monthly Notices of the Royal Astronomical Society*, 324(1): 18–32, June 2001. doi: 10.1046/j.1365-8711.2001.04126.x.

A. Z. Bonanos, D. L. Massa, M. Sewilo, D. J. Lennon, N. Panagia, L. J. Smith, M. Meixner, B. L. Babler, S. Bracker, M. R. Meade, K. D. Gordon, J. L. Hora, R. Indebetouw, and B. A. Whitney. Spitzer SAGE Infrared Photometry of Massive Stars in the Large Magellanic Cloud. *The Astronomical Journal*, 138(4):1003–1021, Oct. 2009. doi: 10.1088/0004-6256/138/4/1003.

J. C. Bouret, T. Lanz, D. J. Hillier, S. R. Heap, I. Hubeny, D. J. Lennon, L. J. Smith, and C. J. Evans. Quantitative Spectroscopy of O Stars at Low Metallicity: O Dwarfs in NGC 346. *Astrophysical Journal*, 595(2): 1182–1205, Oct. 2003. doi: 10.1086/377368.

F. Bresolin, P. A. Crowther, and J. Puls. *Massive Stars as Cosmic Engines*, volume 250 of *IAU Symposium*. June 2008.

J. Breysacher, M. Azzopardi, and G. Testor. The fourth catalogue of Population I Wolf-Rayet stars in the Large Magellanic Cloud. *Astronomy and Astrophysics Supplement*, 137:117–145, May 1999. doi: 10.1051/aas:1999240.

I. Brott, S. E. de Mink, M. Cantiello, N. Langer, A. de Koter, C. J. Evans, I. Hunter, C. Trundle, and J. S. Vink. Rotating massive main-sequence stars. I. Grids of evolutionary models and isochrones. *Astronomy & Astrophysics*, 530:A115, June 2011. doi: 10.1051/0004-6361/201016113.

R. Burnham. *Burnham's celestial handbook. an observers guide to the universe beyond the solar system*, volume 445. 1978.

J. I. Castor, D. C. Abbott, and R. I. Klein. Radiation-driven winds in Of stars. *Astrophysical Journal*, 195:157–174, Jan. 1975. doi: 10.1086/153315.

R. Chini, V. H. Hoffmeister, A. Nasseri, O. Stahl, and H. Zinnecker. A spectroscopic survey on the multiplicity of high-mass stars. *Monthly*

Notices of the Royal Astronomical Society, 424(3):1925–1929, Aug. 2012. doi: 10.1111/j.1365-2966.2012.21317.x.

M. R. L. Cioni, G. Clementini, L. Girardi, R. Guand alini, M. Gullieuszik, B. Miszalski, M. I. Moretti, V. Ripepi, S. Rubele, G. Bagheri, K. Bekki, N. Cross, W. J. G. de Blok, R. de Grijs, J. P. Emerson, C. J. Evans, B. Gibson, E. Gonzales-Solares, M. A. T. Groenewegen, M. Irwin, V. D. Ivanov, J. Lewis, M. Marconi, J. B. Marquette, C. Mastropietro, B. Moore, R. Napiwotzki, T. Naylor, J. M. Oliveira, M. Read, E. Sutorius, J. T. van Loon, M. I. Wilkinson, and P. R. Wood. The VMC survey. I. Strategy and first data. *Astronomy & Astrophysics*, 527:A116, Mar. 2011. doi: 10.1051/0004-6361/201016137.

P. S. Conti, P. A. Crowther, and C. Leitherer. *From Luminous Hot Stars to Starburst Galaxies*. 2008.

P. A. Crowther. Physical Properties of Wolf-Rayet Stars. *Annual Review of Astronomy and Astrophysics*, 45(1):177–219, Sept. 2007. doi: 10.1146/annurev.astro.45.051806.110615.

P. A. Crowther and L. J. Hadfield. Reduced Wolf-Rayet line luminosities at low metallicity. *Astronomy & Astrophysics*, 449(2):711–722, Apr. 2006. doi: 10.1051/0004-6361:20054298.

R. M. Cutri and et al. VizieR Online Data Catalog: WISE All-Sky Data Release (Cutri+ 2012). *VizieR Online Data Catalog*, art. II/311, Apr. 2012.

S. E. de Mink and I. Mandel. The chemically homogeneous evolutionary channel for binary black hole mergers: rates and properties of gravitational-wave events detectable by advanced LIGO. *Monthly Notices of the Royal Astronomical Society*, 460(4):3545–3553, Aug. 2016. doi: 10.1093/mnras/stw1219.

S. E. de Mink, O. R. Pols, and R. W. Hilditch. Efficiency of mass transfer in massive close binaries. Tests from double-lined eclipsing binaries in the SMC. *Astronomy & Astrophysics*, 467(3):1181–1196, June 2007. doi: 10.1051/0004-6361:20067007.

S. E. de Mink, M. Cantiello, N. Langer, O. R. Pols, I. Brott, and S. C. Yoon. Rotational mixing in massive binaries. Detached short-period systems. *Astronomy & Astrophysics*, 497(1):243–253, Apr. 2009. doi: 10.1051/0004-6361/200811439.

H. Dekker, S. D'Odorico, A. Kaufer, B. Delabre, and H. Kotzlowski. Design, construction, and performance of UVES, the echelle spectrograph for the UT2 Kueyen Telescope at the ESO Paranal Observatory. In M. Iye and

A. F. Moorwood, editors, *Proc. SPIE*, volume 4008 of *Society of Photo-Optical Instrumentation Engineers (SPIE) Conference Series*, pages 534–545, Aug. 2000. doi: 10.1117/12.395512.

R. G. Detmers, N. Langer, P. Podsiadlowski, and R. G. Izzard. Gamma-ray bursts from tidally spun-up Wolf-Rayet stars? *Astronomy & Astrophysics*, 484(3):831–839, June 2008. doi: 10.1051/0004-6361:200809371.

J. Diaz-Cordoves and A. Gimenez. A new nonlinear approximation to the limb-darkening of hot stars. *Astronomy & Astrophysics*, 259(1):227–231, June 1992.

J. Diaz-Cordoves, A. Claret, and A. Gimenez. Linear and non-linear limb-darkening coefficients for LTE model atmospheres. *Astronomy and Astrophysics Supplement*, 110:329, Apr. 1995.

P. P. Eggleton. Aproximations to the radii of Roche lobes. *Astrophysical Journal*, 1983a.

P. P. Eggleton. Towards consistency in simple prescriptions for stellar convection. *Monthly Notices of the Royal Astronomical Society*, 1983b.

Z. Eker, V. Bakış, S. Bilir, F. Soydugan, I. Steer, E. Soydugan, H. Bakış, F. Aliçavuş, G. Aslan, and M. Alpsoy. Interrelated main-sequence mass-luminosity, mass-radius, and mass-effective temperature relations. *Monthly Notices of the Royal Astronomical Society*, 479(4):5491–5511, Oct. 2018. doi: 10.1093/mnras/sty1834.

J. J. Eldridge and E. R. Stanway. BPASS predictions for binary black hole mergers. *Monthly Notices of the Royal Astronomical Society*, 462 (3):3302–3313, Nov. 2016. doi: 10.1093/mnras/stw1772.

C. J. Evans, M. B. Kennedy, P. L. Dufton, I. D. Howarth, N. R. Walborn, N. Markova, J. S. Clark, S. E. de Mink, A. de Koter, P. R. Dunstall, V. Hénault-Brunet, J. Maíz Apellániz, C. M. McEvoy, H. Sana, S. Simón-Díaz, W. D. Taylor, and J. S. Vink. The VLT-FLAMES Tarantula Survey. XVIII. Classifications and radial velocities of the B-type stars. *Astronomy & Astrophysics*, 574:A13, Feb. 2015. doi: 10.1051/0004-6361/201424414.

T. Eversberg, S. Lépine, and A. F. J. Moffat. Outmoving Clumps in the Wind of the Hot O Supergiant ζ Puppis. *Astrophysical Journal*, 494(2): 799–805, Feb. 1998. doi: 10.1086/305218.

E. L. Fitzpatrick. Correcting for the Effects of Interstellar Extinction. *Publications of the Astronomical Society of the Pacific*, 111(755):63–75, Jan. 1999. doi: 10.1086/316293.

C. Foellmi, A. F. J. Moffat, and M. A. Guerrero. Wolf-Rayet binaries in the Magellanic Clouds and implications for massive-star evolution - I. Small Magellanic Cloud. *Monthly Notices of the Royal Astronomical Society*, 2003a.

C. Foellmi, A. F. J. Moffat, and M. A. Guerrero. Wolf-Rayet binaries in the Magellanic Clouds and implications for massive-star evolution - II. Large Magellanic Cloud. *Monthly Notices of the Royal Astronomical Society*, 2003b.

D. B. Friend and D. C. Abbott. The Theory of Radiatively Driven Stellar Winds. III. Wind Models with Finite Disk Correction and Rotation. *Astrophysical Journal*, 311:701, Dec. 1986. doi: 10.1086/164809.

D. Graczyk, I. Soszyński, R. Poleski, G. Pietrzyński, A. Udalski, M. K. Szymański, M. Kubiak, Ł. Wyrzykowski, and K. Ulaczyk. The Optical Gravitational Lensing Experiment. The OGLE-III Catalog of Variable Stars. XII. Eclipsing Binary Stars in the Large Magellanic Cloud. *Acta Astronomica*, 61(2):103–122, June 2011.

D. F. Gray. On the Existence of Classical Microturbulence. *Astrophysical Journal*, 184:461–472, Sept. 1973. doi: 10.1086/152344.

N. J. Grin, O. H. Ramírez-Agudelo, A. de Koter, H. Sana, J. Puls, I. Brott, P. A. Crowther, P. L. Dufton, C. J. Evans, G. Gräfener, A. Herrero, N. Langer, D. J. Lennon, J. T. van Loon, N. Markova, S. E. de Mink, F. Najarro, F. R. N. Schneider, W. D. Taylor, F. Tramper, J. S. Vink, and N. R. Walborn. The VLT-FLAMES Tarantula Survey. XXV. Surface nitrogen abundances of O-type giants and supergiants. *Astronomy & Astrophysics*, 600:A82, Apr. 2017. doi: 10.1051/0004-6361/201629225.

W. R. Hamann and G. Gräfener. A temperature correction method for expanding atmospheres. *Astronomy & Astrophysics*, 410:993–1000, Nov. 2003. doi: 10.1051/0004-6361:20031308.

T. M. Heckman, L. Armus, and G. K. Miley. On the Nature and Implications of Starburst-driven Galactic Superwinds. *The Astrophysical Journal Supplement Series*, 74:833, Dec. 1990. doi: 10.1086/191522.

A. Heger, N. Langer, and S. E. Woosley. Presupernova Evolution of Rotating Massive Stars. I. Numerical Method and Evolution of the Internal Stellar Structure. *Astrophysical Journal*, 528(1):368–396, Jan. 2000. doi: 10.1086/308158.

R. W. Hilditch. *An Introduction to Close Binary Stars*. 2001.

D. J. Hillier and D. L. Miller. The Treatment of Non-LTE Line Blanketing

in Spherically Expanding Outflows. *Astrophysical Journal*, 496(1):407–427, Mar. 1998. doi: 10.1086/305350.

M. Hogerheijde. *The molecular environment of low-mass protostars*. PhD thesis, Department of Astronomy, University of California, Campbell Hall, Berkeley, CA 94720, USA, June 1998.

P. F. Hopkins. Galaxies on FIRE: Stellar Feedback Explains Inefficient Star Formation. In *American Astronomical Society Meeting Abstracts #224*, volume 224 of *American Astronomical Society Meeting Abstracts*, page 215.06, June 2014.

I. D. Howarth. LMC and galactic extinction. *Monthly Notices of the Royal Astronomical Society*, 203:301–304, Apr. 1983. doi: 10.1093/mnras/203.2.301.

R. M. Humphreys. Massive stars in galaxies. *Publications of the Astronomical Society of the Pacific*, 99:5–14, Jan. 1987. doi: 10.1086/131948.

I. Hunter, I. Brott, D. J. Lennon, N. Langer, P. L. Dufton, C. Trundle, S. J. Smartt, A. de Koter, C. J. Evans, and R. S. I. Ryans. The VLT FLAMES Survey of Massive Stars: Rotation and Nitrogen Enrichment as the Key to Understanding Massive Star Evolution. *The Astrophysical Journal Letters*, 676(1):L29, Mar. 2008. doi: 10.1086/587436.

I. Hunter, I. Brott, N. Langer, D. J. Lennon, P. L. Dufton, I. D. Howarth, R. S. I. Ryans, C. Trundle, C. J. Evans, A. de Koter, and S. J. Smartt. The VLT-FLAMES survey of massive stars: constraints on stellar evolution from the chemical compositions of rapidly rotating Galactic and Magellanic Cloud B-type stars. *Astronomy & Astrophysics*, 496(3):841–853, Mar. 2009. doi: 10.1051/0004-6361/200809925.

P. Kaaret, H. Feng, and T. P. Roberts. Ultraluminous X-Ray Sources. *Annual Review of Astronomy and Astrophysics*, 55(1):303–341, Aug. 2017. doi: 10.1146/annurev-astro-091916-055259.

I. D. Karachentsev, V. E. Karachentseva, W. K. Huchtmeier, and D. I. Makarov. A Catalog of Neighboring Galaxies. *The Astronomical Journal*, 127(4):2031–2068, Apr. 2004. doi: 10.1086/382905.

D. Kato, C. Nagashima, T. Nagayama, M. Kurita, J. F. Koerwer, T. Kawai, T. Yamamuro, T. Zenno, S. Nishiyama, D. Baba, R. Kadowaki, Y. Haba, H. Hatano, H. Shimizu, M. Nishimura, T. Nagata, S. Sato, Y. Murai, T. Kawazu, Y. Nakajima, H. Nakaya, R. Kandori, N. Kusakabe, A. Ishihara, N. Kaneyasu, J. Hashimoto, M. Tamura, T. Tanabé, Y. Ita, N. Matsunaga, Y. Nakada, K. Sugitani, K.-I. Wakamatsu, I. S. Glass, M. W. Feast, J. W. Menzies, P. A. Whitelock, P. Fourie, J. Stoffels,

G. P. Evans, and T. Hasegawa. The IRSF Magellanic Clouds Point Source Catalog. *Publications of the Astronomical Society of Japan*, 59: 615–641, June 2007. doi: 10.1093/pasj/59.3.615.

D. Kato, Y. Ita, T. Onaka, T. Tanabé, T. Shimonishi, I. Sakon, H. Kaneda, A. Kawamura, T. Wada, F. Usui, B.-C. Koo, M. Matsuura, and H. Takahashi. AKARI Infrared Camera Survey of the Large Magellanic Cloud. I. Point-source Catalog. *The Astronomical Journal*, 144(6):179, Dec. 2012. doi: 10.1088/0004-6256/144/6/179.

R. Kippenhahn, A. Weigert, and A. Weiss. *Stellar Structure and Evolution*. 2012. doi: 10.1007/978-3-642-30304-3.

U. Kolb and H. Ritter. A comparative study of the evolution of a close binary using a standard and an improved technique for computing mass transfer. *Astronomy & Astrophysics*, 236:385–392, Sept. 1990.

J. Krtička and J. Kubát. Improved velocity law parameterization for hot star winds. *Astronomy & Astrophysics*, 534:A97, Oct. 2011. doi: 10.1051/0004-6361/201116679.

G. P. Kuiper. On the Interpretation of β Lyrae and Other Close Binaries. *Astrophysical Journal*, 93:133, Jan. 1941. doi: 10.1086/144252.

T. Lanz and I. Hubeny. A Grid of Non-LTE Line-blanketed Model Atmospheres of O-Type Stars. *The Astrophysical Journal Supplement Series*, 146(2):417–441, June 2003. doi: 10.1086/374373.

B. M. Lasker, M. G. Lattanzi, B. J. McLean, B. Bucciarelli, R. Drimmel, J. Garcia, G. Greene, F. Guglielmetti, C. Hanley, G. Hawkins, V. G. Laidler, C. Loomis, M. Meakes, R. Mignani, R. Morbidelli, J. Morrison, R. Pannunzio, A. Rosenberg, M. Sarasso, R. L. Smart, A. Spagna, C. R. Sturch, A. Volpicelli, R. L. White, D. Wolfe, and A. Zacchei. The Second-Generation Guide Star Catalog: Description and Properties. *The Astronomical Journal*, 136(2):735–766, Aug. 2008. doi: 10.1088/0004-6256/136/2/735.

A. Loeb and R. Barkana. The Reionization of the Universe by the First Stars and Quasars. *Annual Review of Astronomy and Astrophysics*, 39: 19–66, Jan. 2001. doi: 10.1146/annurev.astro.39.1.19.

A. Maeder. Evidences for a bifurcation in massive star evolution. The ON-blue stragglers. *Astronomy & Astrophysics*, 178:159–169, May 1987.

L. Mahy, H. Sana, M. Abdul-Masih, L. A. Almeida, N. Langer, T. Shenar, A. de Koter, S. E. de Mink, S. de Wit, N. J. Grin, C. J. Evans, A. F. J. Moffat, F. R. N. Schneider, R. Barbá, J. S. Clark, P. Crowther, G. Gräfener, D. J. Lennon, F. Tramper, and J. S. Vink. The Taran-

tula Massive Binary Monitoring. III. Atmosphere analysis of double-lined spectroscopic systems. *Astronomy & Astrophysics*, 634:A118, Feb. 2020. doi: 10.1051/0004-6361/201936151.

P. Marchant, N. Langer, P. Podsiadlowski, T. M. Tauris, and T. J. Moriya. A new route towards merging massive black holes. *Astronomy & Astrophysics*, 588:A50, Apr. 2016. doi: 10.1051/0004-6361/201628133.

P. Marchant, N. Langer, P. Podsiadlowski, T. M. Tauris, S. de Mink, I. Mandel, and T. J. Moriya. Ultra-luminous X-ray sources and neutron-star-black-hole mergers from very massive close binaries at low metallicity. *Astronomy & Astrophysics*, 604:A55, Aug. 2017. doi: 10.1051/0004-6361/201630188.

F. Martins, D. Schaerer, and D. J. Hillier. A new calibration of stellar parameters of Galactic O stars. *Astronomy & Astrophysics*, 436(3):1049–1065, June 2005. doi: 10.1051/0004-6361:20042386.

F. Martins, A. Hervé, J. C. Bouret, W. Marcolino, G. A. Wade, C. Neiner, E. Alecian, J. Grunhut, and V. Petit. The MiMeS survey of magnetism in massive stars: CNO surface abundances of Galactic O stars. *Astronomy & Astrophysics*, 575:A34, Mar. 2015. doi: 10.1051/0004-6361/201425173.

M. Meixner, K. D. Gordon, R. Indebetouw, J. L. Hora, B. Whitney, R. Blum, W. Reach, J.-P. Bernard, M. Meade, B. Babler, C. W. Engelbracht, B.-Q. For, K. Misselt, U. Vijh, C. Leitherer, M. Cohen, E. B. Churchwell, F. Boulanger, J. A. Frogel, Y. Fukui, J. Gallagher, V. Gorjian, J. Harris, D. Kelly, A. Kawamura, S. Kim, W. B. Latter, S. Madden, C. Markwick-Kemper, A. Mizuno, N. Mizuno, J. Mould, A. Nota, M. S. Oey, K. Olsen, T. Onishi, R. Paladini, N. Panagia, P. Perez-Gonzalez, H. Shibai, S. Sato, L. Smith, L. Staveley-Smith, A. G. G. M. Tielens, T. Ueta, S. van Dyk, K. Volk, M. Werner, and D. Zaritsky. Spitzer Survey of the Large Magellanic Cloud: Surveying the Agents of a Galaxy's Evolution (SAGE). I. Overview and Initial Results. *The Astronomical Journal*, 132(6):2268–2288, Dec. 2006. doi: 10.1086/508185.

M. R. Mokiem, A. de Koter, J. S. Vink, J. Puls, C. J. Evans, S. J. Smartt, P. A. Crowther, A. Herrero, N. Langer, D. J. Lennon, F. Najarro, and M. R. Villamariz. The empirical metallicity dependence of the mass-loss rate of O- and early B-type stars. *Astronomy & Astrophysics*, 473(2):603–614, Oct. 2007. doi: 10.1051/0004-6361:20077545.

K. F. Neugent, P. Massey, and N. Morrell. A Modern Search for Wolf-Rayet Stars in the Magellanic Clouds. IV. A Final Census. *Astrophysical Journal*, 863(2):181, Aug. 2018. doi: 10.3847/1538-4357/aad17d.

A. Niedzielski and W. Skorzynski. Kinematical Structure of Wolf-Rayet

Winds. I.Terminal Wind Velocity. *Acta Astronomica*, 52:81–104, Mar. 2002.

T. Nugis and H. J. G. L. M. Lamers. Mass-loss rates of Wolf-Rayet stars as a function of stellar parameters. *Astronomy & Astrophysics*, 360: 227–244, Aug. 2000.

T. Nugis and H. J. G. L. M. Lamers. The mass-loss rates of Wolf-Rayet stars explained by optically thick radiation driven wind models. *Astronomy & Astrophysics*, 389:162–179, July 2002. doi: 10.1051/0004-6361:20020557.

L. M. Oskinova, W. R. Hamann, and A. Feldmeier. Neglecting the porosity of hot-star winds can lead to underestimating mass-loss rates. *Astronomy & Astrophysics*, 476(3):1331–1340, Dec. 2007. doi: 10.1051/0004-6361: 20066377.

S. P. Owocki, K. G. Gayley, and N. J. Shaviv. A Porosity-Length Formalism for Photon-Tiring-limited Mass Loss from Stars above the Eddington Limit. *Astrophysical Journal*, 616(1):525–541, Nov. 2004. doi: 10.1086/ 424910.

B. Paczyński. Evolution of Close Binaries. V. The Evolution of Massive Binaries and the Formation of the Wolf-Rayet Stars. *Acta Astronomica*, 17:355, Jan. 1967.

M. J. Page, C. Brindle, A. Talavera, M. Still, S. R. Rosen, V. N. Yershov, H. Ziaeepour, K. O. Mason, M. S. Cropper, A. A. Breeveld, N. Loiseau, R. Mignani, A. Smith, and P. Murdin. The XMM-Newton serendipitous ultraviolet source survey catalogue. *Monthly Notices of the Royal Astronomical Society*, 426(2):903–926, Oct. 2012. doi: 10.1111/j.1365-2966. 2012.21706.x.

B. Paxton, L. Bildsten, A. Dotter, F. Herwig, P. Lesaffre, and F. Timmes. Modules for Experiments in Stellar Astrophysics (MESA). *The Astrophysical Journal Supplement Series*, 192(1):3, Jan. 2011. doi: 10.1088/ 0067-0049/192/1/3.

B. Paxton, M. Cantiello, P. Arras, L. Bildsten, E. F. Brown, A. Dotter, C. Mankovich, M. H. Montgomery, D. Stello, F. X. Timmes, and R. Townsend. Modules for Experiments in Stellar Astrophysics (MESA): Planets, Oscillations, Rotation, and Massive Stars. *The Astrophysical Journal Supplement Series*, 208(1):4, Sept. 2013. doi: 10.1088/ 0067-0049/208/1/4.

B. Paxton, P. Marchant, J. Schwab, E. B. Bauer, L. Bildsten, M. Cantiello, L. Dessart, R. Farmer, H. Hu, N. Langer, R. H. D. Townsend, D. M. Townsley, and F. X. Timmes. Modules for Experiments in Stellar

Astrophysics (MESA): Binaries, Pulsations, and Explosions. *The Astrophysical Journal Supplement Series*, 220(1):15, Sept. 2015. doi: 10.1088/0067-0049/220/1/15.

G. Pietrzyński, D. Graczyk, W. Gieren, I. B. Thompson, B. Pilecki, A. Udalski, I. Soszyński, S. Kozłowski, P. Konorski, K. Suchomska, G. Bono, P. G. P. Moroni, S. Villanova, N. Nardetto, F. Bresolin, R. P. Kudritzki, J. Storm, A. Gallenne, R. Smolec, D. Minniti, M. Kubiak, M. K. Szymański, R. Poleski, Ł. Wyrzykowski, K. Ulaczyk, P. Pietrukowicz, M. Górski, and P. Karczmarek. An eclipsing-binary distance to the Large Magellanic Cloud accurate to two per cent. *Nature*, 495(7439): 76–79, Mar. 2013. doi: 10.1038/nature11878.

O. Pols. Binary Stars. Lecture notes for a Utrecht University MSc course. https://www.astro.ru.nl/ onnop/education/binaries$_u trecht_n otes$/.

A. Prsa and P. Harmanec. PHOEBE manual. *Villanova University, dept. of Astronomy and Astrophysics*, Apr. 2010.

A. Prša and T. Zwitter. A Computational Guide to Physics of Eclipsing Binaries. I. Demonstrations and Perspectives. *Astrophysical Journal*, 628 (1):426–438, July 2005. doi: 10.1086/430591.

N. Przybilla, M. Firnstein, M.-F. a. Nieva, G. Meynet, and A. Maeder. Mixing of CNO-cycled matter in massive stars. *Bulletin de la Societe Royale des Sciences de Liege*, 80:279–284, Jan. 2011.

J. Puls, M. A. Urbaneja, R. Venero, T. Repolust, U. Springmann, A. Jokuthy, and M. R. Mokiem. Atmospheric NLTE-models for the spectroscopic analysis of blue stars with winds. II. Line-blanketed models. *Astronomy & Astrophysics*, 435(2):669–698, May 2005. doi: 10.1051/0004-6361:20042365.

J. Puls, N. Markova, S. Scuderi, C. Stanghellini, O. G. Taranova, A. W. Burnley, and I. D. Howarth. Bright OB stars in the Galaxy. III. Constraints on the radial stratification of the clumping factor in hot star winds from a combined H_α, IR and radio analysis. *Astronomy & Astrophysics*, 454(2): 625–651, Aug. 2006. doi: 10.1051/0004-6361:20065073.

L. Rezzolla, E. R. Most, and L. R. Weih. Using Gravitational-wave Observations and Quasi-universal Relations to Constrain the Maximum Mass of Neutron Stars. *The Astrophysical Journal Letters*, 852(2):L25, Jan. 2018. doi: 10.3847/2041-8213/aaa401.

E. E. Salpeter. The Luminosity Function and Stellar Evolution. *Astrophysical Journal*, 121:161, Jan. 1955. doi: 10.1086/145971.

H. Sana. Binary stars. Lecture notes for a KULeuven MSc course, 2019.

H. Sana, S. E. de Mink, A. de Koter, N. Langer, C. J. Evans, M. Gieles, E. Gosset, R. G. Izzard, J. B. Le Bouquin, and F. R. N. Schneider. Binary Interaction Dominates the Evolution of Massive Stars. *Science*, 337(6093): 444, July 2012. doi: 10.1126/science.1223344.

H. Sana, A. de Koter, S. E. de Mink, P. R. Dunstall, C. J. Evans, V. Hénault-Brunet, J. Maíz Apellániz, O. H. Ramírez-Agudelo, W. D. Taylor, N. R. Walborn, J. S. Clark, P. A. Crowther, A. Herrero, M. Gieles, N. Langer, D. J. Lennon, and J. S. Vink. The VLT-FLAMES Tarantula Survey. VIII. Multiplicity properties of the O-type star population. *Astronomy & Astrophysics*, 550:A107, Feb. 2013. doi: 10.1051/0004-6361/201219621.

H. Sana, J. B. Le Bouquin, S. Lacour, J. P. Berger, G. Duvert, L. Gauchet, B. Norris, J. Olofsson, D. Pickel, G. Zins, O. Absil, A. de Koter, K. Kratter, O. Schnurr, and H. Zinnecker. Southern Massive Stars at High Angular Resolution: Observational Campaign and Companion Detection. *The Astrophysical Journal Supplement Series*, 215(1):15, Nov. 2014. doi: 10.1088/0067-0049/215/1/15.

A. A. C. Sander, W. R. Hamann, H. Todt, R. Hainich, T. Shenar, V. Ramachandran, and L. M. Oskinova. The Galactic WC and WO stars. The impact of revised distances from Gaia DR2 and their role as massive black hole progenitors. *Astronomy & Astrophysics*, 621:A92, Jan. 2019. doi: 10.1051/0004-6361/201833712.

D. J. Schlegel, D. P. Finkbeiner, and M. Davis. Maps of Dust Infrared Emission for Use in Estimation of Reddening and Cosmic Microwave Background Radiation Foregrounds. *Astrophysical Journal*, 500(2):525–553, June 1998. doi: 10.1086/305772.

F. R. N. Schneider, N. Langer, A. de Koter, I. Brott, R. G. Izzard, and H. H. B. Lau. Bonnsai: a Bayesian tool for comparing stars with stellar evolution models. *Astronomy & Astrophysics*, 570:A66, Oct. 2014. doi: 10.1051/0004-6361/201424286.

O. Schnurr, A. F. J. Moffat, N. St-Louis, N. I. Morrell, and M. A. Guerrero. A spectroscopic survey of WNL stars in the Large Magellanic Cloud: general properties and binary status. *Monthly Notices of the Royal Astronomical Society*, 389(2):806–828, Sept. 2008. doi: 10.1111/j.1365-2966.2008.13584.x.

T. Shenar, D. P. Sablowski, R. Hainich, H. Todt, A. F. J. Moffat, L. M. Oskinova, V. Ramachandran, H. Sana, A. A. C. Sander, O. Schnurr, N. St-Louis, D. Vanbeveren, Y. Götberg, and W. R. Hamann. The Wolf-Rayet binaries of the nitrogen sequence in the Large Magellanic Cloud. Spectroscopy, or-

bital analysis, formation, and evolution. *Astronomy & Astrophysics*, 627: A151, July 2019. doi: 10.1051/0004-6361/201935684.

T. Shenar, A. Gilkis, J. S. Vink, H. Sana, and A. A. C. Sand er. Why binary interaction does not necessarily dominate the formation of Wolf-Rayet stars at low metallicity. *Astronomy & Astrophysics*, 634:A79, Feb. 2020. doi: 10.1051/0004-6361/201936948.

S. Simón-Díaz and A. Herrero. The IACOB project. I. Rotational velocities in northern Galactic O- and early B-type stars revisited. The impact of other sources of line-broadening. *Astronomy & Astrophysics*, 562:A135, Feb. 2014. doi: 10.1051/0004-6361/201322758.

L. F. Smith. Absolute magnitudes and intrinsic colours of Wolf-Rayet stars. *Monthly Notices of the Royal Astronomical Society*, 140:409, Jan. 1968. doi: 10.1093/mnras/140.4.409.

G. E. Soberman, E. S. Phinney, and E. P. J. van den Heuvel. Stability criteria for mass transfer in binary stellar evolution. *Astronomy & Astrophysics*, 327:620–635, Nov. 1997.

J. O. Sundqvist and S. P. Owocki. Clumping in the inner winds of hot, massive stars from hydrodynamical line-driven instability simulations. *Monthly Notices of the Royal Astronomical Society*, 428(2):1837–1844, Jan. 2013. doi: 10.1093/mnras/sts165.

R. E. Taam and E. L. Sandquist. Common Envelope Evolution of Massive Binary Stars. *Annual Review of Astronomy and Astrophysics*, 38:113–141, Jan. 2000. doi: 10.1146/annurev.astro.38.1.113.

T. M. Tauris and E. P. J. van den Heuvel. *Formation and evolution of compact stellar X-ray sources*, volume 39, pages 623–665. 2006.

A. Udalski, M. Szymanski, J. Kaluzny, M. Kubiak, and M. Mateo. The Optical Gravitational Lensing Experiment. *Acta Astronomica*, 42:253–284, Oct. 1992.

K. A. van der Hucht. Past and present classification of hot massive stars. In J. M. Vreux, A. Detal, D. Fraipont-Caro, E. Gosset, and G. Rauw, editors, *Liege International Astrophysical Colloquia*, volume 33 of *Liege International Astrophysical Colloquia*, page 1, Jan. 1996.

K. A. van der Hucht. The VIIth catalogue of galactic Wolf-Rayet stars. *New Astronomy Reviews*, 45(3):135–232, Feb. 2001. doi: 10.1016/S1387-6473(00)00112-3.

H. van Winckel. Radiative Processes in Astronomy. Lecture notes for a KULeuven MSc course, 2016.

J. S. Vink, A. de Koter, and H. J. G. L. M. Lamers. New theoretical mass-loss rates of O and B stars. *Astronomy & Astrophysics*, 362:295–309, Oct. 2000.

B. E. Westerlund and L. F. Smith. Worlf-Rayet Stars in the Large Magellanic Cloud. *Monthly Notices of the Royal Astronomical Society*, 128:311, Jan. 1964. doi: 10.1093/mnras/128.4.311.

H. E. White, T. W. Baumgarte, and S. L. Shapiro. Gravity Darkening and Brightening in Binaries. *Astrophysical Journal*, 752(2):122, June 2012. doi: 10.1088/0004-637X/752/2/122.

S. C. Yoon and N. Langer. Evolution of rapidly rotating metal-poor massive stars towards gamma-ray bursts. *Astronomy & Astrophysics*, 443(2):643–648, Nov. 2005. doi: 10.1051/0004-6361:20054030.

N. Zacharias, C. T. Finch, T. M. Girard, A. Henden, J. L. Bartlett, D. G. Monet, and M. I. Zacharias. The Fourth US Naval Observatory CCD Astrograph Catalog (UCAC4). *The Astronomical Journal*, 145(2):44, Feb. 2013. doi: 10.1088/0004-6256/145/2/44.

J. P. Zahn. The dynamical tide in close binaries. *Astronomy & Astrophysics*, 41:329–344, July 1975.

S. Zucker. Cross-correlation and maximum-likelihood analysis: a new approach to combining cross-correlation functions. *Monthly Notices of the Royal Astronomical Society*, 342(4):1291–1298, July 2003. doi: 10.1046/j.1365-8711.2003.06633.x.

S. Zucker and T. Mazeh. Study of Spectroscopic Binaries with TODCOR. I. A New Two-dimensional Correlation Algorithm to Derive the Radial Velocities of the Two Components. *Astrophysical Journal*, 420:806, Jan. 1994. doi: 10.1086/173605.

Appendices

A Accounting for interstellar reddening

This Appendix shows how the interstellar reddening (see Section 3.5) is accounted for in this thesis.

In order to correct for the reddening of the star, the following formula can be used

$$F_{\text{int}}(\lambda) = F_{\text{obs}}(\lambda) \times 10^{A(\lambda)/2.5}, \tag{A.1}$$

where $F_{\text{int}}(\lambda)$ and $F_{\text{obs}}(\lambda)$ are the intrinsic and the observed, or reddened, flux respectively, and $A(\lambda) = m_{\text{observed}}(\lambda) - m_{\text{intrinsic}}(\lambda)$ is the absolute extinction for a certain wavelength. Using the Johnson-UBV photometric system, the relative extinction parameter or coefficient for a given wavelength is defined as

$$R(\lambda) = \frac{A(\lambda)}{E(B-V)}, \tag{A.2}$$

where $A(\lambda)$ is the absolute extinction at the given wavelength and $E(B-V) = A(B) - A(V)$ is the reddening. Substituting Eq. (A.2) into (A.1) gives the following final formula to obtain the intrinsic or dereddened flux

$$F_{\text{int}}(\lambda) = F_{\text{obs}}(\lambda) \times 10^{R(\lambda)E(B-V)/2.5}. \tag{A.3}$$

In this report, reddening models is preferred to dereddening data. The formula is the following

$$F_{\text{obs}}(\lambda) = F_{\text{int}}(\lambda) \times 10^{R(\lambda)E(B-V)/-2.5}. \tag{A.4}$$

$R(\lambda)$ is determined by the fit of the reddening law as presented by Howarth (1983). However, rather than working with the parameter λ, he works with the parameter $x = 1/\lambda$, with λ in μm and the relative extinction parameter $X(x) = A(\lambda)/E(B-V)$.

The relative extinction coefficient for the UV, in the LMC, is defined as

$$X_{\rm UV,LMC}(x) = R_{\rm LMC}(V) - 0.236 + 0.462x + 0.105x^2 + 0.454/[(x-4.557)^2 + 0.293], \tag{A.5}$$

for the optical in the LMC as

$$X_{\rm opt,LMC}(x) = R_{\rm LMC}(V) + 2.04(x-1.83) + 0.094(x-1.83)^2, \tag{A.6}$$

and for the optical in the Galaxy as

$$X_{\rm opt,gal}(x) = R_{\rm gal}(V) + 2.56(x-1.83) - 0.993(x-1.83)^2, \tag{A.7}$$

where for the UV $2.75 \leq x \leq 9.0$ and for the optical $1.83 \leq x \leq 2.75$ and $R(V)$ defined by Eq. (A.2).

The extinction in the IR is determined by

$$X_{\rm IR}(x) = [(1.86 - 0.48x)x - 0.1]x \tag{A.8}$$

and is the same for the Galaxy and the LMC.

The equations for the reddened model in the UV, optical and IR are then respectively:

$$F_{\rm UV}(\lambda) = F_{\rm int}(\lambda) \times 10^{X_{\rm UV,LMC}(x)(E_{\rm LMC}(B-V)+0.03)/-2.5}, \tag{A.9}$$

$$F_{\rm opt}(\lambda) = F_{\rm int}(\lambda) \times 10^{X_{\rm opt,LMC}(x)E_{\rm LMC}(B-V)/-2.5} \times 10^{0.03X_{\rm opt,gal}(x)/-2.5}, \tag{A.10}$$

$$F_{\rm IR}(\lambda) = F_{\rm int}(\lambda) \times 10^{X_{\rm IR}(x)(E_{\rm LMC}(B-V)+0.03)/-2.5}, \tag{A.11}$$

where the values for the Galaxy have been replaced with $R_{\rm gal}(V) = 3.1$ (Fitzpatrick, 1999) and $E_{\rm gal}(B-V) = 0.03$ (Schlegel et al., 1998). $F_{\rm int}(\lambda)$ is the model flux coming from the SED in the ranges specified above.

B Deriving ν in the radial-velocity curve

The radial-velocity curve was given in (4.2) and is repeated here:

$$v_{\mathrm{rad}} = \gamma + K\left[e\cos\omega + \cos(\omega+\nu)\right]. \tag{B.1}$$

The only variable in the radial-velocity curve is the true anomaly ν. In order to find ν we use the auxiliary circle of the ellipse describing the orbit. This is the circle centred around the centre of the ellipse with a radius equal to the semi-major axis. A schematic representation is given in Figure B.1. Two new variables are introduced: the mean anomaly M and the eccentric anomaly E. The mean anomaly is defined as

$$M = \frac{2\pi}{P}(t - T0), \tag{B.2}$$

where t is the time at a particular phase in the orbit. The eccentric anomaly E can be determined by Kepler's equation, which takes the form

$$M = E - e\sin E. \tag{B.3}$$

In order to solve this equation, a numerical method, such as the Newton-Raphson method, must be used. Once E is determined, ν can be obtained with the following equation:

$$\tan\left(\frac{\nu}{2}\right) = \sqrt{\frac{1+e}{1-e}}\tan\left(\frac{E}{2}\right). \tag{B.4}$$

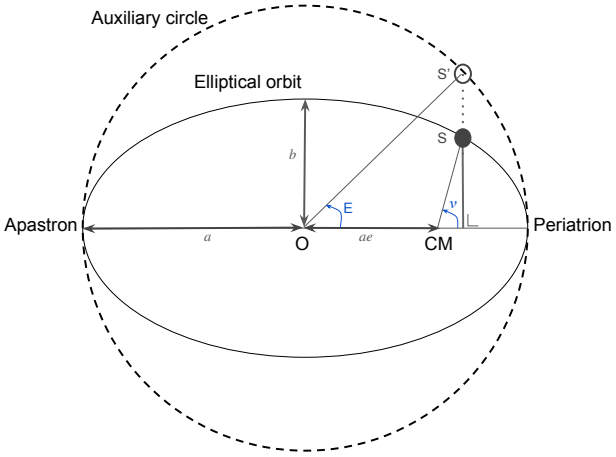

Figure B.1: Schematic representation of an elliptic orbit with its auxiliary circle. The auxiliary circle has a radius equal to the semi-major axis of the ellipse and has the same centre. The centre of the ellipse is marked with O and the centre of mass of the orbit is marked as CM. The true anomaly ν, eccentric anomaly E, the semi-major axis a, semi-minor axis b and the distance from the centre to the focal point ae are indicated on the diagram. The point S is the position of the star on the orbit and point S' is the projection of the star on the auxiliary circle.

C Photometric observations

This Appendix shows a table with the wavelengths, fluxes and photometric filters of photometric observations taken for BAT99 126. The table is referenced in Section 6.2.

Table C.1: Photometric observations of BAT99 126. Data obtained from VizieR (`http://vizier.unistra.fr/vizier/sed/`).

Passband	Effective wavelength [Å]	Flux [erg $s^{-1}cm^{-2}Å^{-1}$]	Magnitude	Ref.
XMM-OT:UVW2	2 118.97	1.99e-13 ± 6.68e-16	10.66	a
XMM-OT:UVM2	2 311.07	1.48e-13 ± 5.61e-16	10.99	a
XMM-OT:UVW1	2 908.07	1.02e-13 ± 1.44e-17	11.39	a
XMM-OT:U	3 441.18	5.90e-14 ± 8.71e-17	11.99	a
Johnson:U	3 971.0	5.61e-14 ± 2.80e-15	12.04	b
Johnson:B	4 481.0	4.08e-14 ± 2.04e-15	12.39	b
XMM-OT:B	4 505.79	2.86e-14 ± 1.36e-17	12.77	a
Johnson:V	5 423.0	2.06e-14 ± 1.03e-15	13.13	b
XMM-OT:V	5 430.53	1.92e-14 ± 1.02e-16	13.20	a
POSS-II:F	6 399.94	1.35e-14 ± 5.64e-15	13.59	c
Johnson:R	6 441.0	8.97e-15 ± 4.49e-16	14.03	b
POSS-II:i	7 836.89	8.69e-15 ± 3.47e-15	14.07	c
Johnson:I	8 071.0	5.85e-15 ± 2.92e-16	14.50	b
VISTA:Y	10 183.86	2.38e-15 ± 2.89e-18	15.48	d
2MASS:J	12 390.17	1.74e-15 ± 3.12e-17	15.81	f
VISTA:J	12 463.83	1.81e-15 ± 1.93e-18	15.77	d
Johnson:J	12 500.21	1.75e-15 ± 3.45e-17	15.81	e
Johnson:H	16 300.16	6.79e-16 ± 1.58e-17	16.83	e
2MASS:H	16 494.77	6.70e-16 ± 1.65e-17	16.85	f
VISTA:Ks	21 337.54	2.16e-16 ± 6.58e-19	18.08	d
2MASS:Ks	21 637.85	2.88e-16 ± 7.68e-18	17.77	f
Johnson:K	21 900.25	2.72e-16 ± 8.75e-18	17.83	e
AKARI:N3	31 899.94	1.06e-16 ± 3.54e-18	18.85	g
WISE:W1	33 500.10	7.83e-17 ± 1.87e-18	19.18	h
Spitzer/IRAC:3.6	35 499.82	6.07e-17 ± 2.38e-18	19.46	i
Spitzer/IRAC:4.5	44 930.23	3.49e-17 ± 8.91e-19	20.06	i
WISE:W2	46 000.19	2.88e-17 ± 7.08e-19	20.27	h
Spitzer/IRAC:5.8	57 309.64	1.51e-17 ± 5.48e-19	20.97	i
AKARI:S7	71 199.46	7.63e-18 ± 3.55e-19	21.71	g
Spitzer/IRAC:8.0	78 720.81	6.34e-18 ± 2.90e-19	21.91	i
AKARI:S11	104 501.00	2.96e-18 ± 1.92e-19	22.73	g
WISE:W3	115 598.23	4.85e-19 ± 1.48e-19	24.70	h
WISE:W4	220 906.68	1.12e-18 ± 3.81e-19	23.79	h

Data taken from a) Page et al. (2012); b) Bonanos et al. (2009); c) Lasker et al. (2008); d) Cioni et al. (2011); e) Kato et al. (2007); f) Zacharias et al. (2013); g) Kato et al. (2012); h) Cutri and et al. (2012); i) Meixner et al. (2006)

D Extra material on the derived RVs

This Appendix is related to extra results of the radial velocities (RVs) obtained with the cross-correlation and line-profile fitting method (Section 7.4). It shows

- An example of a smooth CCF for the WR star on the N V λ4603.73 line, using a single spectrum as the template.
- An image of the RVs of the WR star showing the discrepancy between the measurements for the N V λ4944.56 line and the measurements of the other spectral lines.
- An example of a badly behaving CCF for the WR star for the N V λ4944.56 line
- How using a different spectrum as the template for the WR star will not alter the derived RVs significantly
- An example of the CCF for the O II λ4347.42/4351.26 and O II λ4349.43 lines

A smooth CCF for the WR star on the N V λ4603.73 line

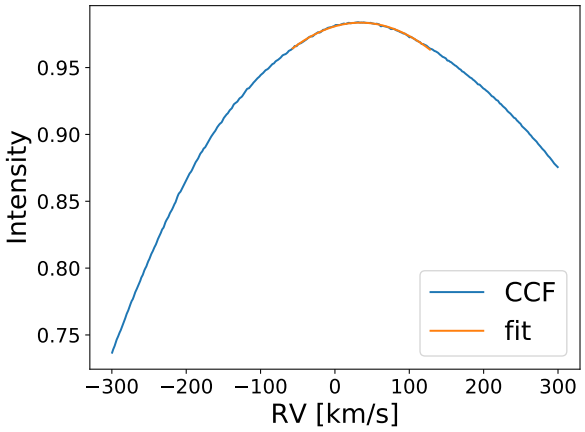

Figure D.1: Example of the CCF obtained by cross-correlating one of the spectra with the N V λ4603.73 line. The example shows the results for the spectrum taken at MJD

RVs of the WR star showing the discrepancy between the measurements for the N V λ4944.56 line and the measurements of the other spectral lines

An example of the discrepancy between the N V λ4944.56 line and the other three lines is shown in Figure D.2. The RVs are obtained using a single spectrum as the mask, here the one taken at MJD 58444.10. The data points are not calibrated, but naturally they show values around zero at this MJD. This Figure thus also shows how a small uncertainty is induced by the polynomial fitting on the CCF, as the values at MJD 58444.10 are not exactly zero here.

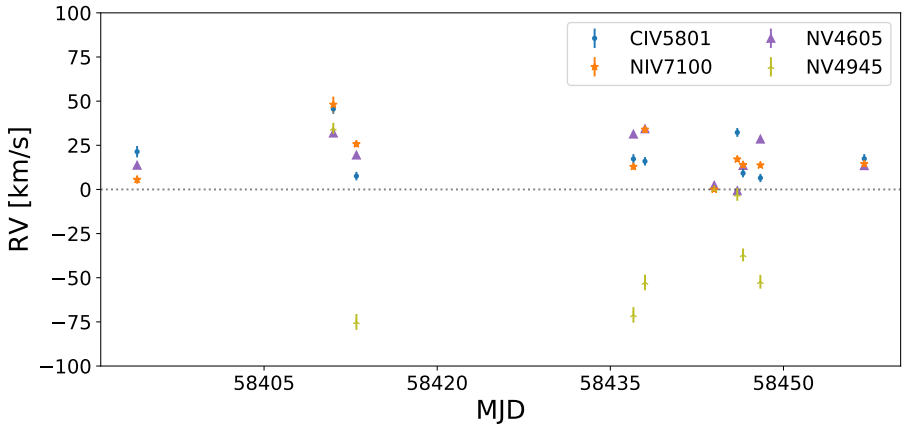

Figure D.2: Obtained RVs of the WR star using four different lines: C IV λ5801.33/5811.98 (CIV5801, blue dots), N IV $\sim$ λ7100 (NIV7100, orange stars), N V λ4603.73 (NV4605, purple triangles) and N V λ4944.56 (NV4945, yellow tri-crosses).

Bad CCF for the WR star

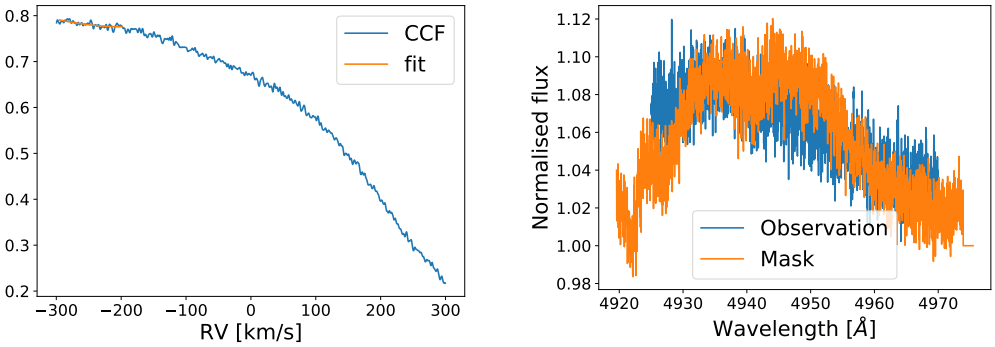

Figure D.3: Example of a bad behaving CCF. Left: The CCF in blue and the polynomial fit in orange. Right: The spectrum whose RV is derived (blue) and the mask (orange).

How using a different spectrum as the template will not alter the derived RVs of the WR star significantly

Figure D.4 shows the RVs for the N V λ4603.73 line obtained with two different templates. The blue triangles are the RVs obtained with the spectrum corresponding to MJD 58437.31. For the RVs shown by the yellow dots the spectrum corresponding to MJD 58444.10 is used as the template. For visual purposes, the RVs have been calibrated to be zero at MJD 58444.10. It can be seen that the derived RVs are not completely equivalent with each other.

In Figure D.5 two sets of RVs can be seen. These correspond to the RVs derived with different coadded templates. The coadded spectra have been created by using the RVs of the N V λ4603.73 line with the two different spectra mentioned above as the original template. In the legend they are indicated with MJD58437 and MJD58444 to indicate the original spectrum that was used as the template. Instead of showing all lines, only C IV λ5801.33/5811.98 (legend name: CIV5801) and N IV $\sim \lambda$7100 (legend name: NIV7100) are shown. None of the RVs are calibrated. It can be seen that there is a slight difference in derived RVs. However, it is seen that the variation between the measurements has the same trend for every set of data points. Hence, the results presented in Section 7.4.3 will not be altered significantly. When symbols of a certain line are not shown, it is because their uncertainty could not be derived because of a badly behaving CCF.

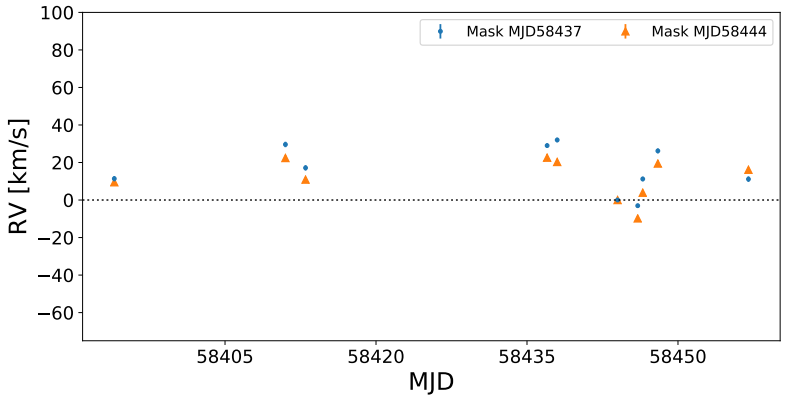

Figure D.4: RVs for the N v λ4603.73 line obtained with two different templates. Blue dots are the RVs obtained with the spectrum corresponding to MJD 58437.31. Orange triangles are the RVs obtained with the spectrum corresponding to MJD 58444.10. RVs are calibrated such that both have RV = 0 km/s at MJD 58444.10.

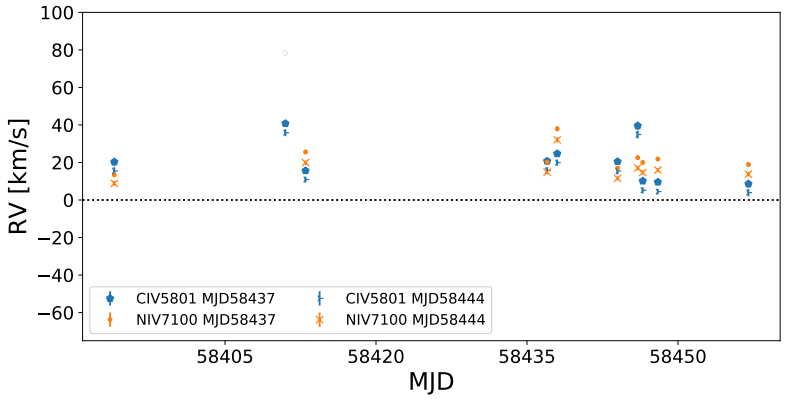

Figure D.5: RVs of the WR star for the C IV λ5801.33/5811.98, N v λ4944.56 and N IV $\sim \lambda$7100 line obtained with two different templates. The template in both cases is a coadded spectrum created from the derived RVs of the N v λ4603.73 line. One is created by using as an original template the spectrum at MJD 58437.31, the second one uses the spectrum at MJD 58444.10. The blue symbols correspond to the C IV λ5801.33/5811.98 line and orange symbols correspond to the N IV $\sim \lambda$7100 line.

Example of the CCF for the O II λ4347.42/4351.26 and O II λ4349.43 lines

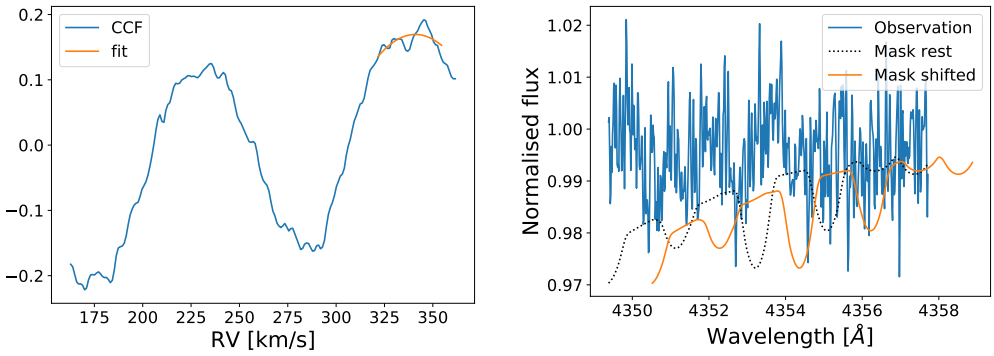

Figure D.6: Example of a bad CCF (left) and renormalised spectrum (right) with fits (orange) of the O II λ4347.42/4351.26 and O II λ4349.43 lines. In the right-hand panel, the model at the rest wavelength with a velocity of the LMC ($v = 262.2$ km/s) is shown with a dotted black line. The orange model shows the model shifted with the derived RV.

INSTITUUT VOOR STERRENKUNDE
Celestijnenlaan 200D bus 2401
3000 LEUVEN, BELGIË
tel. + 32 16 37 46 28
www.kuleuven.be